ADVANCED INTERFACE SYSTEMS FOR READOUT, CONTROL, AND SELF-CALIBRATION OF MEMS RESONANT GYROSCOPES

A Dissertation
Presented to
The Academic Faculty

by

Arashk Norouzpour-Shirazi

In Partial Fulfillment
of the Requirements for the Degree
Doctor of Philosophy in the
School of Electrical and Computer Engineering

Georgia Institute of Technology
May 2016

ADVANCED INTERFACE SYSTEMS FOR READOUT, CONTROL, AND SELF-CALIBRATION OF MEMS RESONANT GYROSCOPES

Approved by:

Prof. Farrokh Ayazi, Advisor
School of Electrical and Computer
Engineering
Georgia Institute of Technology

Prof. John D. Cressler
School of Electrical and Computer
Engineering
Georgia Institute of Technology

Prof. Hua Wang
School of Electrical and Computer
Engineering
Georgia Institute of Technology

Prof. Oliver Brand
School of Electrical and Computer
Engineering
Georgia Institute of Technology

Prof. Hamid Garmestani
School of Materials Science and
Engineering
Georgia Institute of Technology

Date Approved: December 2, 2015

I dedicate this dissertation to my loving parents for
their support, encouragement, and wisdom

ACKNOWLEDGEMENTS

I would like to express my sincere gratitude to my advisor and mentor, Professor Farrokh Ayazi for his insightful guidance, support, and encouragement, for believing in my ability to succeed and for guiding me towards success.

I would also like to thank my dissertation defense committee members, Professor John Cressler, Professor Oliver Brand, Professor Hamid Garmestani, and Professor Hua Wang. It has been a great privilege to benefit from their input and help in construction of my dissertation. I am especially grateful to Professor John Cressler for the invaluable technical and life lessons that I learned from him throughout my study at Georgia Tech. It has been always a great pleasure to attend his teaching classes in Georgia Tech and study his books.

I would also like to express my sincere appreciation to Qualtré, for providing unlimited test devices for my research.

My research adventure would not have been as exciting and productive without every single help that I received from my precious colleagues who shared their intuition and experiences with me all these years. I would like to acknowledge my colleagues at IMEMS group in Georgia Institute of Technology, for their valuable support over the past 5 years. My special thanks go to Dr. Diego Serrano and Mr. Mojtaba Hodjat-Shamami for all the time and effort they spent on brainstorming and detailed technical discussions. I truly admire their never-ending passion for solving the unsolved, and finding the truth. I

TABLE OF CONTENTS

LIST OF TABLES

LIST OF FIGURES

SUMMARY

MEMS gyroscopes have become an essential component in many consumer, industrial and automotive applications, owing to their small form factor and low production cost. However, their poor stability, also known as drift, has hindered their penetration into high-end tactical and navigation applications, where highly stable bias and scale factor are required over long period of time to avoid significant positioning error. Improving the long-term stability of MEMS gyroscopes has created new challenges in both the physical sensor design and fabrication, as well as the system architecture used for interfacing with the physical sensor.

The objective of this research is to develop interface circuits and systems for control and self-calibration of MEMS resonators and Coriolis resonant gyroscopes to enhance the stability of bias and scale factor without the need for any mechanical rotary stage.

For resonator frequency calibration and tuning, an electrical scheme is presented which provides access to manipulating the mechanical parameters of MEMS resonators by generating displacement and acceleration signals from the velocity output of the resonator, thereby modifying the equivalent mass and stiffness of the resonator via electrical stimulus. This unique method of generating and applying the electrical equivalent of mechanical forces from the resonator output signal can be generalized to mimic any desired force in resonant structures, or to cancel any undesired force in such devices. The applicability of this active tuning method to enhance the stability performance of piezoelectric-on-Silicon MEMS resonators and gyroscopes is verified by simulations and measurements. For the first time, a 14MHz MEMS-based VCO with 1550 ppm linear bidirectional tuning is implemented using this technique.

Further, a self-calibrating dual-mode interface architecture is introduced that simultaneously actuates and senses both gyroscopic modes of an axisymmetric bulk

acoustic wave (BAW) gyroscope. The difference of the two mode outputs provides inherent bias compensation, while doubling the rate sensitivity. Moreover, the quadrature-phase component of the difference output provides rate-independent monitoring of the frequency mismatch of the gyroscope modes, and thus facilitates in-run compensation of the split. The sum of the two modes is used to close a self-sustaining drive actuation loop. The dual-mode scheme theoretically eliminates the mechanical bias terms of an axisymmetric gyroscope, limiting the drift performance to that of the second-order mismatch errors between the gyroscope modes. The in-run mode-matching capability provides up to 45 times temperature compensation of the MEMS gyroscope bias, achieving ±1.5 °/s peak-to-peak bias variation over a temperature range of [10 - 80] °C. The active tuning technique is utilized to virtually emulate mechanical rotation in the resonant Coriolis gyroscope, for the purpose of online scale factor calibration. The response of the gyroscope to the virtual rate is used for monitoring of physical scale factor drifts over time and temperature, and compensating for those drifts. The in-situ scale factor calibration system improves the temperature stability of scale factor by >250 times, to better than 0.15%, and also reduces the long-term drift of scale factor by 150 times to as low as 60 ppm, over 7 days.

The system architectures presented in this dissertation introduce paradigm shifts in interface system design methodologies for readout, control, and self-calibration of MEMS resonators and resonant sensors. The tuning and self-calibration schemes are presented with detailed mathematical analysis, with and without nonidealities. Each effect is validated by simulations using circuit-based resonator and gyroscope models in Cadence. Measurement results show the effectiveness of each of the proposed tuning and self-calibration techniques.

CHAPTER 1

INTRODUCTION

Gyroscopes are mechanical sensors that measure angular rotation about a certain axis. Mechanical gyroscopes have been used for decades in their traditional navigation role, as gyrocompass instruments in situations where magnetic compass units cannot operate, or are not accurate enough, such as stabilization of aircrafts or unmanned vehicles, intercontinental ballistic missiles, etc. Through multiple generations, gyroscope technologies have matured from bulky mechanical spinning gyroscopes that utilize the conservation of angular momentum to detect rate, to less bulky optical gyroscopes that use the Sagnac effect to detect rate, to Coriolis vibratory gyroscopes (CVG), which have eventually evolved to miniaturized micro-electromechanical (MEMS) Coriolis resonant gyroscopes that benefit from small form factor, low power consumption, ease of electrical interface, and low cost of production. The most recent technologies including nuclear magnetic resonance (NMR) gyroscope and quantum gyroscope offer superb stability and precision at the cost of relatively bulky and expensive implementations which disqualifies them for integrated high-end consumer applications such as personal navigation or GPS augmentation.

Micromachined gyroscopes offer small size at low production costs, which qualifies them for integrated navigation solutions [1]. However, these structures are relatively noisy compared to their more expensive counterparts. Moreover, due to their resonance-based principle of operation, these gyroscopes are affected by environmental variations, such as temperature variation and aging, which result in performance drifts. Fabrication imperfections can create undesired mismatches and coupling terms between the electromechanical parameters of the gyroscopic modes of micromachined devices, which can deteriorate the performance drift further.

The main goal of this dissertation is the research and development of self-calibration techniques for reduction of drift errors in MEMS resonant gyroscopes, by means of electrical foreground calibration schemes.

1.1   MEMS CORIOLIS RESONANT GYROSCOPES

Inertial measurement units (IMUs) have been successfully deployed in a variety of industrial and aerospace applications over the past few decades, to provide high-precision motion sensing and navigation [1]-[2]. With the advances in micromachining technology, the miniaturized inertial sensors were used for a wide array of low-accuracy and low-power consumer and automotive applications such as image stabilization for digital cameras, motion sensing for gaming consoles, anti-skid control and airbag deployment in automobiles, and platform stabilization.

Different applications require different performance levels for the inertial measurement system. Table I summarizes the performance grades for gyroscopes [3]. Rate grade, tactical grade and inertial grade performances are used in consumer applications, industrial and automotive applications, and navigation applications, respectively. While consumer applications require relatively relaxed noise, accuracy and stability performance, navigation applications typically have stringent requirements on noise, accuracy, and overall performance stability, to provide precision positioning.

Table I: Performance grades of gyroscopes [3].

	Rate Grade	Tactical Grade	Inertial (Navigation) Grade
Bias drift	10 to 1000 °/hr	0.01 to 10 °/hr	<0.01 °/hr
Angle random walk	> 0.5 °/√hr	0.5 - 0.05 °/√hr	< 0.001 °/√hr
Scale factor accuracy	0.1 - 1%	100 – 1000 ppm	< 10 ppm
Full scale range	50 - 1000 °/sec	>500 °/sec	>400 °/sec
Bandwidth	> 70 Hz	~100 Hz	~100 Hz

1.1.1 Principle of Operation

Vibratory gyroscopes operate based on the Coriolis effect which is the energy transfer between two orthogonal resonance modes of a device as a result of an out-of-plane rotation [4]. Figure 1.1 shows an example of a tuning-fork gyroscope operating based on Coriolis energy transfer. The primary resonance mode is actuated along the x-axis, and a rotation about the z-axis induces Coriolis acceleration along y-axis, moving the fork tines along y direction. Coriolis acceleration can be mathematically expressed as:

$$\vec{a}_{cor} = 2\vec{v} \times \vec{\Omega}_z \qquad (1.1)$$

where v is the velocity of the primary in-plane mode, also called the drive mode, and Ω_z is the rotation about the out-of-plane axis (z-axis). Based on (1), the Coriolis acceleration is generated at the same frequency as that of the drive mode, but along the secondary in-plane mode, also known as the sense mode. It can be understood intuitively that the Coriolis acceleration can generate larger displacement along the sense axis, if the resonance frequencies of the sense mode and drive mode are matched [5]-[6].
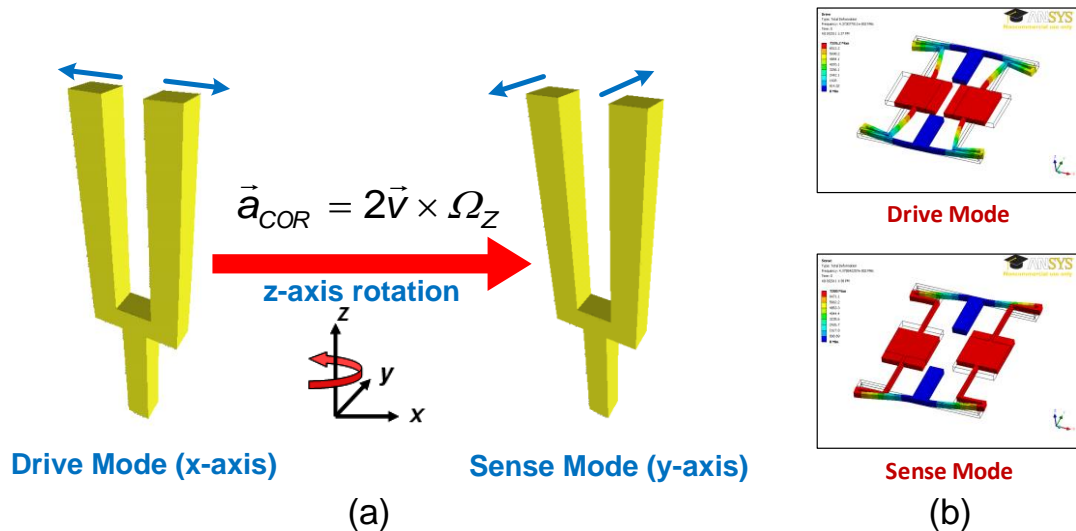
Figure 1.1: (a) Coriolis effect in a tuning fork, (b) Tuning-fork gyroscope (TFG) operating based on the Coriolis effect [5].

3

The mathematical representation of MEMS vibratory gyroscopes operation can be described as follows:

$$m\ddot{x} + d_{xx}\dot{x} + k_{xx}x + k_{yx}y + d_{yx}\dot{y} = f_x(t) - 2m\lambda\Omega_z\dot{y}$$
$$m\ddot{y} + d_{yy}\dot{y} + k_{yy}y + k_{xy}x + d_{xy}\dot{x} = f_y(t) + 2m\lambda\Omega_z\dot{x}$$

(1.2)

where m is the mass of the resonator, d_{ii} and k_{ii} terms are the damping and stiffness of the resonance modes along their respective axes, and $d_{xy} = d_{yx}$ and $k_{xy} = k_{yx}$ terms are the damping and stiffness coupling terms between the two modes [7]-[8]. This equation can be represented in the Laplace domain as follows:

$$\begin{bmatrix} s^2 + \dfrac{\omega_x}{Q_x}s + \omega_x^2 & \omega_{xy}^2 + \dfrac{\omega_{xy}}{Q_{xy}}s + 2\lambda\Omega_z s \\ \omega_{yx}^2 + \dfrac{\omega_{yx}}{Q_{yx}}s - 2\lambda\Omega_z s & s^2 + \dfrac{\omega_y}{Q_y}s + \omega_y^2 \end{bmatrix} \bullet \begin{bmatrix} X(s) \\ Y(s) \end{bmatrix} = \begin{bmatrix} F_x(s)/m \\ F_y(s)/m \end{bmatrix}$$

(1.3)

In the above set of equations:

$$\frac{d_{xx}}{m} = \frac{\omega_x}{Q_x}, \frac{d_{yy}}{m} = \frac{\omega_y}{Q_y}, \frac{k_{xx}}{m} = \omega_x^2, \frac{k_{yy}}{m} = \omega_y^2$$

$$\frac{d_{xy}}{m} = \frac{d_{yx}}{m} = \frac{\omega_{xy}}{Q_{xy}} = \frac{\omega_{yx}}{Q_{yx}}, \frac{k_{xy}}{m} = \frac{k_{yx}}{m} = \omega_{xy}^2 = \omega_{yx}^2$$

(1.4)

Theoretically each of the x and y modes can be excited into resonance via mechanical forces f_x and f_y, respectively. As explained earlier, the Coriolis coupling from a primary mode to a secondary mode is proportional to both the applied mechanical rotation rate about the sensitive axis (z-axis in this case), Ω_z, and the velocity of the primary mode vibration. The cross product of the two vectors is scaled by a scalar angular gain, λ, which is determined by the geometry of the device and its gyroscopic mode shapes. The opposite-phase Coriolis terms change the gyroscope equations, and thus its overall transfer function, when a rotation is applied.

4

1.1.2 Mode-Matching in MEMS Coriolis Gyroscopes

As mentioned earlier, the most common way of interfacing a Coriolis gyroscope is to excite the *x*-mode (drive mode) into oscillation, and then detect the Coriolis-induced deflection along the *y*-mode (sense mode) axis, which is an amplitude-modulated (AM) signal with its envelope proportional to the applied rate and at the frequency of the drive mode oscillations. In this case, and in the absence of mode coupling terms, (1.3) can be simplified to:

$$
\left(s^2 + \frac{\omega_x}{Q_x} s + \omega_x^2 \right) X(s) = \frac{F_x(s)}{m}, \quad f_x(t) = F_0 \cos \omega_x t
$$

$$
\left(s^2 + \frac{\omega_y}{Q_y} s + \omega_y^2 \right) Y(s) = -2s\lambda \Omega_z X(s). \tag{1.5}
$$

In the above representation, the drive mode is actuated by a sinusoidal excitation at ω_x, while the sense mode is excited by the Coriolis force. The drive-mode resonator can be used in a series-mode oscillator loop to provide self-sustaining actuation to the gyroscope, while the Coriolis-induced displacement of the sense mode can be detected and multiplied by the drive signal to demodulate rate.

Based on (1.5), and given that typically $\omega_x, \omega_y \gg \Delta\omega$, the drive and sense displacements are derived as:

$$
x(t) = \frac{Q_x F_x}{m\omega_x^2} \sin \omega_x t, \quad \dot{x}(t) = \frac{Q_x F_x}{m\omega_x} \cos \omega_x t
$$

$$
y(t) \approx \frac{2\lambda \Omega_z Q_x F_x \cos(\omega_x t + \varphi)}{m\omega_x^2 \times \sqrt{(2\Delta\omega)^2 + (\omega_y/Q_y)^2}}, \quad \varphi \approx \tan^{-1} \frac{\omega_y/Q_y}{2\Delta\omega} \tag{1.6}
$$

where $\Delta\omega$ is the angular frequency split between the two gyroscope modes, and ω_y/Q_y is the sense-mode 3-dB bandwidth (*BW*). The sense-mode displacement can also be

5

specifically derived at mode-matched condition (i.e. $\Delta\omega = 0$), and at mode-split condition ($\Delta\omega > BW$) as follows:

$$\Delta\omega = 0 \;\rightarrow\; y(t) \approx -\frac{2\lambda\Omega_z Q_x}{m\omega_x^3} Q_y F_x \sin(\omega_x t)$$

$$\Delta\omega \gg BW \;\rightarrow\; y(t) \approx \frac{\lambda\Omega_z Q_x}{m\omega_x^2} \frac{F_x \cos(\omega_x t)}{\Delta\omega} \tag{1.7}$$

As can be concluded from (1.7), at mode-matched condition, i.e. $\Delta\omega = 0$ (Figure 1.2a), sense-mode displacement is directly proportional to the sense-mode quality factor, Q_y, while at mode-split condition where $\Delta\omega \gg BW$ (Figure 1.2b), the sense-mode displacement becomes inversely proportional to $\Delta\omega$. Besides the maximum sensitivity and SNR at mode-matched condition, the Coriolis-induced displacement always has quadrature-phase relationship with the input drive signal, which facilitates rate demodulation by simply multiplying the Coriolis output with the drive signal, in a coherent AM demodulation scheme. However, at mode-split condition, if $\Delta\omega$ is comparable to the sense-mode BW, the AM demodulator phase-shift has to be adjusted accordingly in order to achieve maximum possible sensitivity.
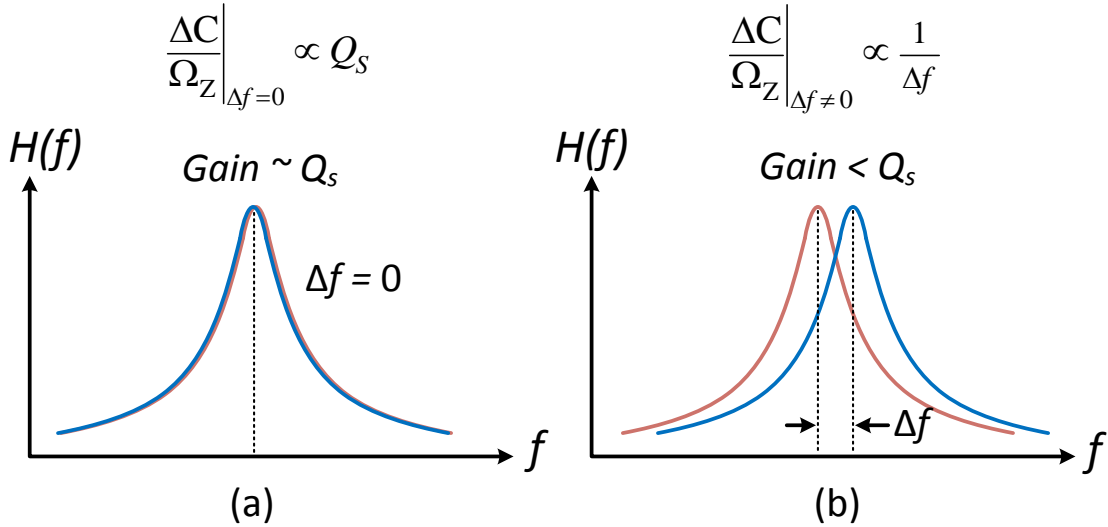
Figure 1.2: (a) At mode-matched condition gyroscope gain is directly proportional to sense-mode quality factor, (b) at mode-split condition gyroscope gain is inversely proportional to frequency split.

1.1.3 Gyroscope Response in the Presence of Stiffness and Damping Coupling

Practical implementations of micromachined MEMS gyroscopes suffer from undesired damping and stiffness coupling between the degenerate gyroscopic modes. While stiffness coupling is mainly caused by misalignments and fabrication imperfections [2], [8]-[9], existence of damping coupling is mainly attributed to either non-proportional damping [10], or to drive force coupling due to misalignments [2], [11], which can be affected by the device structure.

In case of stiffness coupling, an undesired force proportional to the displacement of the drive mode is generated in the sense-mode equation. Therefore, since the drive-mode displacement and velocity are 90° out-of-phase, the resulting undesired component of the sense output current has quadrature-phase relationship with the Coriolis component in the sense output, hence called quadrature signal. In case of damping coupling however, the coupling term is proportional to the velocity of the drive mode, in the same manner as the Coriolis coupling, making it difficult to distinguish rate from damping coupling.

The mathematical representation of a realistic gyroscope in presence of parasitic coupling terms can be described as:

$$\left(s^2 + \frac{\omega_x}{Q_x} s + \omega_x^2 \right) X(s) = \frac{F_x(s)}{m}, \ f_x(t) = F_0 \cos \omega_x t$$

$$\left(s^2 + \frac{\omega_y}{Q_y} s + \omega_y^2 \right) Y(s) = -\left(2s\lambda\Omega_z + s\frac{\omega_{xy}}{Q_{xy}} + \omega_{xy}^2 \right) X(s) \tag{1.8}$$

For simplicity, these coupling terms are neglected in the drive-mode equation, since the drive-mode energy loss due to these terms can always be restored by a gain-controlled drive oscillator loop.

The sense mode is actuated by the Coriolis force and the stiffness and damping coupling forces, resulting in:

$$y(t) \approx \frac{\left[2\lambda\Omega_z + \dfrac{\omega_{xy}}{Q_{xy}} \right] \dfrac{Q_x F_x}{\omega_x} \cos\left(\omega_x t + \varphi\right) - \dfrac{\omega_{xy}^{\;2}}{\omega_x^{\;2}} Q_x F_x \sin\left(\omega_x t + \varphi\right)}{m\omega_x \times \sqrt{\left(2\Delta\omega\right)^2 + \left(\omega_y/Q_y\right)^2}}, \quad \varphi \approx \tan^{-1} \frac{\omega_y/Q_y}{2\Delta\omega} \quad (1.9)$$

In a coherent AM demodulation scheme, given that the carrier signal is adjusted to be in-phase with the Coriolis component to achieve maximum SNR, the quadrature component can be rejected completely. However, the problem is that the magnitude of the uncompensated quadrature component in a MEMS gyroscope is typically 2-3 orders of magnitude larger than the full-scale range of the Coriolis signal [2]. Therefore, the quadrature component can saturate the sense front-end amplifiers and degrade the noise performance and dynamic range of the detection circuits [12]. The literature review in Chapter 3 of this dissertation will give an overview of different ways to cancel or compensate for quadrature at the device level or circuit level.

1.2   GYROSCOPE PERFORMANCE SPECIFICATIONS

A number of parameters are commonly used to describe the performance of MEMS vibratory gyroscopes. These parameters include scale factor, resolution, bias drift, dynamic range, and bandwidth [13]. These parameters are briefly discussed in this section, and an overview of how they can be used to analyze the performance of a gyroscope system is provided.

1.2.1   Scale Factor

Coriolis force causes deflection along the sense axis of a vibratory gyroscope. Scale factor, or angular rate sensitivity, of a vibratory gyroscope is the ratio of the change in the output signal, which can be sense-mode deflection, sense output current, or sense-mode capacitance variation, to the input signal, i.e. physical rotation.

Scale factor is typically measured in units of (pA/°/sec) or (mV/°/sec) depending on whether the sensor output current or the system output voltage is being reported.

The current sensitivity of a capacitive gyroscope can be expressed as:

$$I_{Coriolis} = \frac{2V_P C_{s0} Q_{eff} x_{drive}}{d_{s0}} \Omega_z \tag{1.10}$$

where V_P is the polarization of the capacitive device, C_{s0} is the sense capacitance at rest, d_{s0} is the sense gap at rest, and x_{drive} is the displacement amplitude of the drive-mode oscillation, also described by (1.6). At mode-matched condition, Q_{eff} is equal to the sense-mode quality factor, Q_s. In mode-split condition, Q_{eff} can be modified to match the sensitivity defined by (1.6). Mode-matching maximizes the gyroscope angular rate sensitivity, and thus increases the SNR of the front-end electronics.

1.2.2   Resolution

The resolution of a gyroscope is the minimum rotation rate that can be distinguished from the noise floor of the system per square-root of detection bandwidth, and is expressed in units of (°/sec/√Hz) or (°/hr/√Hz). The overall resolution of a gyroscope is mathematically defined by the total noise equivalent rotation (TNEΩ), which is comprised of two main components: mechanical noise equivalent rotation (MNEΩ), and electrical noise equivalent rotation (ENEΩ).

$$TNE\Omega = \sqrt{MNE\Omega^2 + ENE\Omega^2} \tag{1.11}$$

Mechanical and Electrical Brownian Noise

Mechanical noise is caused by the Brownian motions of the suspended mass along the sense axis. By equating the displacement caused by Brownian motion to the displacement caused by mechanical rotation, MNEΩ can be derived as:

$$MNE\Omega = \frac{1}{2x_{drive}} \sqrt{\frac{4k_B T}{\omega_s m Q_s}} \cdot \sqrt{BW} \tag{1.12}$$

where k_B is the Boltzmann constant (1.38×10^{-23} *Joules/K*), T is temperature in Kelvin, m is mass, ω_s is the sense-mode angular frequency, Q_s is the sense-mode quality factor, and BW is the measurement bandwidth (in units of Hz, unlike the rest of this thesis where BW is in units of rad/s).

Electronic noise of the circuits is dominated by the input-referred current noise of the sense pick-off circuits. Using the same method, the noise can be referred to input rotation of the device, to derive ENEΩ as follows:

$$ENE\Omega = \frac{d_{s0}}{2V_P C_{s0} Q_{eff} x_{drive}} \cdot I_{n,total} \cdot \sqrt{BW} \tag{1.13}$$

where $I_{n,total}$ is the total input-referred current noise of the sense pick-off electronics, and Q_{eff} is the same effective quality factor described in section 1.2.1. In other words, ENEΩ is the ratio of the input-referred current noise to the current sensitivity of the gyroscope.

As can be seen, both noise values are inversely proportional to the amplitude of drive-mode displacement, x_{drive}. Therefore, increasing the drive amplitude within the linear operation region of the actuator is commonly used to enhance the overall noise performance of the gyroscope system [14]-[15].

Mode-matching can significantly improve ENEΩ by increasing the current sensitivity and thus improving the SNR of the electronics interface [6], [14]. However, MNEΩ is not affected by the frequency split between the two modes, since the mechanical noise and the Coriolis-induced displacement see the same gain to the gyroscope output, and thus are affected equally by mode split and the transducer. The value of ENEΩ is typically designed to be sufficiently lower than MNEΩ, such that MNEΩ becomes the dominant contributor to the overall noise (TNEΩ). ENEΩ can be reduced by decreasing the input-referred current noise of the sense pick-off amplifiers by careful design.

1.2.3 Zero-Rate Output and Bias Drift

Zero-rate output (ZRO) is the output of the gyroscope in the absence of angular rotation. The long-term drift of the ZRO is called bias drift (measured in °/hr or °/sec) which shows the long-term stability of the gyroscope stationary output. The importance of bias stability is in the integration of the rate output to calculate angle and consequently the heading of the system. In such a case the long-term drifts of the sensor can accumulate and cause errors in the deduced orientation angle.

It can be understood from (1.9) that the drift of ZRO is most commonly attributed either to the drift of the DC terms caused by the stiffness and damping coupling, or to the drift of gyroscope transfer function with variations of mode-split, resonance frequency, quality factor, and transduction coefficient over time or environmental effects such as temperature, resulting in fake rate readout, thus errors e.g. in long-term navigation.

Allan Variance

Bias drift of a sensor is a statistical measure of how it performs over short or long periods of time, and as such, stochastic methods are used to model bias drift. The most useful and informative method is Allan variance [16]-[18], which is based on calculating standard deviation of the averages of clusters of different sizes, of a large array of bias-only samples of the sensor output. Allan variance can be mathematically represented as:

$$\sigma^2(\tau) = \frac{1}{2(n-1)} \sum_i \left(y(\tau)_{i+1} - y(\tau)_i \right)^2 \tag{1.14}$$

where $\sigma(\tau)$ is the root Allan variance as a function of averaging time τ, n is the total number of data clusters of size τ, and $y_i(\tau)$ is the average of the measurement in cluster i.

It can be understood that the root Allan variance at each τ is the standard deviation of the averages of τ-size data clusters. In other words, the value of $\sigma(\tau)$ at each τ, is a measure of the error between each two consecutive sample of averaging size τ. Therefore, if for instance the output solely contains thermal noise and no other drift errors, then both

11

the value of the averages of size τ, and the standard deviation of these averages, $\sigma(\tau)$, constantly decrease as τ increases. However, if the output bias monotonically drifts over time, e.g. due to temperature change, then with an increase in τ, the difference and thus the standard deviation between the averages of size τ will also increase. From an intuitive perspective, the root Allan variance can be considered as the probability and extent of having an erroneous bias output, after τ seconds of averaging. This intuition can be directly used to understand the stringent requirements of inertial sensors for navigation.

Figure 1.3 shows a sample plot of Allan variance analysis, in which the values of root Allan variance are plotted as a function of averaging time, τ, on a log-log scale [17]. The time-domain data from the stationary sensor contains contributions from different noise sources, each correlated to a different averaging time, and thus corresponding to different parts of the Allan variance plot. This allows for a thorough analysis of the time-domain drift behavior of the sensor. The main drift and noise components in a typical Allan variance plot are: quantization noise, angle random walk (ARW), bias drift, rate random walk (RRW), and rate ramp.

The random processes associated with these error terms can be assumed to be uncorrelated. Therefore, the total Allan variance at each τ can be calculated by:
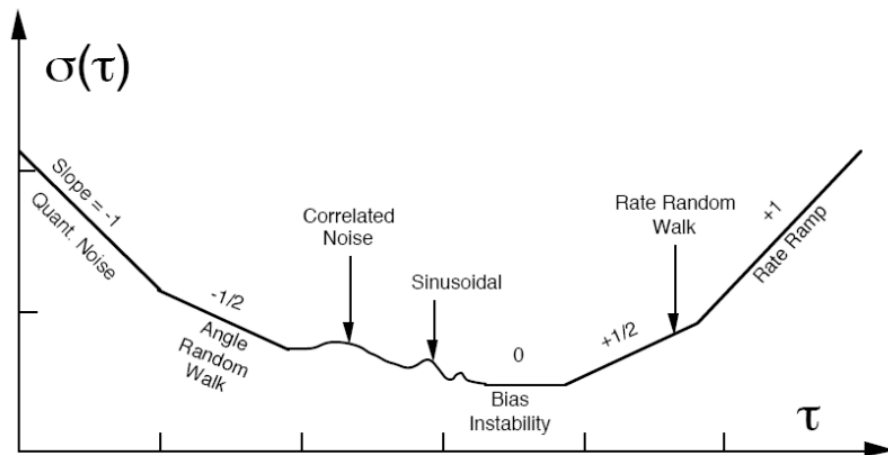
Figure 1.3: Typical Allan variance plot, showing different regions corresponding to different sources of noise and drift.

$$\sigma_{total}^2(\tau) = \sigma_{Quantization}^2(\tau) + \sigma_{ARW}^2(\tau) + \sigma_{Bias-drift}^2(\tau) + \sigma_{RRW}^2(\tau) \qquad (1.15)$$

Quantization noise:

Quantization noise is represented by the portion of the Allan variance plot that is proportional to $1/\tau$, i.e. has a slope of -1, when plotted in a log-log scale. The expression for quantization noise is given by [19]:

$$\sigma_{Quantization}^2(\tau) = \frac{\sqrt{3}Q_N}{\tau^2} \qquad (1.16)$$

where Q_N is equal to the quantization noise of the digitizer divided by the scale factor of the gyroscope. This component is measured at the lowest averaging times, as it relates to the high-frequency sampling at the output of the sensor. It should be noted that the derivation in (1.16) is for a uniformly distributed quantization noise in a simple Nyquist-rate analog-to-digital (A/D) converter. The formula will be different for a noise-shaped oversampled A/D converter backend.

Angle Random Walk:

Angle random walk (ARW) is the result of angle error build-up over time, due to white noise in the angular rate output. It can be shown that if the power spectral density (PSD) of the wideband white noise is given by $S_w(f) = N^2$, where N is the input-referred angular rate noise of the system (TNEΩ) in °/hr/√Hz, then the ARW variance is [19]:

$$\sigma_{ARW}^2(\tau) = \frac{N^2}{\tau} \qquad (1.17)$$

Based on the above, on a log-log scale Allan variance plot, ARW is represented by a straight line with a slope of -1/2, i.e. is a function of $\tau^{-1/2}$. The value of ARW can be found by fitting a line with a slope of -1/2 to the Allan variance plot, and reading the value of the line at $\tau = 1$ sec, which is equal to N. Typically, the Allan variance plot itself has $\tau = 1$ in its ARW region. Assuming that $\sigma(\tau)$ is plotted in units of °/hr, The value of ARW can be reported as the same value of N in units of °/hr/√Hz. However, it is more

13

common to report ARW as $N/60$, in units of °/√hr, to be directly used as a measure of short-term stability of the system. For instance, a gyroscope ARW of 0.01 °/√hr results in an integrated angle error of 0.005° after 15 minutes of integration. It must be noted that despite the reduction in the value of $\sigma(\tau)$ with τ, the heading error in the integrated output itself increases as the integration time increases. For instance, in the above example, if the integration time is increased to 1 hour, the integrated angle error increases to 0.01°.

Bias Drift:

It has been shown in [19] that the contribution of random low-frequency noise with $1/f$ PSD is a flat line with slope of zero on the Allan deviation plot. The value of the flat region in Allan deviation plot is called bias instability or bias drift, which represents the minimum achievable error between consecutive averages of size larger than the bias drift timescale. In other words, as long as the averaging time is shorter than that of the bias drift time constant, the error between consecutive averages reduces with the increase of τ. However, for averaging time beyond the bias drift time constant, this error will not reduce anymore.

Rate Random Walk and Rate Ramp:

Rate random walk (RRW) is a result of an unknown random process with acceleration PSD, creating a slope of +1/2 on the log-log Allan variance plot. It can be shown that RRW can be caused by demodulation of $1/f^2$ terms from the phase noise profile of the drive loop by the zero-rate output in the sense-mode response. While this error is less visibly seen in characterization results of this thesis, the rate ramp region with slope of +1 is more commonly recognized on most of the Allan variance plots.

Rate ramp is caused by deterministic sources of error that monotonically change the output over long periods of time [19]. The main source of this error is recognized to be environmental variations, which affect the gyroscope performance through changing the gyroscope transfer function and its resonance parameters. Temperature variation for instance, can cause drift of output bias by affecting the magnitude of the quadrature and

damping coupling terms, thereby changing the output bias terms at the demodulator output. Moreover, temperature variation can affect both resonance frequency and quality factor of the gyroscopic resonance modes, and consequently change the response of the gyroscope to the coupling terms.

In a coherent demodulation scheme, temperature-induced frequency shift does not affect the gyroscope performance directly as it does to a resonator structure, since both modes shift equally as a result of temperature variation. However, this frequency shift can change the output bias when the self-sustaining actuation signal is coupled to the sense-mode output current through reactive electrical coupling terms, such as capacitive feedthrough in package routings and Through-Silicon-Via (TSV) structures, or inductive coupling through long parallel unshielded signal pads on a PCB prototype or the interface IC. Reactive coupling can become a significant source of bias variation in high-frequency gyroscope structures, where higher oscillation frequency of the device generates larger levels of output bias and bias variation, for the same amount of capacitive or inductive coupling. In other words, in higher frequency gyroscopes, smaller coupling is needed to provide noticeable drift in the gyroscope bias, as compared to lower frequency gyroscopes. The relatively lower sensitivity of high-frequency gyroscopes further exaggerates the effect of such electrical couplings. This shows the significance of careful circuit implementation and sophisticated packaging for resonant Coriolis gyroscopes.

Determining Minimum Detectable Rotation Rate:

In an ideal gyroscope system where the output noise is only limited by the white noise contributions from both the MEMS element and the circuits, the minimum detectable rotation rate of a gyroscope is theoretically determined by knowing the ARW and bandwidth values. However, in a real gyroscope system, the other components of the Allan deviation plot described above also induce errors in the rate measurements. Besides thermal white noise, the flicker noise and the slowly varying temperature-induced drift are the two most common sources of long-term drift in MEMS gyroscope systems.

Figure 1.4 depicts the contributions of these drift and noise sources to the Allan deviation plot of a typical gyroscope. While the standard deviation of the error due to white noise reduces with the increase of averaging time, the flicker noise flattens the Allan deviation plot, implying that the error remains constant as the averaging time increases further. In the presence of slight temperature-induced drift, the rate error starts increasing with τ for above a certain value of τ, implying further increase in the integrated angle error than expected by only integrating the white and flicker noises. The time constant τ where the roll-up takes place, determines the optimum averaging size of the rate output for angle detection, with minimum error from long term drift of the gyroscope. This optimum averaging size determines the suitable sampling update rate for the navigation system, and the period at which the gyroscope needs temperature recalibration.

In the presence of large temperature drifts, the roll-up of the Allan deviation plot can take place at a smaller τ, resulting in a larger value of bias instability, as the temperature drift dominates the overall long term drift error. The reduction of the bias instability time constant, and more importantly the increase of the bias instability itself
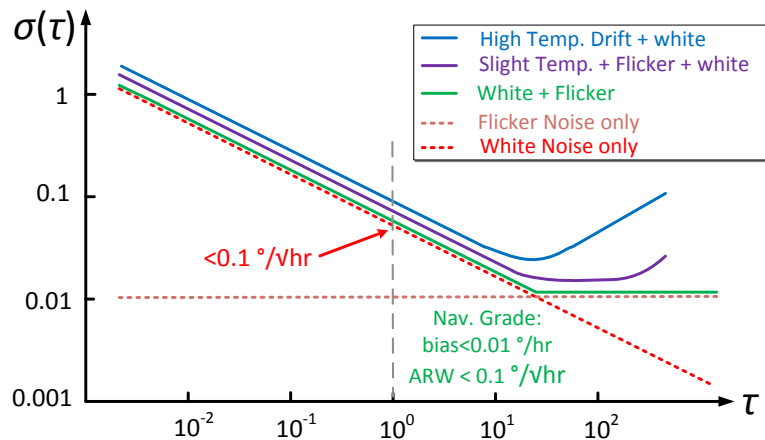
Figure 1.4: Allan variance for ideal gyroscope is dominated by ARW region only. For navigation-grade performance, ARW < 0.1 °/√hr and bias drift < 0.01 °/hr are required, while only flicker can affect the ARW-only trend of the Allan variance plot, and temperature effects are sufficiently compensated. Addition of slight temperature effects can cause roll-up of the Allan variance curve, while too much uncompensated temperature effect can roll up the curve before flicker affects it.

can be detrimental to any deduced reckoning operation using the gyroscope. Therefore, reduction of temperature effect on the drift of bias and scale factor is of utmost importance when considering the use of gyroscopes for navigation.

Flicker noise that comes from backend electronics, can be reduced by using all-digital architectures that utilize high-accuracy data converter interface to the analog signals. Using low-flicker bipolar devices rather than CMOS transistors for analog blocks can also reduce flicker further. Moreover, it can be shown that the phase noise profile of the drive signal, when demodulated by the ZRO contents of the sense signal, can demodulate into baseband $1/f^2$ noise that can result in rate random walk. Using lower flicker devices and architectures can result in lower drive loop phase noise.

Regarding temperature effects, besides using temperature compensation techniques, reducing feedthrough and inductive coupling in the system implementation can also reduce rate ramp in the overall gyroscope long-term bias performance.

With completely compensated temperature effects, in the presence of flicker and thermal noise sources only, the Allan variance plot looks closest to the green line in Figure 1.4, where the Allan deviation line flattens at the bias instability levels required by the desired application, e.g. < 0.01 °/hr for navigation, and remains at that level. To achieve this level of temperature compensation, sophisticated electrical calibration and temperature compensation techniques are required.

1.2.4 Bandwidth and Dynamic Range

Bandwidth (BW) of a gyroscope is a measure of its response time to input rotation changes. Bandwidth (single-sided bandwidth) of the sensor is related to the resonance frequency, f_0, and quality factor, Q by:

$$BW = \frac{f_0}{2Q}(Hz) = \frac{\omega_0}{2Q} \ (rad/s) \tag{1.18}$$

In this thesis $\omega_0/2Q$ is used as the definition of BW in most discussions.

Higher bandwidth provides faster response to rotation changes of the gyroscope. The bandwidth requirements of different applications are described in Table I. For instance, in pedestrian navigation application, where settling time is not an issue, a high-Q, thus high-resolution gyroscope is preferred, whereas in an automotive anti-skid control system where agile responses to quick unpredicted motions are required, high bandwidth is preferred over high resolution.

Dynamic range of a gyroscope is defined as the range between the minimum detectable rate, defined by TNEΩ, and the maximum detectable rate (full-scale rate) that the device can tolerate without significant mechanical nonlinearity. Excluding the nonlinearities and full-scale rate limitations caused by the transducer mechanism, the full-scale rate range of a gyroscope is defined by $BW \times 360$ °/s:

$$FS = BW \times 360 \qquad \left(°/s \right) \tag{1.19}$$

In (1.19), BW is measured in units Hz, implying that every cycle (1 Hz) of rotation stands for 360 °/s of rotation rate. This BW limitation of full-scale range will be mathematically proven and verified by simulations, in Chapter 2 of this dissertation. However, the nonlinearity caused by the transduction mechanism is not discussed in this dissertation; it should rather be discussed in the context of device design.

1.2.5 Scale Factor instability and Drift Mechanisms

According to the simplified equation (1.6), the scale factor of an AM gyroscope system depends on multiple parameters including the quality factors and frequencies of the two gyroscopic modes. Therefore, the stability of the gyroscope scale factor depends strongly on the stability of each of these parameters over time and temperature variation. While frequency variation with temperature is relatively low, in a range of 0.2-0.4% over the entire temperature range, the total quality factor variations can go up to 50%, which can affect the scale factor stability dramatically. Moreover, variations of mode-

split, $\Delta \omega$, can be a significant source of scale factor drift especially if the gyroscope is nominally operating at near-mode-matched condition.

Variation of mode-split can be mainly caused by variations of stiffness coupling between the two modes due to anisoelasticity [20]. Besides the effect of the parameter drifts on the amplitude of the sense-mode displacement, the phase of the sense signal also depends on the bandwidth and mode-split of the gyroscope, resulting in scale factor degradation and leakage of quadrature error into the in-phase rate output.

For penetration of the MEMS technology into high-end tactical market, scale factor stability of 100 ppm is required. This level of stability cannot be achieved without electrical compensation techniques and additional calibration layers.

1.3   MOTIVATION

With the ever-increasing interest towards navigation-grade gyrocompass, the need for reduction of all sources of drift in the performance of MEMS gyroscopes is more highlighted. Different techniques have been used over the past decade to partially compensate the long-term bias drift caused by stiffness and damping coupling terms of MEMS gyroscopes [21]-[22], mostly at the cost of increasing the ARW or reducing the operational bandwidth of the overall system.

Multiple techniques have also been explored to stabilize the transfer function of resonant MEMS gyroscopes by providing mode-matched condition automatically and maintaining it during the operation of the gyroscope [7], [14], [23]-[25]. The most efficient mode-matching techniques mostly rely on injecting external signals to the gyroscope and monitoring the phase relationship or amplitude minima of the gyroscope response, and then deducing the mode-matched condition based on its secondary effects on the system. However, besides the complicated algorithm implementations required for most of these schemes, their incapability in providing a direct measure of the split

between the mode frequencies makes these techniques prone to variations in both electronics and device parameters that are used to monitor the effect of mode split.

Regarding scale factor stabilization, force-to-rebalance architecture [24], [26], has been used to make the gyroscope transfer function independent of the quality factor variations. However, the scheme introduces more challenges regarding the stability of the force-feedback controller and overall power consumption.

The main goal of this research is to develop a novel scheme for MEMS resonant gyroscope interface that provides means to compensate long-term drifts in both bias and scale factor and to also enable robust in-run mode-matching, paving the path towards zero-drift performance on both bias and scale factor. The system solution developed and characterized in this thesis improves the bias performance of a BAW disk gyroscope by almost an order of magnitude, down to sub-$10°$/hr levels, while achieving up to 45 times reduction in temperature drift of bias, and up to 150 times reduction of scale factor long-term drift, without affecting the noise or operation bandwidth of the gyroscope system.

1.4   THESIS ORGANIZATION

The remainder of this dissertation is organized as follows. Chapter 2 provides a circuit model of resonant gyroscopes, followed by open-loop analysis and simulation of the gyroscope mode responses with and without mode coupling terms and rotation, to show the effect of each term on the gyroscope transfer function and behavior.

Chapter 3 provides a system-level understanding of interface systems for MEMS resonant gyroscopes. A brief introduction of high-frequency BAW gyroscopes is provided, followed by a detailed analysis of different components of coherent AM demodulation interface architecture for gyroscopes. The analysis provides a good understanding of the different challenges in gyroscope interface systems and clarifies the impact of each challenge on the noise and drift performance of the overall gyroscope system.

Chapter 4 presents an electrical tuning technique for linear bidirectional frequency tuning of MEMS resonators, specifically for MEMS piezoelectric and piezoelectric-on-Silicon resonators and resonant sensors. The significance of the tuning technique is that it provides means to mimic the effect of different force terms in the equations of MEMS resonators and resonant sensors, including gyroscopes. The technique presented in Chapter 4 will provide the basic principles for the scale factor calibration method introduced in Chapter 5 of this dissertation.

Chapter 5 presents the core idea of this dissertation, which is a dual-mode actuation and sensing scheme for axisymmetric resonant gyroscopes. The dual-mode interface system with inherent bias calibration and in-run mode-matching capability will be explained and the sensitivity and SNR advantages will be analyzed and simulated. Then the scale factor calibration technique, inspired from the dynamic electromechanical resonator tuning scheme of Chapter 4, will be introduced. Performance of the overall sensor with bias and scale factor calibration will be presented and analyzed. The equations of the system are then solved with more details of the effects of circuit nonidealities, and simulation and measurement results that show the efficacy of the self-calibration techniques.

Chapter 6 concludes this work by summarizing the contributions, followed by a detailed analysis of the major risks associated with the use of the proposed self-calibration techniques, and proposes solutions to those risks, which leads to directions on future work towards achieving a zero-drift gyroscope using the proposed self-calibrated dual-mode gyroscope architecture.

CHAPTER 2

CIRCUIT MODELING OF CORIOLIS RESONANT GYROSCOPES

The design concept behind mainstream commercial MEMS Coriolis gyroscopes has been based on mode-split tuning fork structures for a long time [27]-[29]. To interface such structures, a simple yet useful assumption is to take the drive mode as the only mode that couples into the other mode, i.e. the sense mode, and neglect the coupling effects of the sense mode back to the drive mode. It will be shown in Chapter 3 how this is taken care of in most conventional MEMS gyroscope interface architectures. This assumption helps minimize the amount of circuit and MEMS co-simulation, as the designer only has to design a drive oscillator loop to actuate the drive-mode resonator into constant oscillations, and separately design a sense front-end to amplify the Coriolis-induced sense current to be demodulated with the drive signal. Despite being simple, mode-split operation has not been able to provide high-resolution and low-drift performance, resulting in higher demand on mode-matched operation that can provide larger scale factor and higher precision for industrial and navigation applications.

In the case of mode-matched gyroscopes, as far as high-sensitivity rate detection and low-noise performance are concerned, the above-mentioned interface approach still works. However, without a good understanding of the coupling effects and mode-split on the operation of the overall system, developing low-drift system architectures can become overly complicated. To alleviate this complexity, an accurate yet flexible circuit model of the gyroscope is required. A comprehensive model can pave the path towards generation of new ideas for gyroscope interface, specifically the ones that involve actuation of both gyroscope modes such as those described in [30]-[33].

Gyroscope models are typically created in MATLAB or generated by Verilog-A codes in Cadence, to be used together with the interface circuits directly [34]. However, in this work the modeling and simulation has been done all with linear circuit

components for better understanding. Interestingly, the modeling effort has resulted in the resonator tuning ideas presented in Chapter 4 of this thesis.

2.1 BASIC MEMS RESONATOR MODEL

The basic mathematical model of a MEMS resonator is described by:

$$m\frac{d^2x}{dt^2} + d\frac{dx}{dt} + kx = f_0(t) \tag{2.1}$$

The electrical equivalent circuit model of the resonator in the mechanical domain is shown in Figure 2.1a, in which all displacements and forces are represented by electrical charges and voltages, respectively. Consequently, all velocities are represented by electrical currents. Accordingly, the mass-spring-damper components are replaced with *L-C-R* components, respectively. In this model, the *L-C-R* values are equal to the mass-spring-damper values, and the input mechanical force is applied as a voltage to the series tank model. In real world, this input force is generated by applying an electrical voltage to the input electrode of the device, modeled by a transformer with coupling coefficient η, as shown in Figure 2.1b. The transformer represents the transduction mechanism that is used to actuate the resonator and sense its displacement. Therefore, the value of the transduction coefficient, η, can be used to determine the accurate values of the *R*, *L*, *C* components and forces in the electrical series tank of Figure 2.1b. Different transduction mechanisms such as capacitive transduction, piezoelectric transduction, etc. can be used in MEMS devices for actuation and sensing. It can be shown for instance that for a parallel-plate capacitive transducer:

$$\eta = V_P\frac{C_0}{d_0} = V_P\frac{\varepsilon_0 A}{d_0^2}, \tag{2.2}$$

where V_P is the polarization voltage of the capacitive device, C_0 is the rest capacitance, A is the area of the electrode, and d_0 is the rest gap of the parallel-plate electrode.
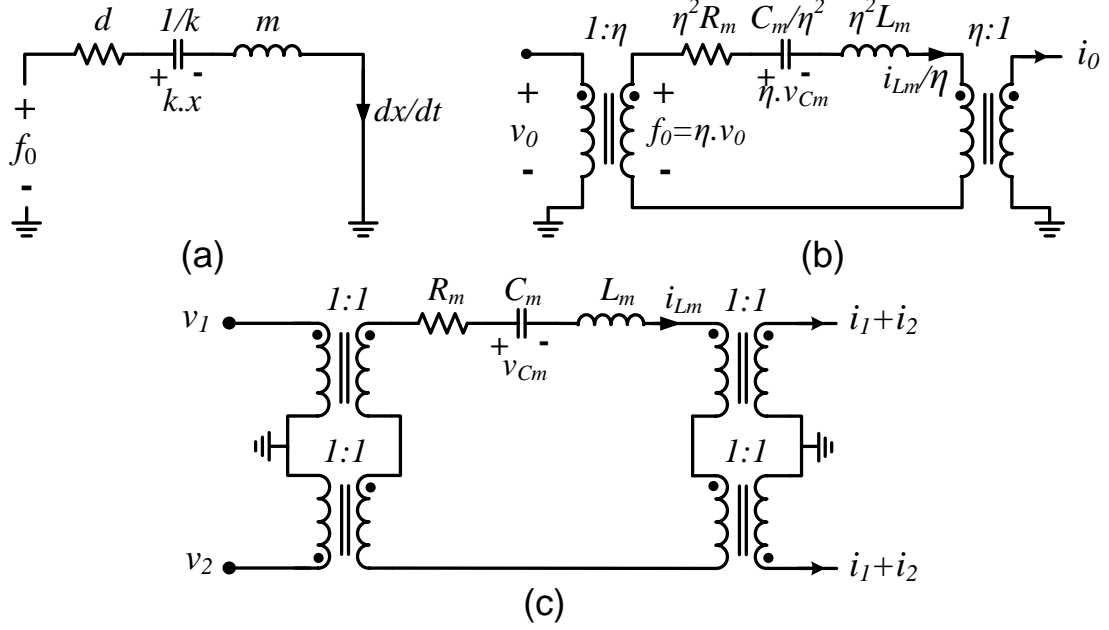
Figure 2.1: (a) Electrical circuit model of an electromechanical resonator; all forces are replaced with voltages, and all displacements are replaced with electrical charges, **(b)** electrical circuit model of the electromechanical resonator with actuation and sensing electrodes modeled as transformers with coupling of η, **(c)** a multi-port resonator model; multiple electrodes on a resonance mode are modeled by multiple series transformers.

Based on the above discussion, the value of the input excitation force f_0, is given by $f_0 = \eta \cdot v_0$. Alternatively, as shown in Figure 2.1c, the resonator mass-spring-damper values can be replaced with equivalent L_m-C_m-R_m values, while the resonant series tank is actuated with voltage v_0, using 1:1 transformer ratios for both actuation and sensing. In this model, the resonator equation will be:

$$L_m \frac{d^2 q}{dt^2} + R_m \frac{dq}{dt} + \frac{1}{C_m} q = v_0(t)$$

$$q = \eta x, \; v_0 = \frac{f_0}{\eta}, \; L_m = \frac{m}{\eta^2}, \; R_m = \frac{d}{\eta^2}, C_m = \frac{\eta^2}{k}. \tag{2.3}$$

Figure 2.1c also shows that in n a multiport resonator, the electrodes are modeled by series transformers that add up multiple forces applied to the resonator ports. This feature is used in this work to apply tuning and calibration forces to resonators and resonant gyroscope modes, as will be described in Chapter 4 and Chapter 5 of this thesis.

24

2.2   GYROSCOPE BASIC MATHEMATICAL MODEL

The basic mathematical model of a Coriolis gyroscope is described by (1.2). In order to generate a circuit model of the complex equation, the electrical analogue of each mechanical term is used, in a similar manner as described for the MEMS resonator in the previous section. Consequently, (1.2) can be represented in the electrical domain as:

$$L_m \frac{di_{Lx}}{dt} + R_x i_{Lx} + \frac{1}{C_x} q_{Cx} + \frac{1}{C_{yx}} q_{Cy} + R_{yx} i_{Ly} = v_x(t) - 2L_m \lambda \Omega_z i_{Ly}$$

$$L_m \frac{di_{Ly}}{dt} + R_y i_{Ly} + \frac{1}{C_y} q_{Cy} + \frac{1}{C_{xy}} q_{Cx} + R_{xy} i_{Lx} = v_y(t) + 2L_m \lambda \Omega_z i_{Lx}, \tag{2.4}$$

where i_{Lx} and i_{Ly} represent the current of each inductor, equivalent to the velocities of each mode, and q_{Cx} and q_{Cy} represent the charges on each capacitor, equivalent to the displacements of each mode. In the above equation, the representations of the stiffness and damping coupling terms have also been modified to equivalent capacitance and resistance coupling terms accordingly, where $C_{xy} = C_{yx}$, and $R_{xy} = R_{yx}$. The value of mass is considered the same for both modes.

Figure 2.2 shows the schematic of the electrical circuit model of a Coriolis gyroscope. Each resonance mode of the gyroscope is modeled by an RLC tank, while the coupling terms of each mode are modeled by dependent voltage sources that are controlled by the capacitor charge or inductor current of the other mode. Specifically in
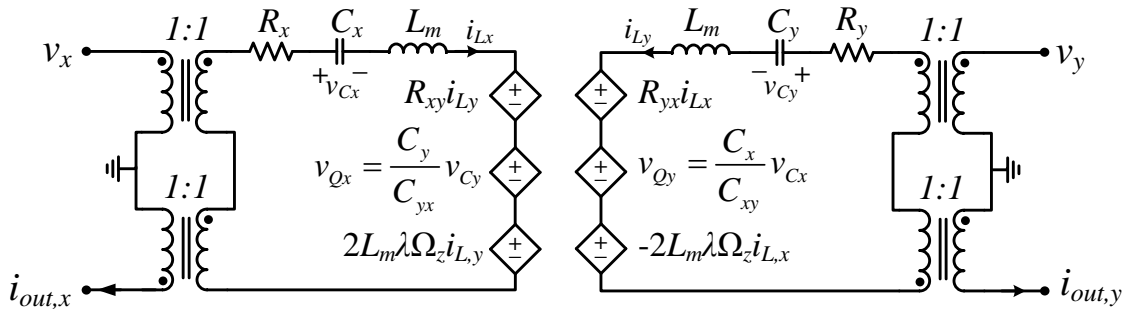
Figure 2.2: Electrical circuit model of a Coriolis gyroscope; each resonance mode of the gyroscope is modeled by an RLC tank, while the coupling terms of each mode are modeled by dependent voltage sources that are controlled by the capacitor charge or inductor current of the other mode.

this case, the damping coupling is modeled by a current-controlled voltage source (CCVS) and the stiffness coupling is modeled by a voltage-controlled voltage source (VCVS) with their gains calculated using the device parameters. Coriolis force is also modeled by a CCVS with a gain of $2L_m\lambda\Omega_z$. It must be noted that the rate Ω_z used in the model is in units of rad/s. To apply rate in units of °/s, the gain of the Coriolis CCVS must be scaled by $\pi/180$.

2.3   COMPLETE CADENCE MODEL FOR RESONANT GYROSCOPE

With the model of Figure 2.2, most features of the open-loop behavior of a Coriolis gyroscope can be studied. However, for the purpose of interface circuit design, the model needs to provide two other important capabilities: application of time-varying rotation rates to the gyroscope, and tuning the mode frequencies with DC control voltages, similar to electrostatic spring-softening effect in capacitive resonators and gyroscopes (described in more detail in section 4.1.1).

Figure 2.3 shows an expanded circuit model of resonant gyroscopes that can be
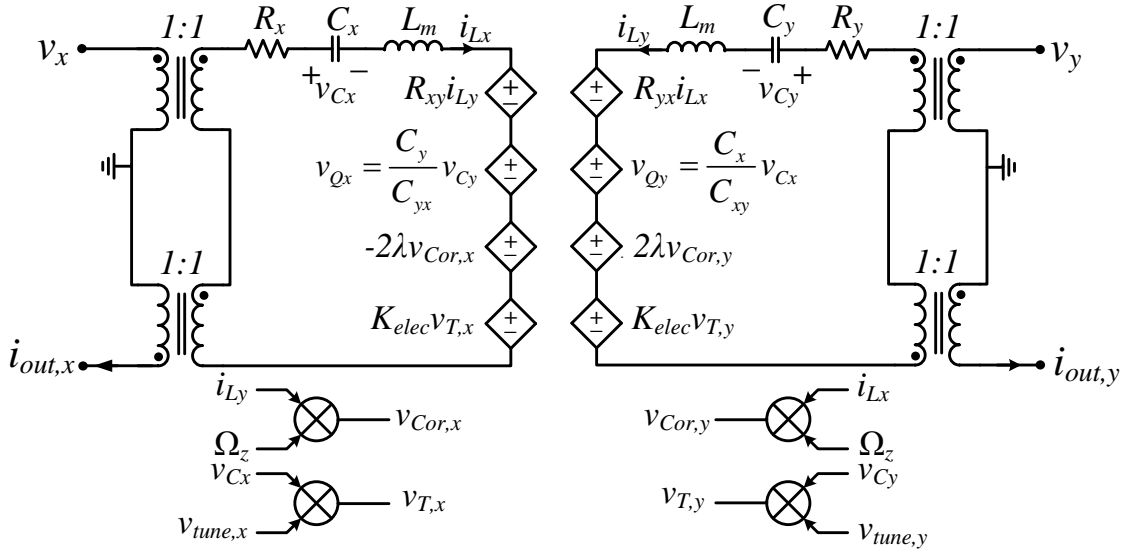
Figure 2.3: Complete circuit model of gyroscope for circuit simulation software; the Coriolis force and tuning force are generated by multiplication of the corresponding mode parameter, i.e. current or charge, by a user-defined scaling, to provide capability of simulating the effect of time-varying rotation, and to enable simulation of control circuits and algorithms for mode-matching.

26

practically used in circuit simulator software to comprehensively evaluate the performance of a gyroscope with time-varying rotation, and also facilitate the design and simulation of a mode-matching control circuit. In this model, the Coriolis signal is generated by a multiplier that modulates the mode velocity terms, i.e. the inductor currents, by an external user-defined voltage that represents physical rotation rate.

To provide tuning capability to each of the modes, the corresponding displacement signal of the individual mode, i.e. its capacitance charge, is scaled by a certain voltage and is applied as a series tuning force to the resonator. In the differential equation of the mode, the voltage used for scaling, tunes the stiffness coefficient of the resonance mode, thereby tuning its resonance frequency. This scaling voltage can be a DC tuning voltage or the output of a mode-matching controller circuit.

2.4   OPEN-LOOP ANALYSIS OF MEMS GYROSCOPE MODEL

The model of Figure 2.3 is used in this section, together with more mathematical analysis to study the effect of stiffness coupling and rotation on the open-loop transfer function of the gyroscope and its implications on closed-loop operation.

The *R-L-C* parameters in the model are chosen such that a quality factor of 2,000 is provided at 2.625 MHz resonance frequency, for each mode. The motional resistance R_m, for each mode is chosen to be 100 kΩ, and the motional capacitance C_m, and motional inductance L_m, are 303.15 aF and 12.1261 H, respectively. While the specific resonance frequency in the model is chosen to match that of the actual device under test, the quality factor value used in the model is almost 20 times lower than that of the actual device, for the sake of faster settling in time-domain simulations. The motional resistance values are also 3-4 times larger than that of the actual device, characterized in Chapter 5. It is noteworthy that in all simulations, the values of the applied rotation rate are represented fractions of the 3-dB single-sided bandwidth (*BW*) of the gyroscope modes, to provide a general intuition to the effects of nonlinearity and mode mismatch errors.

Figure 2.4a shows the frequency response of a stationary mode-split gyroscope that has no mode coupling errors. A frequency split of $\Delta\omega = \omega_0/Q$ is created between the modes by applying an appropriate DC voltage to the tuning multiplier input, $V_{tune,y}$. Two transimpedance amplifiers (TIA) with gain of 100 kΩ are used to pick-off the x-mode and y-mode output current signals, while in each case the measured mode is also being actuated. The plotted magnitude and phase outputs are corresponding to the output voltages of the TIAs. Therefore, as expected from theory, at resonance frequency, the magnitude response has a gain of 0 dB, where the phase response crosses 0°.

Figure 2.4b shows the effect of quadrature on the response of a mode-matched ($\Delta\omega = 0$) gyroscope. The blue full-line in both magnitude and phase responses show the gyroscope response when the x mode is actuated and sensed. Since no rate is applied, the
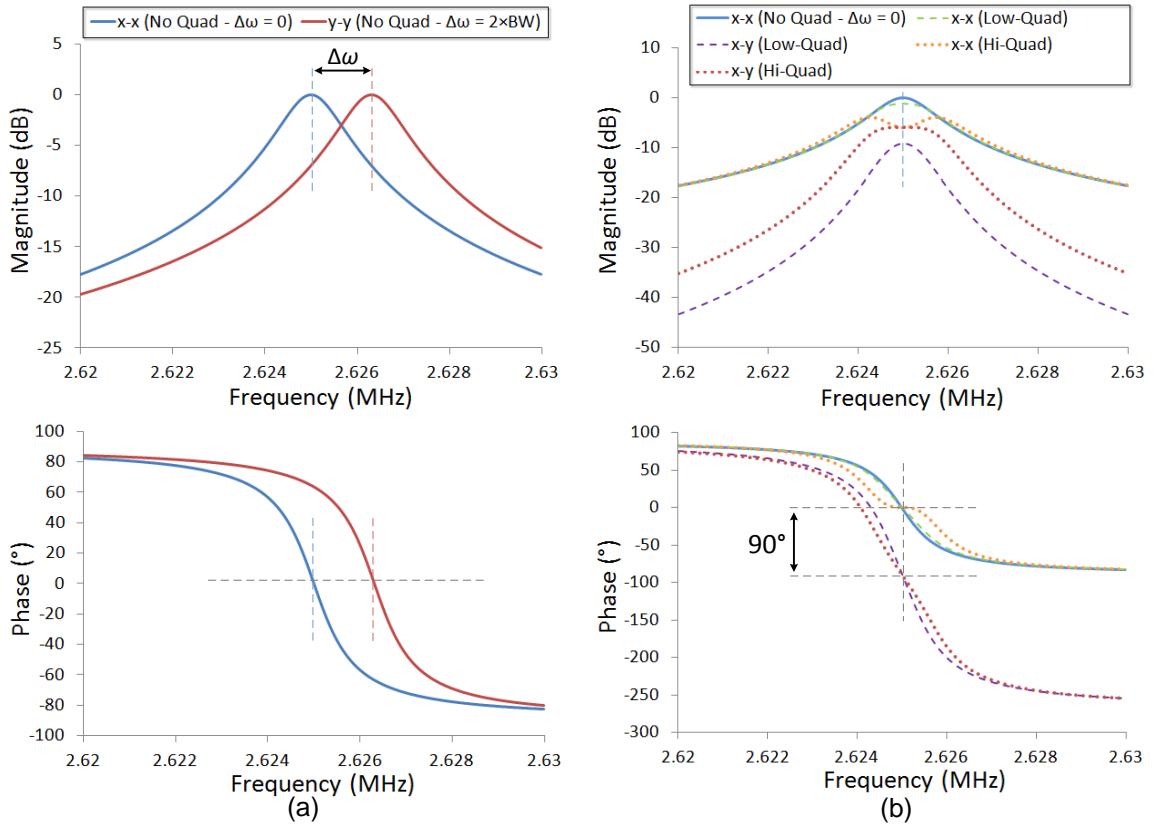
Figure 2.4: (a) Magnitude and phase response of individual modes of a gyroscope with a split of $\Delta\omega = 2 \times BW$, (b) in presence of quadrature coupling at mode-matched condition, the gyroscope shows a mode-split behavior; the amount of split becomes larger as the quadrature coupling increases, as explained by (2.6).

magnitude of the *y* mode would be zero. The dashed lines and dotted lines show the gyroscope magnitude and phase responses in presence of a relatively low quadrature coupling, and a relatively high quadrature coupling, respectively. As can be seen, if the quadrature coupling is sufficiently low, the green dashed lines, representing the *x*-output/*x*-input response remain relatively close in shape and value to the perfectly aligned gyroscope. In this case, the *y*-output/*x*-input response shows a peak at the same natural resonance frequency of the modes, where the quadrature force couples the *x*-mode energy into *y*-mode vibration. The phase of this signal crosses 90° at resonance, as expected from its quadrature-phase relationship with the *x*-mode output current.

When the quadrature amplitude increases, it not only increases the magnitude of the *y*-mode response, but it also creates a split between the degenerate gyroscope modes [20]. The mode split can be seen on both *x* and *y* outputs. It can be shown that if the quadrature increases further, the *x* output phase response will show two additional zero-crossings, which complicate the solution to the drive loop lock-in frequency.

The mode splitting caused by coupling terms can be explained by solving for the Eigen values of (1.3) in the Laplace domain. For simplicity, it is assumed that the two modes are accurately identical, i.e. $\omega_x = \omega_y$, and $Q_x = Q_y$, and also the damping coupling terms and rotation are excluded from the system of equations here. In presence of the stiffness coupling terms only, the solutions to the system of equations in (1.3) is:

$$\begin{vmatrix} s^2 + \dfrac{\omega_0}{Q}s + {\omega_0}^2 & {\omega_{xy}}^2 \\ {\omega_{xy}}^2 & s^2 + \dfrac{\omega_0}{Q}s + {\omega_0}^2 \end{vmatrix} = 0 \Rightarrow \begin{cases} s_{1,2} = -\dfrac{\omega_0}{2Q} \pm j\omega_0\left(1 - \dfrac{\omega_{xy}^2}{2\omega_0^2} - \dfrac{1}{8Q^2}\right) \\ s_{3,4} = -\dfrac{\omega_0}{2Q} \pm j\omega_0\left(1 + \dfrac{\omega_{xy}^2}{2\omega_0^2} - \dfrac{1}{8Q^2}\right) \end{cases}. \quad (2.5)$$

The two positive imaginary answers to the equations are the desired mode frequencies, which disregarding the real part and the effect of the $1/Q^2$ term, can be simplified to:

$$s_{1,3} \approx j\omega_0 \left(1 \pm \frac{\omega_{xy}^2}{2\omega_0^2}\right),$$ (2.6)

in which the difference between the two frequencies, ω_{xy}^2/ω_0, is directly proportional to the amount of stiffness coupling. In the simulations of Figure 2.4b, the value of ω_{xy}^2/ω_0 is equal to $0.02 \times BW$, and $2 \times BW$, for low- and high-quadrature cases, respectively.

In the conventional gyroscope system described by (1.8), in presence of sufficiently small stiffness coupling, the drive loop still approximately locks into the center of the x-mode (drive-mode) peak. Therefore, if the y-mode (sense-mode) natural frequency, ω_y, is matched to that of the x-mode, ω_x, the sensitivity is still at its maximum, considering slight degradation due to the existence of mode coupling terms in the system determinant, that increase the denominator of the sense-mode response. In conclusion, the split caused by sufficiently small mode-to-mode coupling does not necessarily affect the frequency-matched condition in a gyroscope. However, for characterization purposes, it is still important to be able to distinguish whether the mode split seen in the open-loop response of the gyroscope is caused by mode coupling, or by the mismatch of the natural frequencies of the two modes, i.e. ω_x and ω_y, to be able to compensate for each effect. A simple way to determine the existence of mode coupling in the open-loop response of a gyroscope is to look into the sense-mode magnitude response. Yet the sense-mode response alone cannot be used to determine the existence of frequency split.

Figure 2.5 shows the open-loop response of the same gyroscope in presence of both mode split ($\Delta\omega = 2 \times BW$), and same levels of quadrature used in simulations of Figure 2.4. In Figure 2.5a, the two full lines show the individual mode responses for a mode-split gyroscope without any mode coupling. The rest of the dashed and dotted lines show the response of the two modes to x-mode actuation. As can be seen from the x-mode outputs, by introducing a relatively small quadrature coupling, the x-mode output
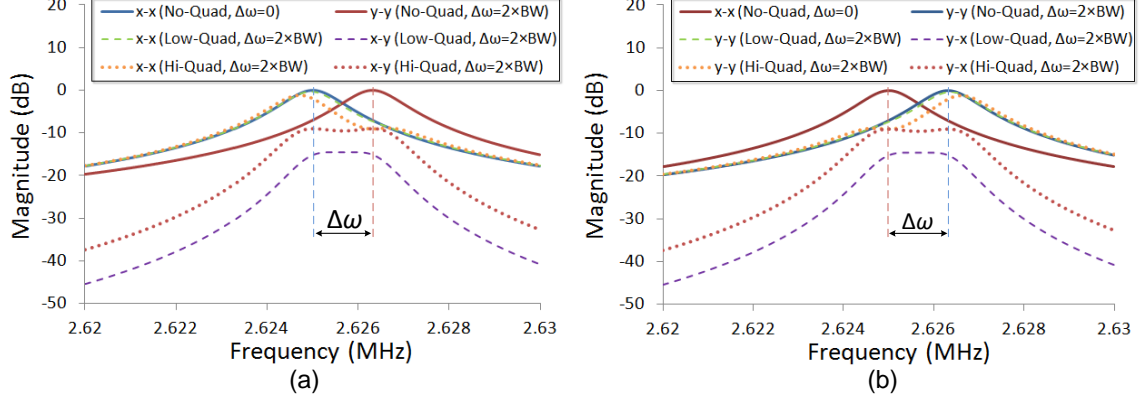
Figure 2.5: Effect of quadrature on mode-split gyroscope: (a) *x*-mode is actuated and both mode outputs are sensed, (b) *y*-mode is actuated and both mode outputs are sensed; the effect of quadrature is identical on the mode outputs. As quadrature increases, the output magnitude increases at the frequency of the drive mode, and decreases at the frequency of the sense mode.

becomes slightly asymmetric. As the amount of coupling increases, a second peak appears near the *y*-mode frequency, where the *x-y* quadrature force actuates the *y* resonance mode. The asymmetry is caused by the fact that the quadrature force in the *y*-mode equation is generated off-resonance with respect to ω_y, and therefore has smaller gain than the peak of the *x* mode. Figure 2.5b shows identical results for when the *y* mode is actuated in presence of mode-split and quadrature coupling. The results are the mirror of those plotted in Figure 2.5a, with respect to the average of the two mode frequencies, i.e. $\omega_0 = (\omega_x + \omega_y)/2$.

As can be concluded from both Figure 2.4 and Figure 2.5, in presence of both mode-split and quadrature, the drive-mode magnitude in each case shows an asymmetric profile with respect to ω_0, while in the absence of mode split, the drive output remains symmetric regardless of the amount of quadrature coupling. Moreover, the sense-mode output is symmetric with respect to ω_0, with and without quadrature or mode split. Therefore, for an axisymmetric gyroscope, an asymmetric profile in the drive-mode response corresponds to frequency split between the gyroscope modes. Furthermore, the amount of quadrature itself can still be analyzed by looking into the sense-mode magnitude response. However, by using this type of open-loop analysis one cannot

guarantee accurate frequency matching and alignment of the two modes. A scheme is required to determine each effect, and null them to zero to provide stable low-noise and high-sensitivity performance.

While quadrature nulling has been used in literature, using electrostatic alignment electrodes and continuous quadrature monitoring in closed-loop schemes [8]-[9], no method offers direct monitoring of frequency split of the modes. The dual-mode interface scheme proposed in Chapter 5 of this thesis will provide a thorough analysis of how this frequency split can be continuously monitored in presence of rotation, and utilized for the purpose of automatic in-run mode-matching.

Besides the undesired stiffness and damping coupling terms in MEMS gyroscopes, the Coriolis force also provides velocity coupling between the two modes. However, unlike the relatively constant or slowly varying nature of mode coupling terms, Coriolis magnitude depends on the amplitude of the time-varying mechanical rotation, with rate frequencies of up to a few tens of Hz depending on the application. As a result, the energy transfer from the drive mode to the sense mode has a time-varying nature, which results in a time-varying behavior of the gyroscope nonlinearities, as will be discussed in more detail in section 3.2.1.

In presence of mechanical rotation, the solutions to the gyroscope system of equations in (1.3) will be:

$$
\begin{vmatrix} s^2 + \dfrac{\omega_0}{Q}s + \omega_0^{\,2} & -2\lambda\Omega_z s \\[2mm] 2\lambda\Omega_z s & s^2 + \dfrac{\omega_0}{Q}s + \omega_0^{\,2} \end{vmatrix} = 0 \Rightarrow
\begin{cases}
s_{1,2} = -\dfrac{\omega_0 - \lambda\Omega_z}{2Q} \pm j\omega_0\left(1 - \dfrac{\lambda\Omega_z}{\omega_0} + \dfrac{1}{2}\left(\dfrac{\lambda\Omega_z}{\omega_0}\right)^2 - \dfrac{1}{8Q^2}\right) \\[5mm]
s_{3,4} = -\dfrac{\omega_0 + \lambda\Omega_z}{2Q} \pm j\omega_0\left(1 + \dfrac{\lambda\Omega_z}{\omega_0} + \dfrac{1}{2}\left(\dfrac{\lambda\Omega_z}{\omega_0}\right)^2 - \dfrac{1}{8Q^2}\right)
\end{cases}
, (2.7)
$$

which shows how the response of the gyroscope varies with mechanical angular rotation. In presence of rotation, not only the imaginary parts, but also the real parts of the solutions change in opposite directions. The split of the real parts in response to rotation,

changes the time constants of the responses of the gyroscope modes, in opposite directions. The positive imaginary parts of the solution can be written as follows:

$$s_{1,3} = -\frac{\omega_0 \pm \lambda\Omega_z}{2Q} + j\omega_0 \left(1 \pm \frac{\lambda\Omega_z}{\omega_0} + \frac{1}{2}\left(\frac{\lambda\Omega_z}{\omega_0}\right)^2 - \frac{1}{8Q^2}\right). \tag{2.8}$$

Assuming that $\Omega_z \ll \omega_0$, and $Q \gg 1$, the solution can be simplified to:

$$s_{1,3} = -\frac{\omega_0 \pm \lambda\Omega_z}{2Q} + j\omega_0 \left(1 \pm \frac{\lambda\Omega_z}{\omega_0}\right), \tag{2.9}$$

showing that the amount of mode split is equal to $2\lambda\Omega_z$. Figure 2.6a shows the same behavior in the drive-mode response of the mode-matched gyroscope, in the absence of any other mode coupling errors. With the application of rate, the magnitude of the drive
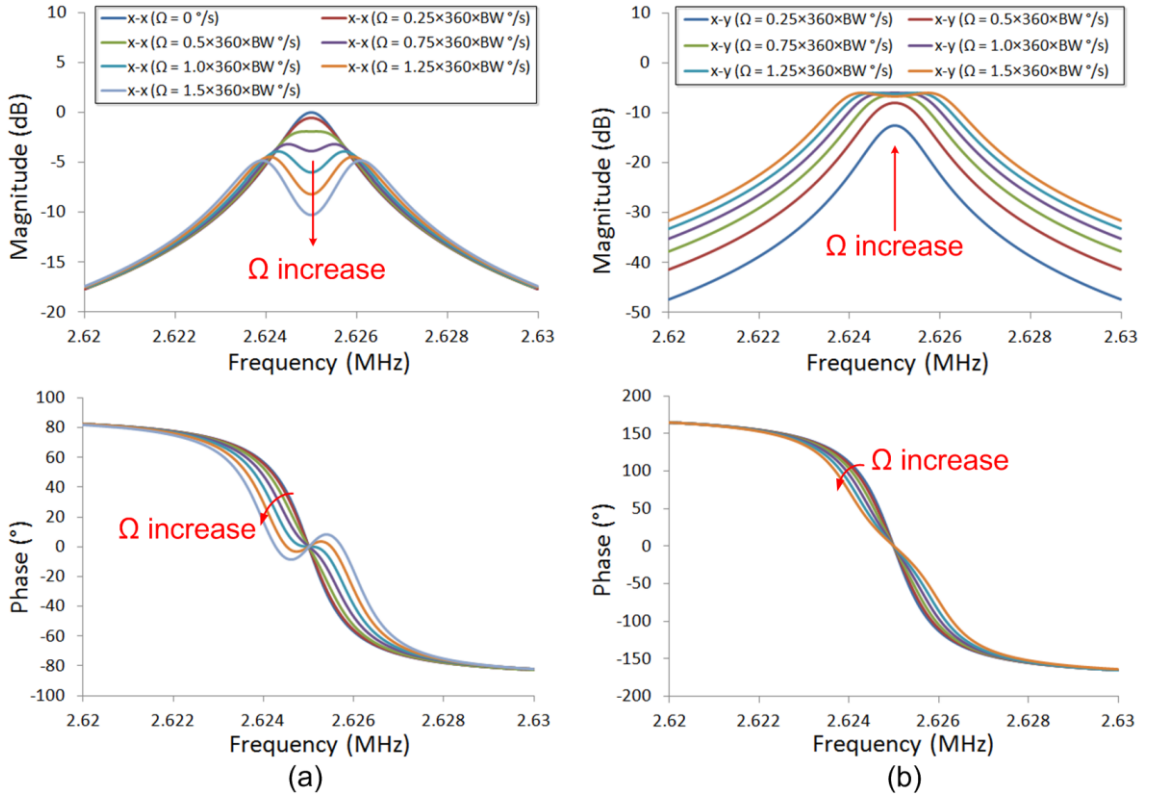
Figure 2.6: Open-loop frequency response of the gyroscope in presence of rotation; (a) drive-mode output, and (b) sense mode output; it can be shown that increasing in mechanical rotation can create a split between the gyroscope mode frequencies.

33

mode reduces at ω_0, due to the increase of energy transfer from the drive mode to the sense mode. At the same time, an increase in the magnitude of the sense-mode response can be seen in Figure 2.6b. Beyond a certain level of angular rotation rate, the rate-induced mode split becomes large enough to start creating a notch at ω_0, in the magnitude response of the sense mode.

The phase response of the drive loop shows an interesting behavior. The sharp slope of the phase response at ω_0 begins to decrease as the angular rate increases, up to $2\lambda\Omega_z = \omega_0/Q$, where the slope of the phase response at ω_0 becomes zero. Beyond this limit, the phase response begins to show two additional zero-crossings. This can cause the drive loop to lock into the lower frequency zero-crossing, resulting in dramatic change of the sense output in response to the new excitation frequency. This is discussed further in section 3.2.1, and the conventional compensation technique will be presented.

The development of the two additional phase zero-crossings can also be explained mathematically. Assuming equal quality factor values at mode-matched condition, in the absence of mode coupling terms, and in presence of rate, with $F_x = F_0$, and $F_y = 0$, the gyroscope system of equatins in (1.3) can be solved to derive x-mode (drive-mode) displacement as follows:

$$\begin{bmatrix} H(j\omega) & -2j\lambda\Omega_z\omega \\ 2j\lambda\Omega_z\omega & H(j\omega) \end{bmatrix} \begin{bmatrix} X(j\omega) \\ Y(j\omega) \end{bmatrix} = \begin{bmatrix} F_0 \\ 0 \end{bmatrix}, \quad H(j\omega) = \omega_0^2 - \omega^2 + j\frac{\omega_0\omega}{Q}, \tag{2.10}$$

resulting in:

$$X(j\omega) = \frac{H(j\omega) \times F_0}{H^2(j\omega) - 4\lambda^2\Omega_z^2\omega^2}. \tag{2.11}$$

Finding the zero-crossings in the phase response of the drive-mode output current at different mechanical rates is equivalent to finding the 90°-crossing points in the displacement output of (2.11), as follows:

$$\sphericalangle X\left(j\omega\right) = \tan^{-1}\frac{\dfrac{\omega_0\omega}{Q}}{\omega_0^2 - \omega^2} - \tan^{-1}\left[\frac{2\dfrac{\omega_0\omega}{Q}\left(\omega_0^2 - \omega^2\right)}{\left(\omega_0^2 - \omega^2\right)^2 - \left(\dfrac{\omega_0\omega}{Q}\right)^2 - 4\lambda^2\Omega_z^2\omega^2}\right] = \frac{\pi}{2} \qquad (2.12)$$

One obvious answer to the above equation is $\omega = \pm\omega_0$, which makes the first *arctan* term equal to 90°, while making the second *arctan* term equal to zero, and thus makes the overall phase equal to 90°, accurately. The other two answers can be found by simplifying (2.12) into the following equation:

$$1 + \left(\frac{\dfrac{\omega_0\omega}{Q}}{\omega_0^2 - \omega^2}\right) \times \left(\frac{2\dfrac{\omega_0\omega}{Q}\left(\omega_0^2 - \omega^2\right)}{\left(\omega_0^2 - \omega^2\right)^2 - \left(\dfrac{\omega_0\omega}{Q}\right)^2 - 4\lambda^2\Omega_z^2\omega^2}\right) = 0 \qquad (2.13)$$

which yields:

$$\omega_{90°}^2 = \omega_0^2 + 2\lambda^2\Omega_z^2 - \frac{1}{2}\left(\frac{\omega_0}{Q}\right)^2 \pm \omega_0\sqrt{\left(2\lambda\Omega_z\right)^2 - \left(\frac{\omega_0}{Q}\right)^2} \qquad (2.14)$$

showing that for values of $\lambda\Omega_z$ smaller than the gyroscope single-sided bandwidth (*BW*), there will be no additional phase zero-crossings in the drive output current transfer function. However, for $\lambda\Omega_z$ values exceeding the *BW*, two additional phase zero-crossings are generated, as previously shown by simulations.

CHAPTER 3

SYSTEM LEVEL CONSIDERATIONS FOR MEMS GYROSCOPES

This chapter explores system-level considerations in design of interface circuits for resonant gyroscopes. A brief overview of the advantages of high-frequency BAW gyroscopes and their implications on gyroscope system design is provided, followed by more details of conventional coherent demodulation interface architectures for MEMS resonant gyroscopes. The main building blocks of such interface architectures include a drive loop for self-sustaining actuation of the gyroscope, a sense front-end for Coriolis current pick-off, and a coherent demodulation circuit for detection of AM-modulated rate signal. The basics and challenges in design and implementation of these building blocks will be presented. Additionally, conventional methods of quadrature cancellation in resonant gyroscopes will be discussed, and advanced architectures will be explored.

3.1   MEMS RESONANT GYROSCOPES – DEVICE OPERATION

Similar to the tuning fork described in Chapter 1, MEMS vibratory gyroscopes can detect rate through Coriolis effect. The next three subsections describe the basic operation principles of the high-frequency axisymmetric BAW disk gyroscopes and substrate-decoupled BAW (SD-BAW) gyroscopes.

3.1.1   Axisymmetric Bulk Acoustic Wave (BAW) Disk Gyroscopes

Most commercially available gyroscopes are asymmetric TFG-like devices, in which the sense and drive frequencies are determined independently by the stiffness of different springs that allow motion along each axis [14], [15]. Having different tuning mechanisms for each mode makes mode matching more difficult. Therefore, these devices typically operate at mode-split condition, where the sense mode has a higher frequency than the drive mode. In order to compensate for the reduced sensitivity, the gyroscopes are designed at lower frequencies (< 20 kHz) with more compliant tethers to

allow for larger sense-mode displacements. However, the low-frequency nature of these devices makes them less immune to vibration and shock. An alternative way of implementing MEMS vibratory gyroscopes is to use the spatially orthogonal degenerate modes of axisymmetric structures such as rings, shells, or disks [35], [36]. The rate detection mechanism is similar to conventional asymmetric gyroscopes. However, in axisymmetric gyroscopes, both modes can be interchangeably used for actuation and sensing, as the two modes are inherently identical. Figure 3.2a shows the SEM photo of such an axisymmetric BAW gyroscope device. Figure 3.2b shows the elliptical mode shapes of two orthogonal degenerate $n = 3$ modes of the 24-electrode disk gyroscope shown in Figure 3.2a. By V_P polarization of the disk, the two modes can be electromechanically actuated and sensed at their respective antinodes, where the mode has its maximum displacement. In this structure, each one of mode-1 and mode-2 has 6 antinodes. The solid and dotted mode shapes represent the two opposite-phase half-cycles of periodic vibrations of each mode. The nodes of each mode are the zero-displacement points that are located in between of each two antinodes of the same mode. For an ideal circular structure, the radial displacements of the modes around the disk are given by:

(a)   (b)
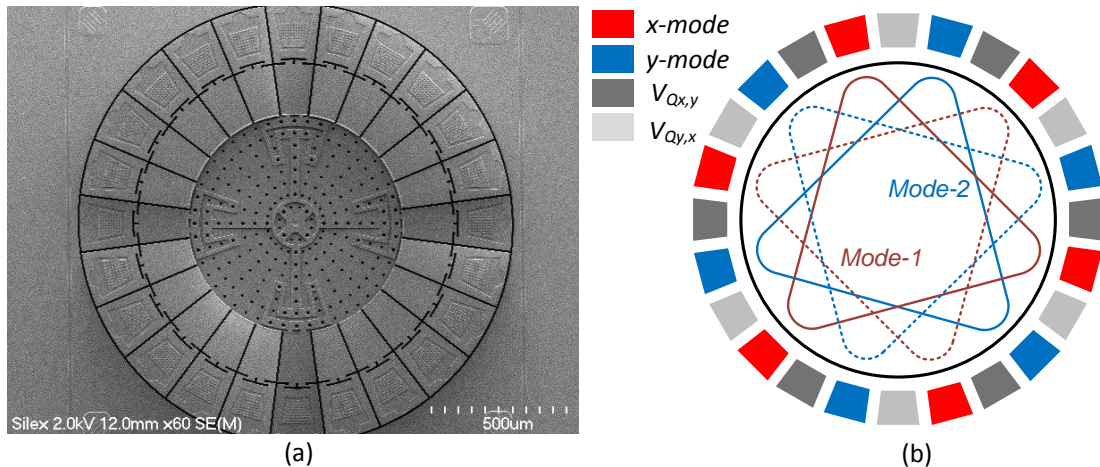
Figure 3.1: (a) SEM photo of a 24-electrode BAW disk gyroscope, (b) two degenerate $n = 3$ mode shapes of a BAW disk gyroscope are shown in blue and red; straight lines and dotted lines show the opposite-phase cycles of each mode. Red and blue electrodes represent the antinodes of the x and y modes, respectively, while the dark grey and light grey electrodes represent the quadrature electrodes, located at equal distance from each two consecutive antinodes of the two modes.

$$\phi_{r1}(\theta) = \cos(3\theta - \theta_0)$$
$$\phi_{r2}(\theta) = \sin(3\theta - \theta_0),$$
(3.1)

where θ_0 is the offset angle of the electrode with respect to the *x*-axis. The nodes of each mode coincide with the antinodes of the other mode. Therefore, it can be concluded that the two $n = 3$ degenerate modes are orthogonal with angular spacing of $\pi/6$. The antinode locations of each mode can also be used for electrostatic frequency tuning of the respective mode to provide mode-matched condition.

The 24-electrode disk gyroscope shown in Figure 3.2 has 12 quadrature electrodes that are each located in between two adjacent antinodes of mode-1 and mode-2. It can be seen in Figure 3.2b that the two modes have equal transduction at these electrode locations. It has been shown in [20] that DC electrostatic tuning can be used at these 12 electrode locations for tuning of spring imbalances.

Due to the relatively high stiffness of the bulk acoustic modes, the resonance frequency of these gyroscopes is typically orders of magnitude higher than that of the tuning-fork gyroscopes [35]. As a result, these devices can provide orders of magnitude higher operation bandwidth, while having the same quality factor as the TFG structures. However, the higher stiffness of the BAW gyroscopes results in lower sensitivity as compared to the lower frequency gyroscopes. To increase the current sensitivity of the BAW gyroscopes, the gap size is reduced to hundreds of nanometers using HARPSS process [37]. The reduced gap size increases the capacitive coupling on the parallel-plate electrodes, and thus increases the current sensitivity of the device, thereby reducing the motional resistance to only a few tens of kΩ.

Another structural difference between axisymmetric gyroscopes and tuning-fork gyroscopes is the constant, λ, that accompanies angular rate, Ω_z, as described in (1.3), in axisymmetric gyroscopes, unlike in tuning-fork gyroscopes where $\lambda = 1$. This constant indicates the angular gain of the gyroscope, which is the portion of energy that is

transferred from one mode to the other, in an axisymmetric gyroscope, in response to applied rotation. In a TFG-like gyroscope where the direction of displacement of different modes is well-defined along perpendicular axes, the energy is completely transferred from one mode to the other. However, in axisymmetric gyroscopes, the displacement of each mode has both radial and tangential components, resulting in reduced coupling of the Coriolis energy between the modes. The amount of reduction is defined by angular gain, λ, which is a function of the geometry and mode order [38].

3.1.2 Effect of Substrate Anisotropy

The radial displacement described by (3.1) is valid for $n = 3$ modes of gyroscopes fabricated on isotropic substrates. Two examples of isotropic substrates are polycrystalline silicon and single-crystalline silicon (SCS)-(111). However, it has been shown in [39] that SCS-(111) is not a good choice for $n = 3$ elliptical degenerate modes of a disk structure, due to the relatively large frequency splits caused by the out-of-plane anisotropy of this substrate. The use of polycrystalline silicon substrate is typically limited in terms of the maximum thickness of the substrate and the overall cost of using this substrate. Therefore, anisotropic SCS-(100) remains the least expensive and most practical choice for exploiting such elliptical degenerate modes in disk structures.

Anisotropy of SCS-(100) can be described by Figure 3.2, where the radial displacements of both degenerate $n = 3$ modes of a disk structure are plotted as a function of angle location around the disk, for both isotropic substrate and SCS-(100) substrate. The radial displacement for isotropic disk is shown in Figure 3.2a, where the displacement is described by (3.1). However, in anisotropic disk, the locations of nodes and antinodes coincide only in four locations around the disk, located at $\pm 45°$, and $\pm 135°$, spaced every $90°$, as shown in Figure 5.18b.

It has been shown in [39] that the radial displacement of the $n = 3$ modes of a solid disk in SCS-(100) can be approximately expressed as:
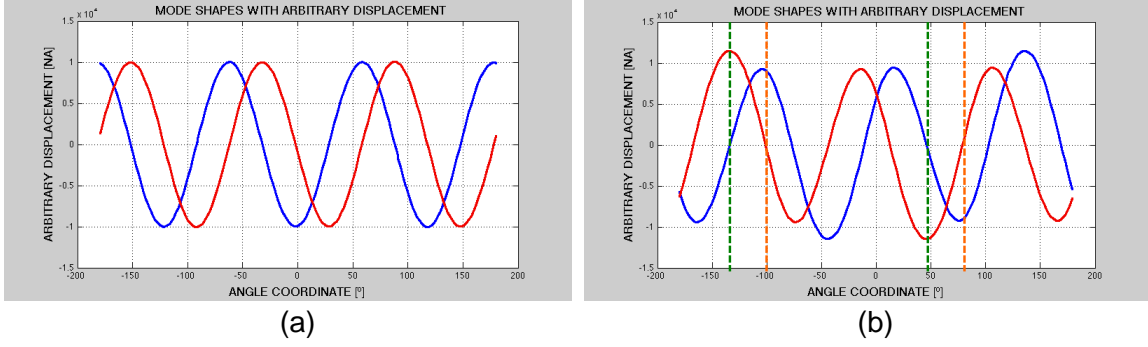
Figure 3.2: Radial displacement of the n=3 degenerate modes (mode 1 in blue, and mode 2 in red) as a function of the disk angle in (a) isotropic substrate, (b) anisotropic (100) SCS substrate.

$$\phi_{r1}(\theta) = \cos(\theta_0 - 3\theta) - \frac{1}{6}\cos(\theta + \theta_0)$$

$$\phi_{r2}(\theta) = \sin(\theta_0 - 3\theta) - \frac{1}{6}\sin(\theta + \theta_0), \tag{3.2}$$

which shows that the mode shapes of the anisotropic disk have harmonic components besides the fundamental components described by (3.1). It can also be shown that in a hollow disk, the coefficient of the additional harmonics, i.e. $\cos(\theta)$ and $\sin(\theta)$ terms, decreases as the inner diameter gets closer to the outer diameter. As an example, in the extreme case of a hollow disk, i.e. an annulus structure, the coefficient of the additional harmonics decreases to as low as 0.01, which can be considered equivalent to isotropic material, depending on the desired accuracy.

Based on Figure 3.2 and comparing equations (3.1) and (3.2), it can be understood that for an anisotropic disk with $n = 3$ modes:

1) The maximum deflections at the antinodes of a particular mode are not equal. Therefore, applying the same force at different antinode locations could result in different displacements. This can show up as insertion loss mismatch between the gyroscope modes.

2) The antinodes of each mode are equally spaced by 60°, but the nodes are not. As a result, the nodes of one mode are not always coinciding with the antinodes of the other, as also explained earlier. This affects the placement of actuation and

sensing electrodes for the two modes. For instance, assuming that in single-mode actuation scheme, the drive-mode actuation electrode is placed at 45° angle, then the antinodes of the drive mode are aligned with this direction. This means that the antinodes of the sense mode are located at 135° and 315° angles, as these are the only locations that the antinodes of the sense mode and nodes of the drive mode coincide. Sense electrodes placed at any other sense-mode antinode locations (15°, 75°, 195°, or 255°) will pick off small amounts of the drive mode that will show up as ZRO. This ZRO can have both in-phase and quadrature-phase components.

3.1.3 Substrate-Decoupled BAW Gyroscope

The major limitation of center-supported BAW disk gyroscopes is the effect of environmental error sources on the gyroscope performance, due to mechanical coupling of these errors from the substrate through the central anchor to the resonating disk structure. In order to reduce the effect of substrate coupling, the resonant structure should be decoupled from the substrate.

A substrate decoupled BAW (SD-BAW) gyroscope is developed in [39], in which a decoupling spring structure is used in between the resonating structure and the substrate, to guarantee minimum energy transfer from one to the other, and thus reduce the substrate coupling effect. Figure 3.3a shows the $n = 3$ mode shapes of the decoupled structure. Figure 3.3b shows the SEM picture of the hollow disk gyroscope device with the decoupling structure in the middle of the disk, designed and fabricated by Qualtré Inc. [40]. Figure 3.3c shows the die photo of the gyroscope device used in this work for prototype development and characterizations of Chapter 5. The hollow disk has an inner radius of 245 μm, an outer radius of 325 μm, and thickness of 40μm, with 290nm capacitive gaps. The wafer-level packaged die has a vacuum of 1-10 Torr. The gyroscope

41
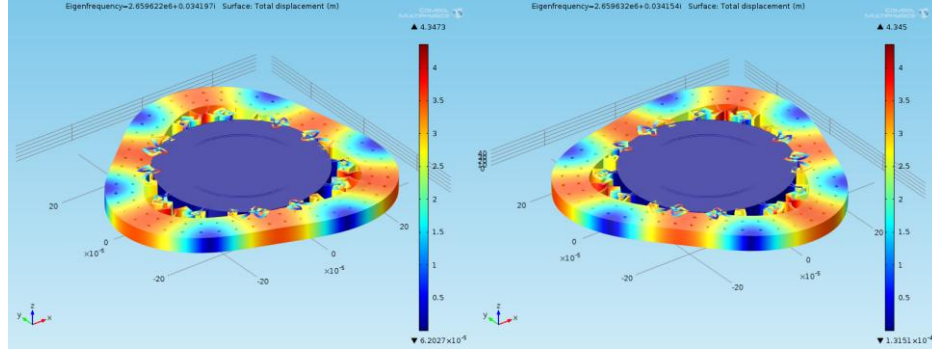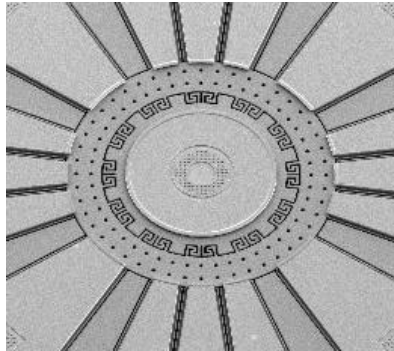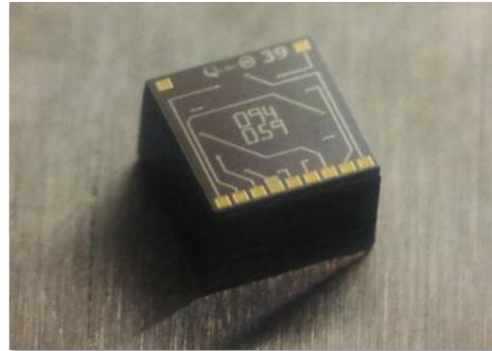
Figure 3.3: (a) elliptical degenerate n=3 modes of the hollow disk structure, (b) SEM photo of the hollow disk structure with decoupling structure in the middle of the disk, (c) wafer-level packaged gyroscope die, designed and fabricated by Qualtré Inc. [40].

modes have resonance frequencies of ~2.625 MHz, motional resistance of ~32.67 kΩ, and quality factors of ~37,000.

3.2   SELF-SUSTAINING DRIVE LOOP

To actuate the drive mode of a gyroscope to maximum displacement, a self-sustaining oscillator loop should be implemented that locks into the peak of the resonance mode. The Barkhausen criteria require the oscillator loop to provide 360° overall phase shift and a total loop gain higher than unity at the peak frequency of the desired mode. In practice, in a MEMS resonator, multiple parasitic resonance modes also exist. In order for the oscillator loop not to lock into those modes, either the phase of the modes should be adjusted to be significantly different than 360°, e.g. 180°, or the gain of the loop should be chosen lower than unity.

Figure 3.4 shows the general architecture of a drive oscillator loop, where a transimpedance amplifier (TIA) is used to amplify and convert the resonator output current to voltage, with 180° phase shift from the actuation signal phase. The voltage is then post-amplified by an inverting variable-gain amplifier (VGA) which provides gain or attenuation to the TIA signal to provide an overall gain of unity at all times to the entire loop, and thereby maintain stable oscillation at the desired amplitude according to the Barkhausen criteria.

An automatic gain control (AGC) sub-block in used to control the gain of the VGA by monitoring the deviation of the input drive voltage or the TIA output voltage from a specific reference level, V_{ref}, and nulling the difference to zero by means of a PID controller. It can be shown that for controlling the input drive force to remain constant, an integrating controller is sufficient, while for stabilizing the output of the TIA, and thereby stabilizing the resonance velocity, a PI controller is needed. While stabilizing the drive signal amplitude can be practiced for MEMS resonators, in the interface of MEMS gyroscopes, the AGC is typically used to stabilize the drive-mode TIA output, thereby stabilizing the drive-mode velocity at all time. This will be discussed in more detail in the
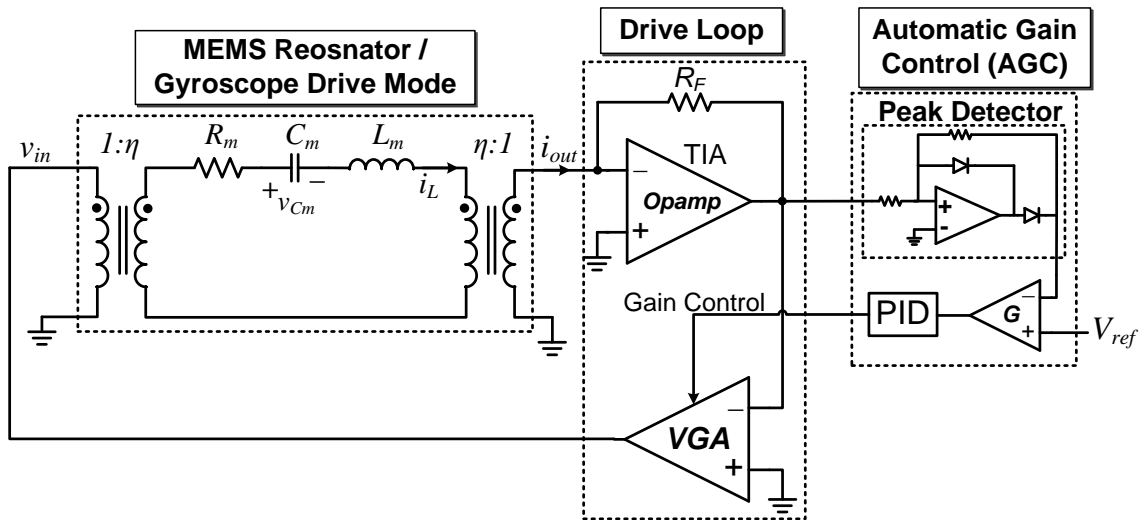
Figure 3.4: General architecture of a drive loop used for self-sustaining actuation of the drive mode. A TIA is used to pick-off the drive-mode current. A VGA provides gain control to stabilize the velocity of the drive mode, and thus stabilize the Coriolis force.

next subsection 3.2.1.

Another function of the AGC is to help with the startup of the oscillator, by increasing the gain of the VGA to maximum when the signal level is at its minimum, i.e. zero oscillation. Moreover, the AGC can guarantee a clean sinusoidal oscillation, rather than a railed and typically square-wave oscillation, which can cause ground bouncing, thereby coupling to the sense front-end and demodulator back-end, creating errors in the rate output.

Another sub-block in many drive loop circuits is a phase shifter that compensates slight phase inaccuracies of the drive loop amplifiers. For instance, for a high-frequency resonance mode, the TIA phase might deviate from 180°, and thus cause the oscillator loop to lock into slightly different frequency than the actual center frequency of resonance, to compensate for the phase variation by means of the sharp phase transition of the resonator itself. In most resonator applications, locking into the series mode resonance, i.e. the center of the resonance peak, is not necessary. For instance, in most commercial implementations of quartz crystal resonator, a single inverter is used to take advantage of the parallel resonance mode and lock into another frequency other than that of the series mode [41]. However, in mode-matched MEMS gyroscopes it is desired that the drive loop locks into the series mode resonance, to create maximum displacement for maximum sensitivity and minimum noise performance.

3.2.1 Using AGC to Compensate the Effect of Coriolis Force on Drive Loop

In MEMS gyroscope interface, the AGC loop is used to stabilize the TIA output peak amplitude, thereby stabilizing the drive-mode velocity to keep the Coriolis force constant in presence of all MEMS parameter variations, e.g. due to environmental changes. Another significant advantage of using AGC to stabilize drive-mode velocity is to compensate for the energy loss in the drive mode due to the application of mechanical rate and even slowly-varying mode coupling terms.

It can be shown that by applying force F_0, the energy stored in each single mode of an ideal stationary gyroscope is equal to:

$$E_D = \frac{1}{2}mv_D{}^2 = \frac{Q^2 F_0{}^2}{2m\omega_0{}^2}, \; E_S = 0 \tag{3.3}$$

In presence of mechanical rotation, Ω_z, the energies can be written as:

$$E_D = \frac{1}{2}mv_D{}^2 = \frac{F_0{}^2}{2m} \frac{\left(\frac{\omega_0}{Q}\right)^2}{\left[\left(\frac{\omega_0}{Q}\right)^2 + \left(2\lambda\Omega_z\right)^2\right]^2}, \; E_S = \frac{1}{2}mv_S{}^2 = \frac{F_0{}^2}{2m} \frac{\left(2\lambda\Omega_z\right)^2}{\left[\left(\frac{\omega_0}{Q}\right)^2 + \left(2\lambda\Omega_z\right)^2\right]^2} \tag{3.4}$$

where part of the drive-mode energy is transferred to the sense mode through Coriolis coupling. It can be concluded that at a constant force, due to the loss of energy caused by applying rate, the velocity of the drive mode drops as rotation rate increases. Using an AGC to regulate the drive-mode TIA output voltage helps restore the lost energy back to the drive mode, thus keep the Coriolis force stable. The lost energy is restored by increasing the applied force to the drive mode input.

From another intuitive perspective, according to (2.7) the determinant of the gyroscope system increases in value as the applied rate increases. Therefore, the velocity of the drive mode decreases, and thus the AGC helps restore the velocity back to the same reference value by applying a larger force to the drive mode.

3.2.2 Effect of Capacitive Feedthrough on Drive Loop

In a packaged MEMS resonator or gyroscope die, the capacitive coupling between different routing traces and the coupling created by Through-Silicon-Vias (TSVs) in the packaging [42] can cause capacitive feedthrough across the drive mode, as shown in Figure 3.5a. As a result of such feedthrough, the magnitude response of the resonance peak changes as described by Figure 3.5b (top), where an anti-resonance is created at a frequency of:
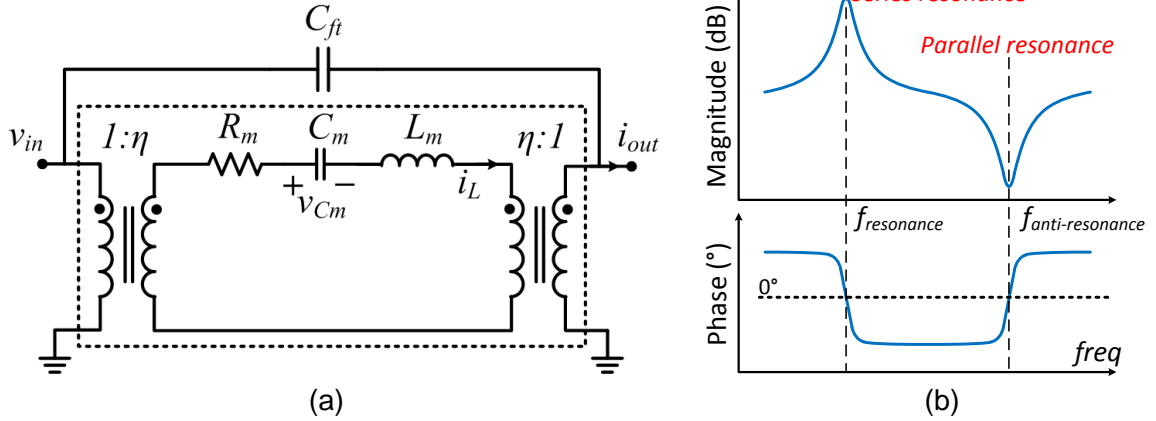
Figure 3.5: (a) resonator model with parasitic feedthrough capacitance, (b) capacitive feedthrough creates an anti-resonance in the magnitude response of the resonator. At the anti-resonance frequency the phase response of the resonator rolls back up; very large feedthrough can make the phase response roll back up before its zero-crossing, and thus mask the phase zero-crossing.

$$f_p = \frac{1}{2\pi\sqrt{L_m \dfrac{C_{ft}C_m}{C_{ft}+C_m}}} \;,$$ (3.5)

where f_p refers to parallel-mode resonance. The phase response of the resonance peak is shown in Figure 3.5b (bottom), where the resonator current phase has 0° transition points at both the series and parallel resonance frequencies.

It can be understood from (3.5) that for a larger C_{ft}, the frequency f_p becomes closer to the series-mode resonance frequency, f_c. If f_p falls too close to the series resonance, f_c, the phase may roll back up before it even reaches the 0° point, and thus prevent a series-mode oscillator from locking into oscillation. The amount of feedthrough capacitance in most packages typically ranges from 50fF to 200fF. The responses of Figure 3.5b are plotted for C_{ft} = 50fF, and C_m = 140aF.

If the feedthrough capacitance is large enough to prevent a locking, a feedthrough cancellation circuit (Figure 3.6a) can be used in parallel with the resonator to provide a negative feedthrough capacitance across the resonator, thus cancel the feedthrough effect completely, at the cost of added noise. Figure 3.6b shows a comparison of a resonance
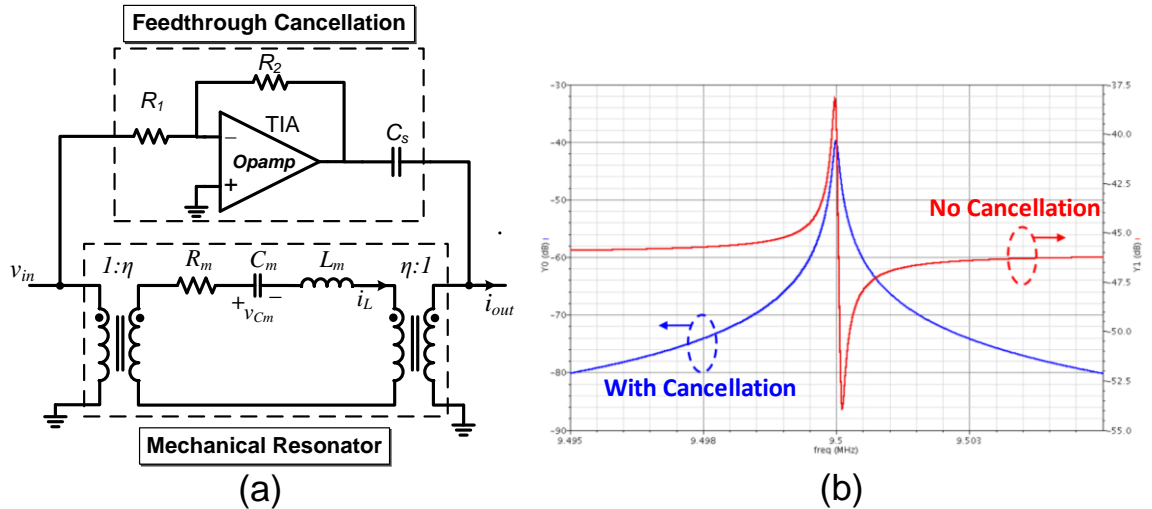
Figure 3.6: (a) feedthrough cancellation circuit comprised of an inverting amplifier followed by a series capacitor to provide negative capacitance in parallel with the parasitic feedthrough, (b) Simulated magnitude response of the resonance peak with feedthrough, with and without feedthrough cancellation.

mode with feedthrough with and without feedthrough cancellation. As can be seen, the cancellation circuit can effectively compensate for phase and magnitude changes due to capacitive feedthrough. Using this circuit, the drive loop can efficiently lock into the series resonance mode.

3.3   SENSE FRONT-END WITH COHERENT DEMODULATION

Figure 3.7 shows the general architecture of an AM gyroscope system. A drive loop is used for self-sustaining actuation of the gyroscope. The Coriolis-induced current is sensed and amplified to a voltage by means of a TIA front-end. The TIA output voltage is then multiplied by the drive signal, using an analog multiplier, to demodulate rate.

As mentioned previously in Chapter 1, phase-sensitive demodulation helps reject quadrature error from the rate signal. However, the damping coupling appears directly in the rate output and still degrades the bias performance. At mode-matched condition for instance, in order to demodulate both rate and quadrature signals, an I/Q demodulation scheme can be used in which the in-phase component of the output represents rate and the quadrature-phase output component represents stiffness coupling, as described by
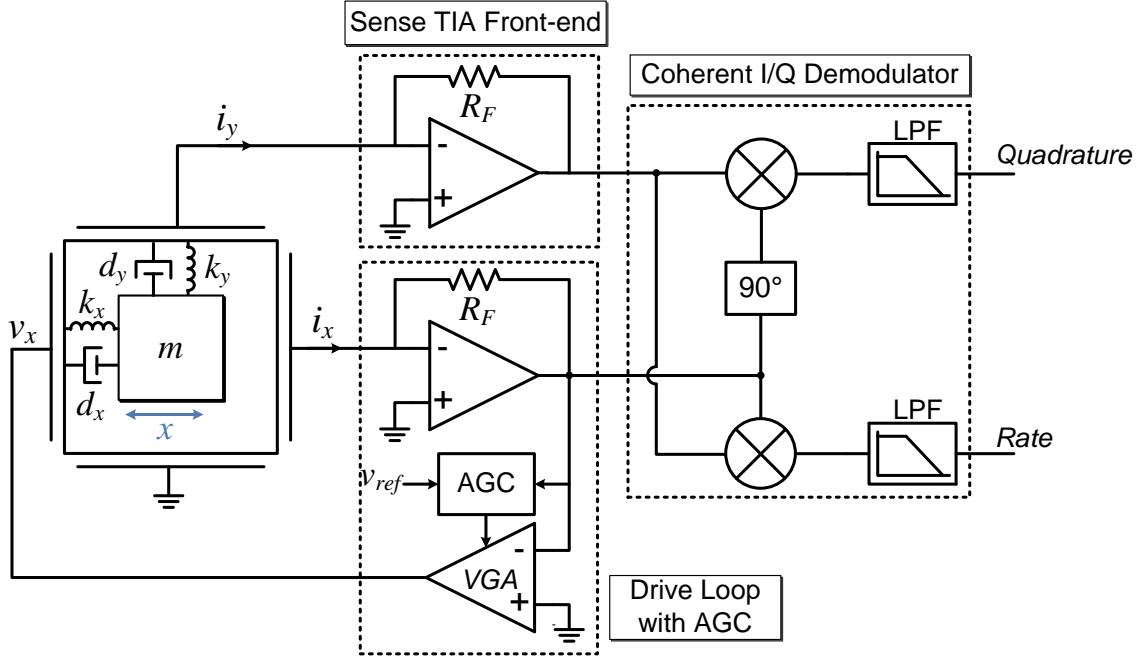
Figure 3.7: General architecture of conventional AM gyroscope system; a drive loop actuates the drive mode in a self-sustaining loop, and a TIA-based sense front-end amplifies the Coriolis-induced sense current into sense voltage to be demodulated with an I/Q coherent demodulator. The in-phase and quadrature-phase outputs of the demodulator provide information of rate and quadrature coupling, respectively.

(1.9). It is necessary to note that (1.9) describes the sense-mode displacement, which is in quadrature with the output current that is proportional to velocity.

3.3.1   Quadrature Cancellation

The quadrature data demodulated from the sense output can be used for in-run monitoring and control of the gyroscope modes alignment. A typical approach is shown in Figure 3.8, where the demodulated Q-channel output is provided to a PID controller that generates the required DC voltage for the quadrature electrodes to null the stiffness coupling at the device level, or equivalently to align the modes [8]-[9].

Mode misalignment is the main cause of initial frequency mismatch in gyroscopes after fabrication, since the quadrature terms add up to the determinant of the gyroscope system matrix and split the solutions, i.e. split the mode frequencies, as explained in section 2.4 of Chapter 2 of this thesis. Therefore, prior to implementation of any mode-
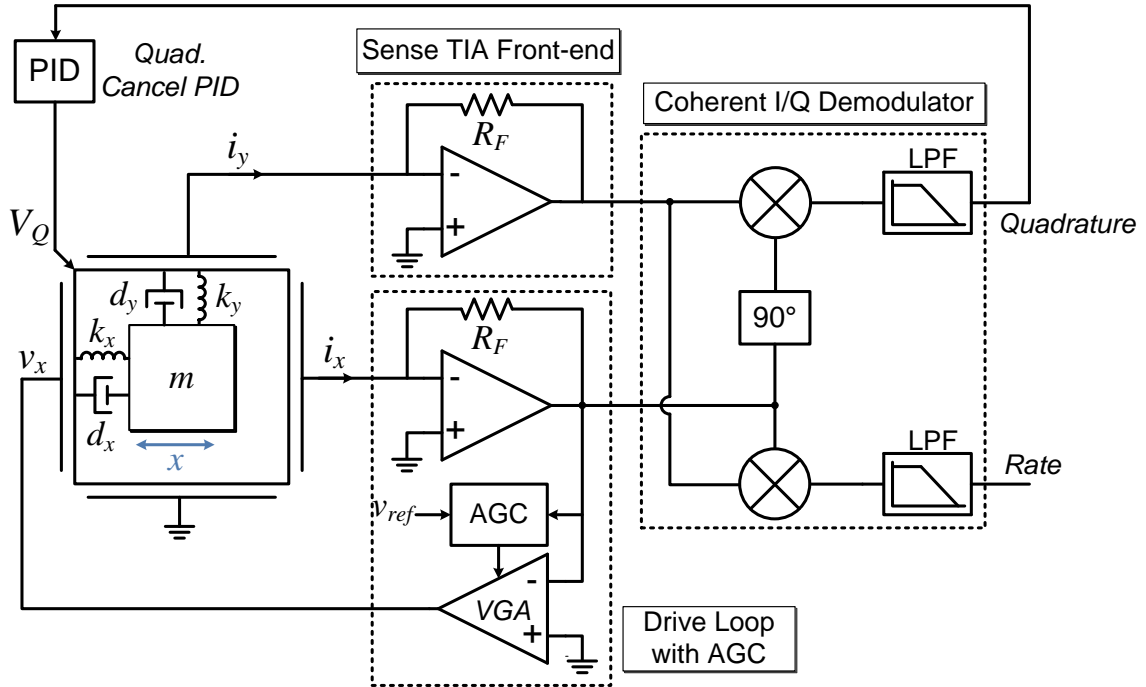
Figure 3.8: General scheme for closed-loop quadrature cancellation; a PID is used in the AM gyroscope to null the quadrature demodulator output. The output of the PID controls the electrostatic quadrature nulling electrodes of a capacitive MEMS gyroscope.

matching scheme, an initial mode alignment scheme is needed to cancel the effect of stiffness coupling terms, followed by an in-run alignment scheme to maintain alignment.

3.3.2 Force-to-Rebalance Architecture

The system architecture described thus far is based on an open-loop sensing and demodulation scheme. In such a scheme, the full scale range of the system is limited to the bandwidth of the mechanical element, i.e. the gyroscope sense-mode bandwidth, since the gyroscope modes split apart in response to rotation, as described by (2.9), resulting in nonlinearity due to rate-dependent transfer function at large input rotations. To eliminate the effect of applied rate on the transfer function of the gyroscope, a closed-loop force-to-rebalance architecture can be used as shown in Figure 3.9. In this scheme, a PID controller loop is used to null the sense-mode velocity by applying appropriate input to the gyroscope sense mode to counterbalance the mechanical Coriolis force. As a result, effectively no Coriolis force will remain in the transfer function of the gyroscope,
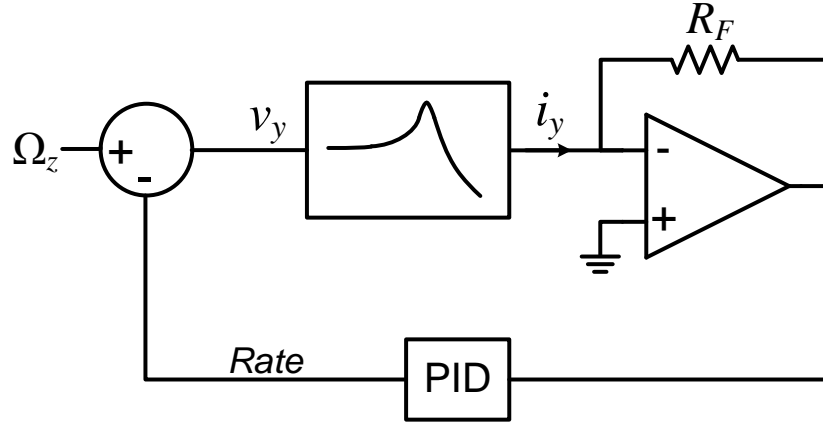
Figure 3.9: General block diagram of force-to-rebalance architecture; The TIA output is nulled by a PID controller at carrier frequency. The PID output is applied to the sense mode to counterbalance the Coriolis force that is generated mechanically by application of rotation.

implying that the gyroscope operation remains linear for a larger range of rotation rates. From a control systems intuitive viewpoint, by using the closed-loop force-to-rebalance architecture, the bandwidth of the overall sense mode is increased by A times, where A is the gain of the PID loop at carrier frequency. This increase in bandwidth translates to same factor of increase in the full-scale range of the gyroscope system. However, in practice, large loop gain can result in instabilities [43], making the design of such interface systems challenging, especially for high-Q, thus narrow-band gyroscopes.

A quadrature control loop used in conjunction with the force-to-rebalance loop [26] can guarantee minimum quadrature-induced displacement on the gyroscope sense mode, and consequently minimum drift of the transfer function of the overall system due to misalignments. However, in-run automatic mode-matching capability, and cancellation of the time-varying damping coupling are not inherently provided by neither of the open-loop or force-feedback schemes.

3.3.3 Mode Reversal

Mode reversal scheme takes advantage of the equality of mode coupling terms from each mode to the other, i.e. $k_{xy} = k_{yx}$ and $d_{xy} = d_{yx}$, to eliminate the long-term drift effects from the output bias of a gyroscope, yet maintain the scale factor and noise

50

performances. In a periodic fashion, the *x*-mode is actuated and the *y*-mode is sensed in one phase, while in the subsequent phase the *y*-mode is actuated and *x*-mode is sensed. In such a scheme, the rate outputs of each two consecutive phases are opposite in phase, while the bias terms remain equal and in-phase. Therefore, the subtraction of the two rate outputs from consecutive phases can be used to eliminate the bias components and also double the rate sensitivity.

This scheme has been reported in [21] and successfully utilized in [44] to reduce long-term bias variations. The core of the system used in each phase can be either an open-loop or a closed-loop force-to-rebalance configuration, with any desired control loops. The scheme typically suffers from added noise and reduced measurement bandwidth due to the limited mode reversal frequency. This limitation originates from the fact that depending on the defined system accuracy, a settling time of a few time constants is required for the gyroscope system to settle down to its steady state in each phase. For instance, for a 100 ppm settling accuracy, a minimum of 9.2τ settling time is needed, which translates to 29.3 msec for a 50-Hz-bandwidth gyroscope core, limiting the maximum applicable rate frequency to a maximum of 17 Hz only. This frequency has to be reduced yet by another order of magnitude to be able to double the sensitivity alongside cancelling the bias.

Besides limiting the measurement bandwidth, the chopping operation contributes to the overall noise by folding more noise from upper bands down to the baseband, just like any chopper-stabilization scheme in circuits. Furthermore, the uncorrelated noise demodulated from the drive loop phase noise by the coupling terms in each phase, will add up, and thus degrade the overall noise performance.

CHAPTER 4

ACTIVE PARAMETRIC TUNING OF MEMS RESONATORS

Parameter modification and tuning of MEMS resonators and resonant elements have been traditionally performed via passive loading. For instance, the quality factor loading method proposed in [14], benefits from the existence of a programmable passive series resistance that adds up to the overall RLC equivalent series resistance, thus modifies the value of the effective quality factor. Another example of such a passive tuning technique is the series capacitive tuning scheme used in [45] to tune the series-mode resonance frequency of a Piezoelectric-on-Silicon resonator. Though theoretically solid, such techniques are proven to be inefficient in presence of parasitic shunt capacitances of the MEMS device electrodes. Moreover, such techniques can only offer unidirectional tuning of MEMS parameters due to the inexistence of negative-value passive components. In order to remedy the above-mentioned challenges, this chapter presents a generalized active tuning method that can be used to linearly tune the electromechanical parameters of a MEMS resonant device by using electromechanical feedback [46]. The presented active tuning concept provides the basic principles needed for calibration of resonators and resonant sensors, including MEMS Coriolis gyroscopes. The scale factor calibration presented in the Chapter 5 will utilize the same concept to calibrate MEMS gyroscopes and eliminate sensitivity drift errors.

4.1 CONVENTIONAL MEMS TUNING SCHEMES

Various electromechanical and electronic schemes have been explored in the past for frequency tuning and quality factor tuning of MEMS resonators and resonant sensors. This section will explore the basics of a few of such techniques, and will present the implementation challenges with each technique, together with the limitations that each

scheme imposes on the system interface for resonators and resonant sensors, including MEMS resonant gyroscopes.

4.1.1   Electrostatic Spring Softening

The following 2nd-order differential equation describes a MEMS resonator:

$$m\frac{d^2x}{dt^2}+d\frac{dx}{dt}+kx=F\left(t\right), \qquad \omega_0=\sqrt{\frac{k}{m}} \tag{4.1}$$

In a capacitive resonator, the DC polarization voltage, V_P, typically applied to the body of the resonating mass, is used to transform the applied AC input actuation voltage, v_{ac}, into AC electrostatic actuation force, F_{elec}, as follows:

$$F_{elec}=\frac{1}{2}\left(V_P+v_{ac}\right)^2\frac{\partial C}{\partial x}, \qquad C=\frac{\varepsilon_0 A}{g_0-x} \Rightarrow \frac{\partial C}{\partial x}\approx\frac{C_0}{g_0}\left(1+\frac{2}{g_0}x\right)$$

$$\Rightarrow F_{elec}=\frac{1}{2}\left(V_P^2+2V_Pv_{ac}+v_{ac}^2\right)\times\frac{C_0}{g_0}\left(1+\frac{2}{g_0}x\right) \tag{4.2}$$

where, C is the transducer capacitance, C_0 is the transducer capacitance at rest, g_0 is the capacitive parallel-plate gap at rest, A is the area of the capacitive electrode, and x is the resonator displacement as a result of the applied force. In response of F_{elec}, the overall 2nd-order equation of the device can be rewritten as:

$$m\frac{d^2x}{dt^2}+d\frac{dx}{dt}+kx=\frac{1}{2}\left(V_P^2+2V_Pv_{ac}+v_{ac}^2\right)\times\frac{C_0}{g_0}\left(1+\frac{2}{g_0}x\right)$$

$$\approx\frac{1}{2}V_P^2\frac{C_0}{g_0}+V_Pv_{ac}\frac{C_0}{g_0}+V_P^2\underbrace{\frac{C_0}{g_0^2}x}_{k_{elec}.x} \tag{4.3}$$

which shows that the electrostatic force is mainly comprised of a DC component, an actuating AC component at the resonance frequency of the resonator that is the product of v_{ac} and the transduction coefficient, $V_P.C_0/g_0$, and lastly another AC component that is proportional to the resonator displacement. The coefficient of the latter term, $V_P^2.C_0/d^2$,

can be used together with the stiffness terms in the original resonator equation to redefine the equivalent resonator stiffness coefficient as follows:

$$m\frac{d^2x}{dt^2} + d\frac{dx}{dt} + \left(k - V_P^2\frac{C_0}{g_0^2}\right)x = \frac{1}{2}V_P^2\frac{C_0}{g_0} + V_P v_{ac}\frac{C_0}{g_0} \tag{4.4}$$

The equivalent stiffness coefficient is the combination of the mechanical stiffness, k, and the electrical stiffness $k_{elec} = V_P^2 . \varepsilon_0 A/g_0^3$. In other words, the electrostatic force, $k_{elec}.x$ generated by the electrostatic transducer can modify the equivalent stiffness of the resonator, thereby tuning its resonance frequency. However, since the electrostatic stiffness term, k_{elec}, is always positive, when subtracted from the mechanical stiffness of the resonator, it can only reduce the effective stiffness and thus reduce the resonance frequency, hence the name spring softening.

In order to tune the resonance frequencies of the degenerate modes in capacitively actuated MEMS gyroscopes, electrostatic spring softening technique is used by applying an independent DC voltage at the anti-node of the desired mode, where the maximum displacement of the mode takes place [35]. Typically, the polarization voltage, V_P, is applied to the resonating mass, and therefore the difference of the electrical stiffness terms created by the polarization voltage and the tuning voltage will tune the mode to the desired frequency as described below:

$$k_{elec} = \sum_i \frac{C_i}{g_i^2}\left(V_P^2 - V_{T,i}^2\right) \tag{4.5}$$

where $V_{T,i}$ is the DC tuning voltage applied to electrode-i, while V_P is applied to the resonating mass, thereby creating an electrostatic force component proportional to V_P^2 for all electrodes. Using this scheme, assuming that the potential of the signal electrodes is at 0V, by increasing the tuning voltage of a specific mode, the corresponding mode frequency increases.

In the same manner, electrostatic spring softening can be used to cancel stiffness coupling error between the modes of an axisymmetric gyroscope. By applying a DC potential to the quadrature electrodes located in between each two neighboring anti-nodes of the two modes, the quadrature-induced displacements will modulate the DC voltage into an AC mechanical force that can be used with appropriate magnitude and polarity to cancel the quadrature error itself. This quadrature-nulling technique [5] has been used manually in this work to cancel quadrature error to enable near-mode-matched operation.

Though being efficient in practice, electrostatic spring softening suffers from nonlinearity of its tuning curve, and incapability of providing bidirectional tuning. Moreover, the electrostatic stiffness coefficient is inversely proportional to $g_0{}^3$, which limits the tuning capability of this scheme for capacitive devices with relatively large gaps. Moreover, it cannot be directly applied to transduction mechanisms other than capacitive actuation. For instance, incorporating electrostatic tuning into Piezoelectric or Piezoelectric-on-Silicon resonators in [47]-[48] requires special additional fabrication processing steps, while still effective only for compliant, thus low-frequency, resonators. Developing an efficient frequency tuning scheme specifically for high-frequency Piezoelectric-on-Silicon resonators has been a challenging topic of research for years.

4.1.2 Electronic Capacitive Series Tuning for Piezoelectric-on-Si Resonators

Another conventional method of tuning MEMS resonators, especially aimed to tune Piezoelectric-on-Silicon resonators, is active series tuning [45], [49]. A programmable capacitor array is used in series with the RLC tank to tune the value of the motional capacitance, thereby tuning the frequency of the resonant mode. In an ideal series RLC tank, a series capacitor bank or tuning varactor, can tune the frequency as:

$$f_{tune} = f_0 \sqrt{1 + \frac{C_m}{C_{tune}}} \qquad (4.6)$$

where C_{tune} is the tuning capacitance, f_0 is the initial resonance frequency before tuning, and f_{tune} is the unidirectionally tuned resonance frequency. The nonlinearity of the tuning curve in this scheme necessitates the use of look-up-table (LUT) approaches wherever a programmable and self-sufficient implementation is desired. Moreover, in this scheme, the tuning range depends highly on the resolution of the capacitor bank, which is typically limited to a few tens of fF in most short-channel CMOS processes, which implies limited tuning range and low tuning slope, in presence of C_m values as low as a fraction of a fF, or even tens of aF depending on the resonance frequency.

In presence of shunt parasitic pad capacitance, C_p, at the device electrodes, the total capacitance seen by the resonator will be $C_p + C_{tune}$. In practice, the value of C_p can vary in a range of 1-10 pF, which makes C_p dominate the total capacitance seen by the resonator, thus makes the tuning scheme inefficient. In order to alleviate this issue, an enhanced series tuning scheme is used in [45], where an active negative capacitor circuit cancels the effect of C_p over a certain range of frequencies to make the series capacitive tuning scheme efficient at frequencies as high as ~500 MHz. Similarly, the active inductor circuit used in [49] cancels the effect of C_p to provide efficient tuning. Figure 4.1 shows a conceptual block diagram implementation of the enhanced series tuning
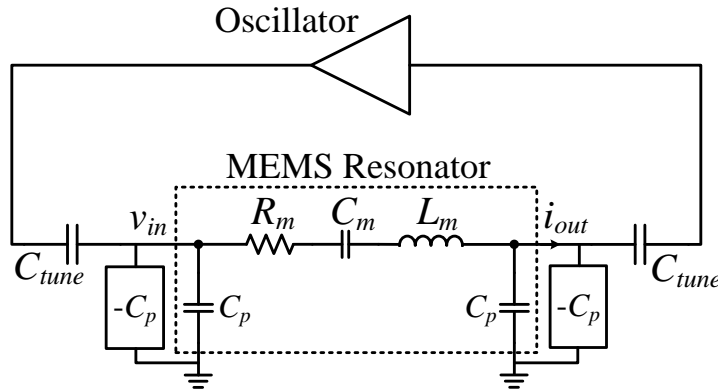
Figure 4.1: Enhanced series tuning scheme; two tuning capacitors are used to tune the motional capacitance of the resonator. In order to cancel the effect of parasitic pad capacitance, two negative capacitor circuits are used at the pads of the resonator.

56

scheme. However, even with cancellation of the shunt pad capacitance, the scheme has to use equalization circuits that translate the linear temperature sensor characteristic to square-root function for temperature compensation. The accuracy of this equalization, and its stability across temperature, can create additional errors in the temperature stability of the tuned oscillator.

Although the enhanced series tuning scheme is useful for resonator tuning, the passive phase-insensitive nature of this scheme disqualifies it for gyroscope tuning.

4.1.3 Electromechanical Passive Load Tuning of MEMS Resonators

Another method of tuning for Piezoelectric-on-Si MEMS resonators is passive load tuning, as described in [50]. In this type of scheme, a resistive load on the device terminal is adjusted to tune the imaginary component of the shunt loading, thereby tune the resonance frequency of the series RLC tank. The equivalent shunt impedance of the device pad in presence of parasitic pad capacitance C_p, can be written as:

$$Z_{eq} = \frac{R_L}{1 + j\omega R_L C_p} \approx \frac{R_L}{1 + \omega^2 R_L^2 C_p^2} - j\frac{\omega R_L C_p}{1 + \omega^2 R_L^2 C_p^2} \tag{4.7}$$

which shows that the imaginary component of the load impedance can be used for unidirectional tuning of the series RLC tank, by changing the value of the load resistance, R_L. The tuning curve profile depends on the values of the original resonance frequency, R_L, and C_p. As long as the value of $\omega R_L C_p \ll 1$, the tuning curve can remain linear. Another important implication of (4.7) is the effect of the real part of the load impedance on the quality factor of the resonator. The real part of this impedance can be used to tune the quality factor of the resonator, where the desired amount of Q-loading and the values of frequency and C_p, can affect the effectiveness of the quality factor tuning.

The efficiency of this tuning scheme degrades with increase of the silicon thickness in the resonator stack. Moreover, similar to the electronic capacitive series

tuning scheme, this technique is also inappropriate for gyroscope mode tuning, mainly due to its Q-loading effect, and also due to challenges with programmability of tuning.

4.2 DYNAMIC TUNING OF MEMS RESONATORS VIA ELECTROMECHANICAL FEEDBACK

The main objective of the techniques explored in the previous section was to provide solely frequency tuning mechanisms for MEMS resonators and resonant elements. The rest of this chapter presents a methodology for electromechanical parameter tuning of MEMS resonant elements, including its stiffness, mass, damping, or even mode coupling in a coupled resonator, particularly in a gyroscope. Beyond the frequency tuning problem only, the techniques provide the basic principles for self-calibration of timing resonators and resonant sensors.

4.2.1 Active Displacement/Acceleration Feedback for Frequency Tuning

The resonance frequency ω_0, of the resonator described in (4.1) can be modified by physically changing the values of either the mass m, or the spring constant k, of the resonator. Alternatively, in a similar manner to electrostatic spring softening, and as described in the modeling of section 2.3, ω_0 can also be modified by mathematical addition or subtraction of additional force terms to the input of the resonator model that are either proportional to the resonator displacement, x, or proportional to the resonator acceleration, d^2x/dt^2, thereby modifying the effective values of k or m, respectively, as:

$$m\frac{d^2x}{dt^2} + d\frac{dx}{dt} + kx = F(t) \pm k_T x \mp m_T \frac{d^2x}{dt^2}$$

$$\Rightarrow (m \pm m_T)\frac{d^2x}{dt^2} + d\frac{dx}{dt} + (k \mp k_T)x = F(t), \quad \omega_0 = \sqrt{\frac{k \mp k_T}{m \pm m_T}}, \qquad (4.8)$$

where k_T and m_T are the coefficients of the displacement and acceleration force terms, respectively. Figure 4.2a shows the electrical model of a two-port resonator, in which the

$$v_{tune,1} = \frac{1}{C_T} \int i_L(t)\, dt = \frac{q}{C_T} \triangleq k_T x$$

$$v_{tune,2} = L_T \frac{di_L(t)}{dt} = L_T \ddot{q} \triangleq m_T \ddot{x}$$

(a)

$$v_{tune,1} = \frac{1}{C_T} \int i_{sns}(t)\, dt$$

$$v_{tune,2} = L_T \frac{di_{sns}(t)}{dt}$$

(b)
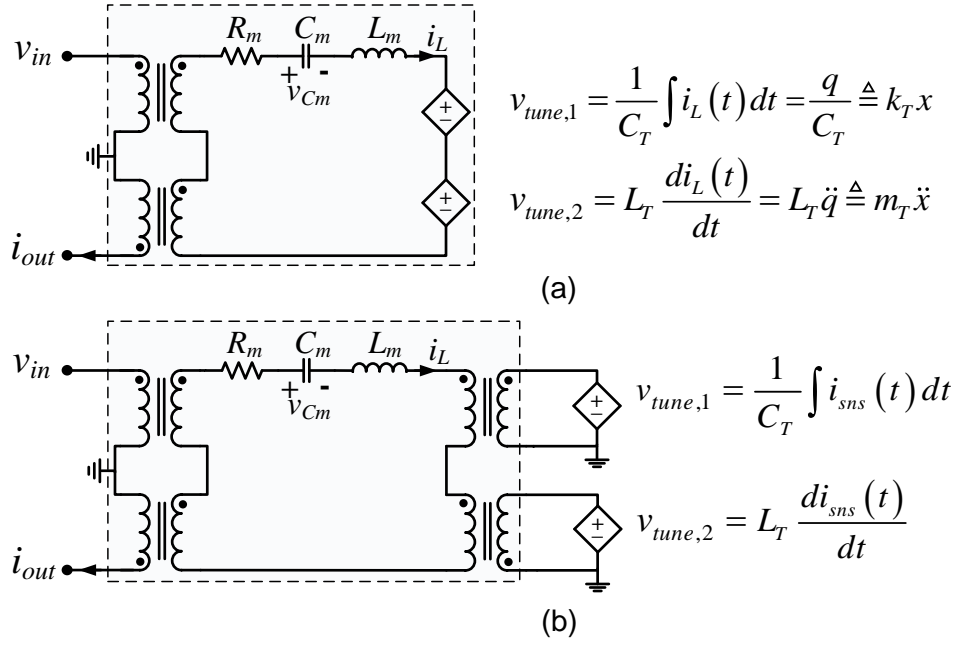
Figure 4.2: (a) Electrical model of a two-port resonator; additional tuning forces are modeled by series VCVS, (b) In a 4-port resonator, the additional external tuning forces are generated by integration and differentiation of resonator output current, and are fed back to the additional resonator signal ports.

additional tuning forces are modeled by series VCVS sources. In the electrical domain, m, k, and d are modeled by L_m, $1/C_m$, and R_m, respectively. The motional capacitor charge, $q = C_m \times v_{C_m}$, and the motional inductor current, i_L, are used to equivalently model the displacement and velocity of the resonance mode, respectively.

As shown in Figure 4.2b, the tuning voltage signals can be generated in the electrical domain by integration or differentiation of the resonator output current, i_{out}. The generated signals are then scaled by k_T and m_T gain coefficients, to be applied externally to the resonator ports, where they are translated back to their corresponding mechanical forces in the resonator. As discussed in section 2.1, the tuning forces applied to resonator ports add up in series with the resonating components to tune their resonance frequency.

Even though both mass and stiffness can be electrically tuned by the proposed method, in this work the system implementation and related simulations and analyses are

mainly focused on electrical tuning of stiffness, where the resonator output current is integrated to generate the tuning force.

A significant advantage of the proposed tuning scheme is its insensitivity to parasitic pad capacitances, since the frequency tuning is provided by means of tuning forces that are generated by active circuits that can be designed to drive the passive loads.

Applicability to MEMS Resonant Gyroscopes:

Another significant advantage of the active tuning scheme is its applicability to mode-matched gyroscopes, since it can directly target the stiffness of each resonance mode without loading any other parameters of the mode, unlike in the case of passive tuning. The applicability of this scheme to mode-matched AlN-on-Si resonant gyroscopes has been shown in [51], where the gyroscope mode frequencies were matched by the active tuning technique, to maximize the device sensitivity. Unlike in capacitively tuned gyroscopes, where the mode with lower frequency has to be tuned to match the higher frequency mode, in active tuning, either of the two modes can be linearly tuned to match the other, thanks to the bidirectional tuning capability provided by active tuning technique. This provides more flexibility to the automatic mode-matching circuits in the gyroscope interface.

Another enabling feature of the proposed active tuning scheme is its capability to mimic and different forces in resonant sensors, including the undesired mode coupling terms in resonant gyroscopes, i.e. quadrature coupling, damping coupling, and Coriolis coupling terms. For instance, the active tuning technique can be customized to cancel the effect of mode coupling terms in a piezoelectric-on-Silicon gyroscope. While this has not been practiced in this dissertation, the mimicking of Coriolis force using the active electromechanical tuning technique is used in Chapter 5 to electrically induce a virtual rotation to the gyroscope, and to use the gyroscope response to this virtual rotation for self-calibration of the physical scale factor. The active tuning technique provides a paradigm shift in the design methodology and control of MEMS resonant elements.
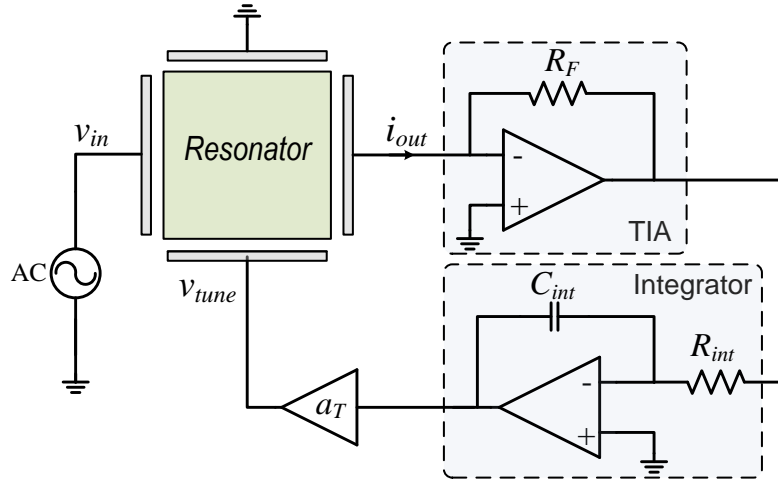
Figure 4.3: A tuning feedback loop is used to tune the open-loop resonator frequency response. The displacement signal is generated by integrating the TIA output, thereby generating a displacement signal. The displacement signal is then scaled by a variable gain, a_T, to provide tuning to the resonator frequency.

4.2.2 System Implementation and Performance Analysis

Figure 4.3 shows the schematic of a test setup in which a feedback loop is implemented to tune the frequency of a multi-port resonator. In this setup, the excitation is provided by a signal generator to the resonator input, v_{in}. The output current of the MEMS resonator, i_{out}, is detected and amplified to a voltage by means of a TIA, and is integrated by a voltage integrator to generate a scaled displacement signal. The resulting signal is then multiplied by a gain of a_T, and is fed back to the resonator through an additional signal port, for active tuning. In electrical domain, the equivalent partial differential equation of the resonator can be written as:

$$L_m \frac{d^2 q(t)}{dt^2} + R_m \frac{dq(t)}{dt} + \frac{q(t)}{C_m} = v_{in}(t) + v_{tune}(t),$$

$$v_{tune}(t) = \frac{a_T R_F}{R_{int} C_{int}} q(t). \qquad (4.9)$$

Therefore, the overall resonator equation is rewritten as:
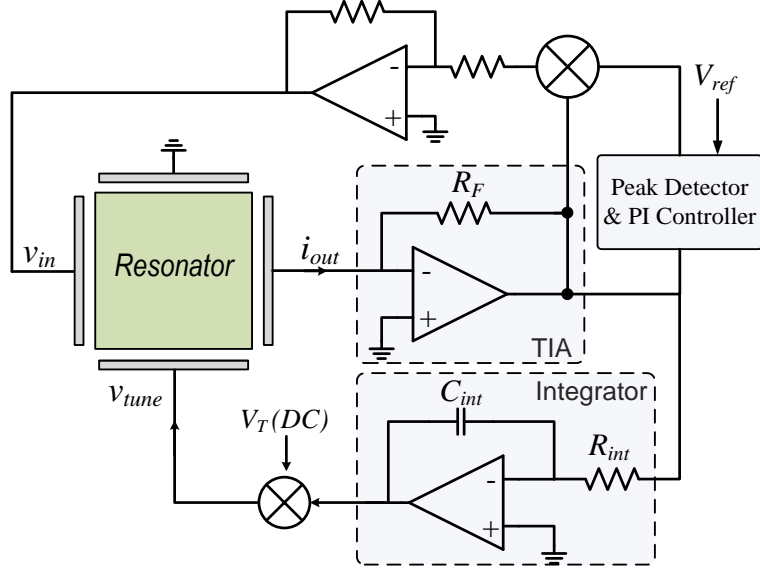
Figure 4.4: An oscillator loop is closed around the resonator, while the tuning signal is applied to another port to tune the oscillation frequency. In the practical implementation, the displacement signal is scaled by an analog multiplier.

$$L_m \frac{d^2 q(t)}{dt^2} + R_m \frac{dq(t)}{dt} + \left[\frac{1}{C_m} - \frac{a_T R_F}{R_{int} C_{int}} \right] q(t) = v_{in}(t). \tag{4.10}$$

Consequently, the tuned resonator frequency, f_{tune}, can be derived as follows:

$$\frac{f_{tune}}{f_0} = \sqrt{1 - \frac{a_T R_F C_m}{R_{int} C_{int}}} \simeq 1 - \frac{a_T R_F C_m}{2 R_{int} C_{int}}, \tag{4.11}$$

The approximation in (4.11) is valid if $C_m \ll C_{int}$. Therefore, the proposed setup can provide linear tuning for MEMS resonators. Moreover, larger value of C_m results in larger tuning slope. Another means of increasing the tuning slope and tuning range is to use multiple tuning electrodes/ports to increase the number of series v_{tune} voltages, thereby increasing the overall tuning force applied to the resonator.

A closed-loop oscillator for the proposed tuning technique is shown in Figure 4.4. The oscillator circuit includes an automatic gain control (AGC) block that monitors the TIA output voltage and stabilizes the resonator velocity by means of a PI controller. The TIA output is integrated and then scaled by an analog multiplier to generate the tuning

62

signal. Using this multiplier, the DC voltage V_T operates similar to the variable gain a_T in the tuning loop of Figure 4.3.

The displacement signal required for active tuning can alternatively be generated by means of a transcapacitance amplifier, followed by a voltage gain-stage. However, the schematics of Figure 4.3 and Figure 4.4 are meant to describe the generalized reconfigurable implementation of the tuning system, where the integrator can be replaced by a differentiator to virtually modify the mass coefficient, as explained by (4.8).

Another practical way to provide the tuning signal is to generate a 90° phase-shifted signal from the TIA output, e.g. by using a phase-locked loop (PLL) circuit or an analog all-pass phase shifter circuit. While the phase-shifted signal has the right phase, it may not have the exact same amplitude as the tuning signal that would have been generated by a differentiator or an integrator. This discrepancy can result in slight tuning inaccuracies. For instance, for a maximum tuning range of 1000 ppm, the maximum difference between the constant amplitude of a constant-envelope phase-shifted signal and that of a differentiator with gain of ωRC, is 1000 ppm over the entire tuning range. Based on (4.11), an error of 1000 ppm in the tuning coefficient a_T, results in $<1\,\text{ppm}$ error in the overall tuning range.

<u>Tuning Range Limitation:</u>

The maximum linear tuning range for a given resonator is determined by the maximum swing of the tuning signal, which is limited by the available linear voltage headroom at the output of each amplifier in the tuning loop.

The output current of the resonator, v_{in}/R_m, is integrated and amplified to generate the tuning signal. Therefore, with the signal headroom limited to the supply voltage, V_{Supply}, the maximum tuning gain, $a_{T,max}$, can be derived from:

$$\frac{v_{drv}}{R_m} \times \frac{a_T R_F}{R_{int} C_{int} \omega_0} < V_{Supply}, \tag{4.12}$$

resulting in:

$$a_{T,max} = \frac{V_{Supply}}{v_{drv}} \times \frac{R_m R_{int} C_{int} \omega_0}{R_F}. \tag{4.13}$$

Using (4.11) and (4.13), the maximum linear tuning range is:

$$\frac{\Delta f_{max}}{f_0} = \frac{V_{Supply}}{v_{drv}} \times \frac{R_m C_m \omega_0}{2} = \frac{V_{Supply}}{2Q v_{drv}}. \tag{4.14}$$

As can be seen, the maximum linear tuning range is inversely proportional to the values of Q and drive amplitude.

Simulation results:

The functionality and performance of electrical active tuning technique is verified with Cadence simulations using the circuit model of a 4-port AlN-on-Si resonator that will be described in section 4.3.1, with $Q = 4500$, $R_m = 1$ kΩ, and $f_0 = 14.2$ MHz. The 4-port resonator has four identical signal electrodes; two for open-loop characterization and closed-loop oscillator interface, and two additional ones available for active tuning.

Figure 4.5 shows the results of applying the tuning displacement signal to only one of the additional tuning electrodes, while the other tuning electrode is grounded. As
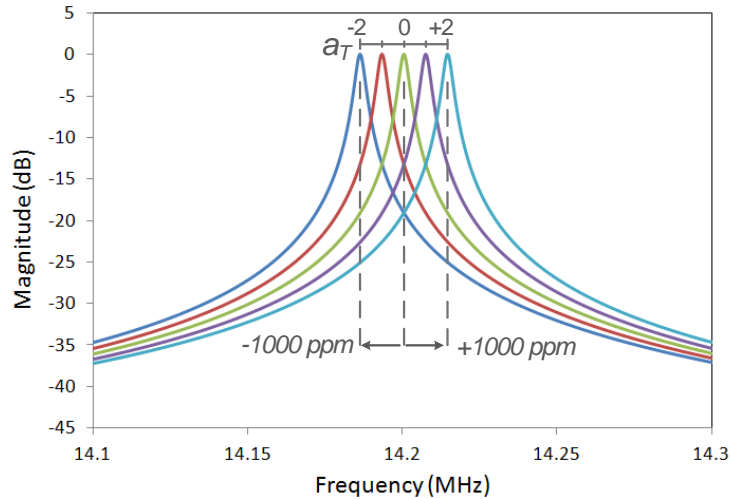
Figure 4.5: Tuning signal is applied to only one electrode. By changing a_T in a range of [-2, 2], the resonator frequency is linearly tuned by ±1000 ppm.

64

can be seen, the frequency response of the 14.2-MHz resonator is tuned by almost ±1000 ppm, by changing the gain of the tuning loop, a_T, in a range of [-2, 2] shown on the horizontal ruler on the top of Figure 4.5. This is in close agreement with (4.11), given a TIA gain of $R_F = 1$ kΩ, $C_m = 2.4905$ fF, $L_m = 50.44$ mH, $R_{int} = 1$ kΩ, and $C_{int} = 2.5$ pF.

Figure 4.6 shows a comparison of dual-port tuning and single-port tuning. The solid line corresponds to the original resonator peak with no tuning, while the dashed line and dotted lines correspond to single-port and dual-port tuning, respectively, both with $a_T = 2$. As expected, dual-port active tuning provides 2000 ppm of tuning which is twice larger than in single-port active tuning.

In order to further confirm the applicability of active tuning to MEMS-based closed-loop oscillators, the 4-port MEMS resonator model is used to provide sinusoidal oscillations at around 14.2 MHz, using the series-mode oscillator circuit shown in Figure 4.4. Periodic Steady State (PSS) simulations were run in Cadence to find the precise oscillation frequency at different values of the tuning voltage, V_T. The oscillator is designed to provide peak v_{drv} amplitude of 500 mV, while the tuning circuits operate from ±5V supply voltages.
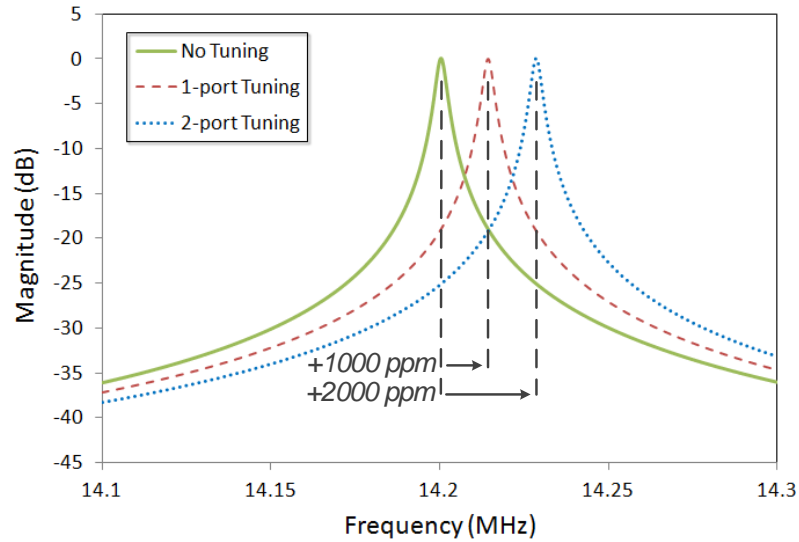
Figure 4.6: The tuning signal is applied to two electrodes for dual-port active tuning, doubling the tuning to 2000 ppm at $a_T = 2$.

As described by (4.12), the amplitude of the tuning signal is restricted by the supply voltage levels. Consequently, the maximum tuning range is determined by the resonator quality factor and the peak amplitude of v_{drv}, as derived in (4.14).

In order to verify the effect of resonator quality factor on tuning performance, two different Q values of 4500 and 3000 are used for the resonator and the oscillation frequency is plotted versus the tuning voltage, V_T, as shown in Figure 4.7. To make a fair comparison, the value of R_m remains the same in both cases, i.e. in the resonator with $Q = 3000$, the values of C_m and L_m change to 3.7365 fF and 33.62 mH, respectively.

For the resonator with $Q = 4500$, linear tuning slope of 500 ppm/V, and maximum linear tuning range of ±1100 ppm (±15.6 kHz) are achieved in the linear tuning range, which is in agreement with (4.11). For the resonator with $Q = 3000$, tuning slope of 750 ppm/V and maximum linear tuning range of ±1650 ppm (±23.4 kHz) are obtained, both 1.5 times larger than in the previous case, as expected from (4.11) and (4.14). It must be noted that in these simulations, maximum linear tuning range is reported, as the main
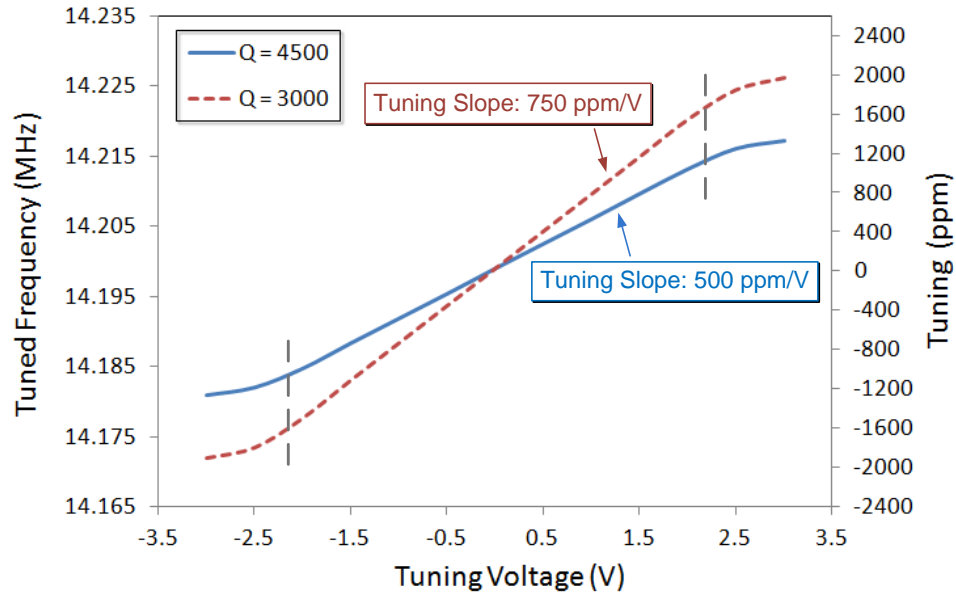
Figure 4.7: The oscillation frequency is simulated for two different resonator Q values of 4500 and 3000. The linear tuning range is inversely proportional to Q, as expected from (4.14); the tuning curve saturates at levels described by (4.12).

66
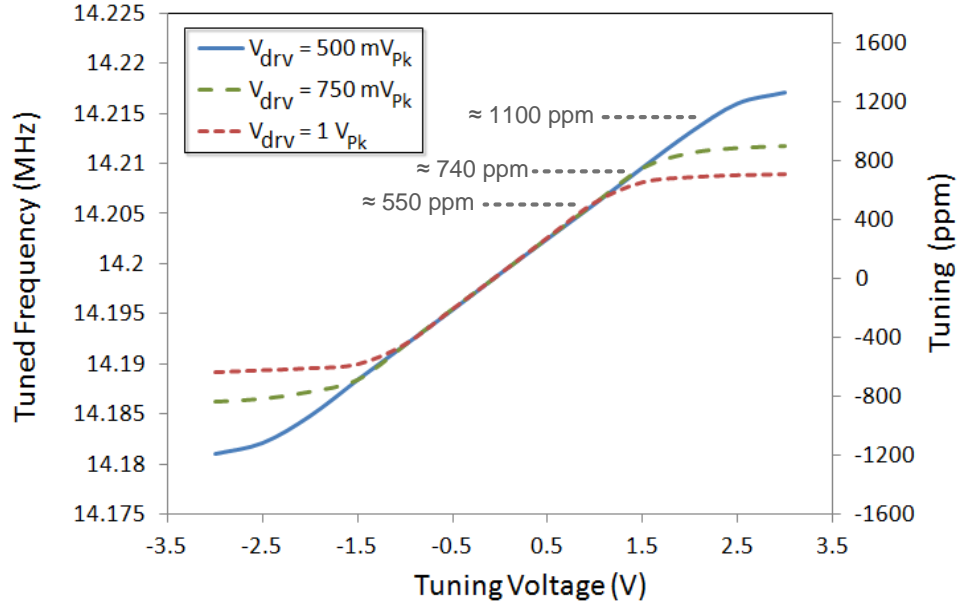
Figure 4.8: For three different values of the drive input signal, the tuning slope remains the same, while the linear tuning range changes as described by (4.14).

purpose of active tuning is to provide programmable linear tuning to the resonator.

Figure 4.8 shows the effect of v_{drv} amplitude on the tuning performance of the closed-loop oscillator. As can be seen, the linear-range tuning slope remains the same for all three different values of v_{drv} peak amplitude. However, as expected from (8), the tuning range becomes smaller as v_{drv} amplitude increases. Maximum linear tuning ranges of ± 1100 ppm, ± 740 ppm, and ± 550 ppm are obtained for v_{drv} peak amplitude levels of 500 mV, 750 mV, and 1V, respectively. The simulation results of Figure 4.7 and Figure 4.8 can be used to highlight the tradeoff between increasing the linear tuning range and reducing oscillator phase noise while using active tuning.

4.2.3 Tuning of Single-Port Resonators

So far, the active tuning scheme has been presented and used only for multi-port resonators, with at least 3 ports, two of which are used as input and output for closed-loop series-mode oscillator implementation, and any additional electrode could be used for active frequency tuning. For devices with limitations on the number of ports, e.g.

67
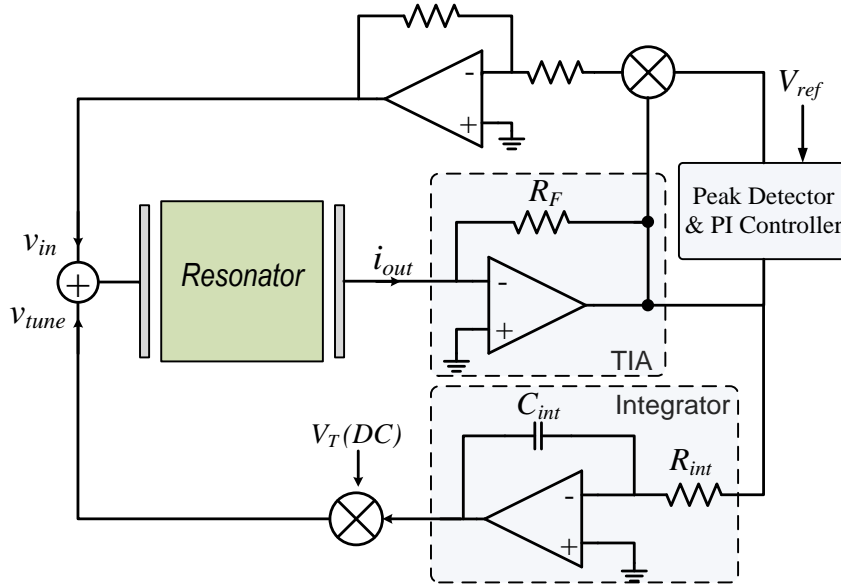
Figure 4.9: Single-port active tuning; a summing amplifier is used to add the in-phase actuation force and the quadrature-phase (displacement feedback) tuning force to provide frequency tuning.

traditional beam resonators with two ports only, the proposed active tuning technique can still be applied for frequency tuning, by using an analog summing amplifier, that adds up the input drive voltage, v_{in}, and the feedback tuning signal, v_{tune}.

Figure 4.9 shows the implementation of such a scheme on a 2-port resonator where, the summation performed mechanically by the device additional ports, in Figure 4.4, is now performed in electrical domain by the analog summing amplifier.

4.2.4 Effect of Tuning Loop Phase Shift on Tuning Performance

Since active tuning electrically modifies the mechanical parameters of the resonator, any amplitude or phase error in the tuning signal can modify the overall resonator characteristic and can affect the tuning performance. It can be shown that as long as the tuning signal maintains accurate quadrature phase relationship with i_{out}, the amplitude errors in the tuning circuits only affect the tuned resonance frequency of the resonator. However, delay-induced phase errors caused by bandwidth limitation and finite DC gain of the opamps in the tuning loop affect the resonator insertion loss and quality factor as well as its tuning performance.

In the presence of a timing error Δt in the tuning signal, (4.9) can be rewritten as:

$$L_m \frac{d^2 q(t)}{dt^2} + R_m \frac{dq(t)}{dt} + \frac{q(t)}{C_m} = v_{drv}(t) + \frac{a_T R_F}{R_{int} C_{int}} q(t \pm \Delta t).$$ (4.15)

The timing error, Δt, is translated to a phase error, $\Delta \varphi = \omega \times \Delta t$, in the phasor representation of a sinusoidal oscillation at frequency ω. With this phase error, the tuning charge/displacement signal can be decomposed into an in-phase component and a quadrature-phase component with respect to the resonator current/velocity term, dq/dt. While the quadrature-phase component tunes the resonance frequency of the resonator, the in-phase component of the tuning signal can amplify or attenuate the magnitude of the output current, i.e. the velocity coefficient, depending on the polarity of $\Delta \varphi$. Therefore, the phasor transform of the resonator equation described in (4.15) can be rewritten as:

$$\left[-L_m \omega^2 + \left(R_m \mp \frac{a_T R_F \sin \Delta \varphi}{R_{int} C_{int} \omega} \right) j\omega + \left(\frac{1}{C_m} - \frac{a_T R_F \cos \Delta \varphi}{R_{int} C_{int}} \right) \right] Q(j\omega) = V_{drv}.$$ (4.16)

The above equation results in a tuning slope of:

$$\frac{f_{tune}}{f_0} \simeq 1 - \frac{a_T R_F C_m \cos \Delta \varphi}{2 R_{int} C_{int}},$$ (4.17)

and a modified motional resistance of:

$$R_m' = R_m \mp \frac{a_T R_F \sin \Delta \varphi}{R_{int} C_{int} \omega}.$$ (4.18)

The modified quality factor, Q', of the resonator is:

$$Q' = Q \times \frac{\sqrt{1 - \frac{a_T R_F C_m \cos \Delta \varphi}{R_{int} C_{int}}}}{1 \mp \frac{a_T R_F \sin \Delta \varphi}{R_m R_{int} C_{int} \omega}} \approx \frac{Q}{1 \mp \frac{a_T R_F \sin \Delta \varphi}{R_m R_{int} C_{int} \omega}}.$$ (4.19)

It can be shown that the quality factor is more dominantly affected by the change of the motional resistance, than that of the motional capacitance, hence the approximation in (4.19).

By replacing a_T in (4.19) with $a_{T,max}$ described by (4.13), and regarding the results derived in (4.14), the maximum variations of the quality factor in presence of phase error $\Delta\varphi$ is derived as:

$$\frac{\Delta Q_{\text{max}\pm}}{Q} \approx \frac{\mp Q \times \Delta f_{\text{max}} \sin \Delta\varphi}{f_0 \mp Q \times \Delta f_{\text{max}} \sin \Delta\varphi}, \tag{4.20}$$

where $\Delta Q_{max\pm}$ represents the maximum Q variations at the positive and negative limits of the overall tuning range. The bidirectional variations in the insertion loss and quality factor of the tuned resonator affect the phase noise of the oscillator as predicted by Leeson's formula [52].

It can be shown that in order to maintain $\Delta Q_{max\pm}/Q$ to below a certain error level, $err_{\Delta Q,max}$, the maximum allowable value of the phase error, $\Delta\varphi_{err,max}$, must be kept within the levels described by:

$$\sin\left(\Delta\varphi_{err,\text{max}}\right) < \frac{f_0 \times err_{\Delta Q,\text{max}}}{Q \times \Delta f_{\text{max}}} = \frac{BW}{\Delta f_{\text{max}}} err_{\Delta Q,\text{max}}, \tag{4.21}$$

where BW stands for the 3-dB bandwidth (in Hz) of the resonator without tuning. In other words, the required relative quality factor error, $err_{\Delta Q,max}$ is relaxed by the ratio of the maximum tuning range Δf_{max}, and the resonator bandwidth, to obtain the required maximum phase error, $\Delta\varphi_{err,max}$. As an example, for a resonator with $Q = 5000$, i.e. $BW = 200$ ppm, and an overall tuning range of 1000 ppm, $err_{\Delta Q,max}$ of 5% translates to $\Delta\varphi_{err,max} < 0.01$ rad $\approx 0.573°$ in the tuning circuits.

The above error analysis highlights a power-accuracy tradeoff in the design of both the oscillator and the tuning circuits. To maintain the phase noise performance, and

for accurate frequency tuning of the resonator without affecting its quality factor or insertion loss, precise control of the phase and amplitude of the tuning signal is needed, which requires careful circuit design and proper bandwidth allocation at the cost of larger power consumption.

Simulation Results:

To study the effect of circuit nonidealities on the tuning performance and the resonator frequency response, a phase error $\Delta\varphi$ is added to the tuning signal by means of a delay, and the frequency response is simulated for different values of a_T. Figure 4.10 shows qualitatively the effect of the tuning phase error on the insertion loss and quality factor of the open-loop resonator. The value of $\Delta\varphi$ is changed from $0°$ to $3°$, in $1°$ steps, for different tuning gain values of $a_T=0,\pm2$. As can be seen in Figure 4.10 and as expected from the analyses of this section, at $\Delta\varphi=0°$ only the resonance frequency changes with a_T. However, with non-zero phase error, the insertion loss and quality factor of the resonator improve or degrade in the same direction depending on the polarity of $a_T\sin\Delta\varphi$, as shown in Figure 4.10. Moreover, for reasonably small values of $\Delta\varphi$, the
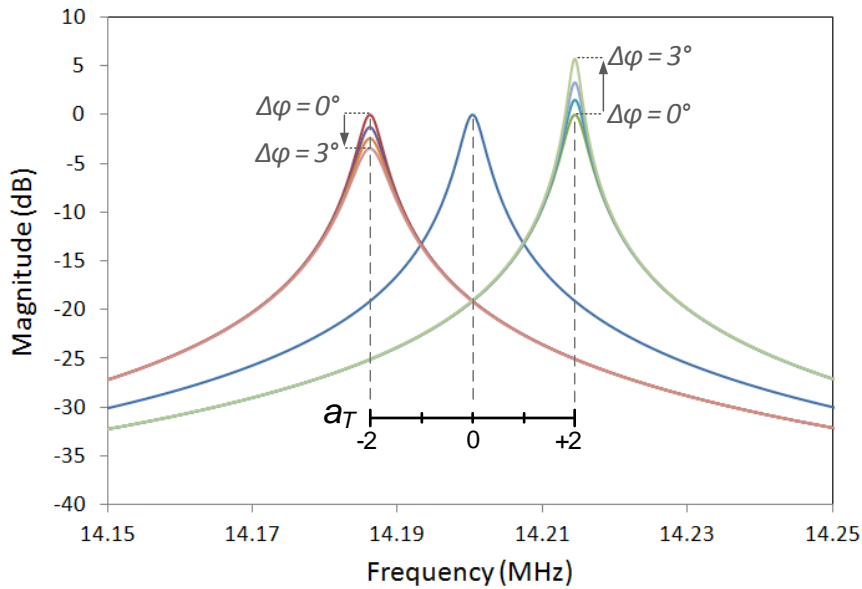
Figure 4.10: The resonator equivalent quality factor and insertion loss change as a result of phase error, $\Delta\varphi$, in the tuning signal, at different values of a_T.

71
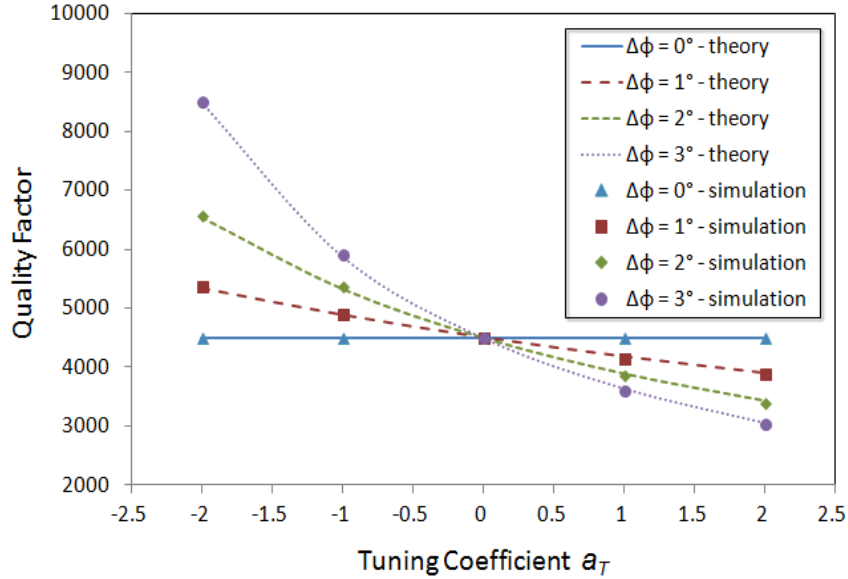
Figure 4.11: The variations of Q become more nonlinear with variations of a_T, as $\Delta\varphi$ increases. The direction of variations will change accordingly for negative values of $\Delta\varphi$.

effect of the phase error on the tuning slope and tuning range is negligible, as the value of $\cos\Delta\varphi$ remains close to unity.

Figure 4.11 shows quantitatively the effect of tuning phase error on the resonator quality factor, where the tuning coefficient is swept in a range of [-2, 2], for each value of phase error. In this figure, the lines represent the theoretical calculation results based on (4.19), while markers represent the simulation, showing close agreement with theoretical analysis. As can be seen, with larger $\Delta\varphi$ values, the relationship between the quality factor of the tuned resonator and the tuning coefficient a_T, becomes more nonlinear.

It can be shown that by reversing the polarity of $\Delta\varphi$, the trend of variations in the plots of Figure 4.10 and Figure 4.11 also reverse, implying that the quality factor is modified in a bidirectional fashion. In other words, by adding velocity feedback to the tuning signal, the damping parameter of the resonator can also be tuned in both directions, hence the name active dynamic tuning. Such capability facilitates compensation of temperature-induced quality factor inconsistencies that can be detrimental to the stability performance of frequency references and resonant sensors.

72

4.3   SYSTEM IMPLEMENTATION AND MEASUREMENT RESULTS

A multi-port AlN-on-Si resonator is used to show the effectiveness of the active frequency tuning technique presented in this Chapter. Discrete electronics are used on a printed circuit board (PCB) prototype to provide active scaled displacement feedback for frequency tuning. The following subsections will provide a brief overview of the design and concept of thin-film Piezoelectric-on-Si (TPoS) resonators, and the details of the discrete PCB design and measurement results.

4.3.1   AlN-on-Si Piezoelectric Resonator

A TPoS resonator comprises a thin-film piezoelectric layer sandwiched between two metallic electrodes stacked on top of a relatively thick substrate layer. The substrate layer, which typically comprises a large portion of the resonator structure, is chosen from materials with inherently low acoustic loss such as single-crystal silicon [53]. The metal electrodes are patterned to match the strain field of the desired resonant mode shape. By applying an AC actuation signal to an input electrode, an AC electric field is induced across the piezoelectric film, which results in a lateral stress to be induced in the structure due to the nonzero d_{31} coefficient of the piezoelectric film [53]. This stress field excites the lateral extensional resonance modes of the structure. Using the same transduction principle, the resonator vibrations are converted back to an electrical signal on an output electrode [54]. For an ideal resonator with only the desired mode shape and no parasitic modes, the functionality of all electrodes are theoretically the same. However, in presence of parasitic modes, it is sometimes beneficial to optimize the position and shape of the input and output electrodes to avoid excitation of undesired modes. With careful design of the electrodes, the coupling factor is optimized and the motional impedance of the resonator is minimized. Such resonators typically use bottom electrodes that create a ground potential to generate the electrical field in the sandwiched piezoelectric layer. The bottom metal electrode, typically made of Molybdenum (Mo), can optionally cover the

entire resonator structure, or alternatively be patterned to match the shape of their respective top electrode [53].

Thin-film piezoelectric resonators offer several advantages over capacitive resonators such as ease of fabrication, not requiring a DC polarization voltage, and not requiring vacuum [53]-[55]. Moreover, the piezoelectric layer provides a relatively large transduction coefficient, which results in larger displacement amplitudes, thus lower motional resistance, as compared to capacitive transduction used for the same resonator mode shapes. The larger range of displacements also implies a wider linear range for piezoelectrically actuated devices. The relatively larger resonator displacement amplitude offered by this transduction mechanism, can be taken advantage of for reducing mechanical noise in Coriolis gyroscopes, as described earlier by (1.12) and (1.13), in Chapter 1 of this thesis. However, the main barrier against using piezoelectric transduction in MEMS gyroscopes has been the lack of an efficient tuning scheme for compensation of process-induced mode split and misalignments in such devices. This especially limits the applicability of piezoelectric transduction for mode-matched resonant gyroscopes [56], where any small frequency split between the high-Q drive and sense resonance modes degrades the gyroscope performance considerably [6]. Furthermore, as explained earlier in section 4.1, piezoelectric devices also traditionally suffered from the lack of efficient tuning schemes that can compensate the process and temperature-induced variations of the resonance frequency, in a linear programmable fashion, without being affected by parasitic shunt pad capacitances.

Since the active tuning scheme is more effective with multi-port devices, a 4-port BAW square resonator is used for proof of concept. The resonator is implemented using a four-mask TPoS fabrication process, similar to the one described in [57]. A resonance mode with two-fold in-plane symmetry has been used to facilitate differential sensing of the output signal as well as electromechanical feedback for active frequency tuning.

Figure 4.12a shows the SEM picture of the device, highlighting the electrode configuration for excitation of the desired mode. The stress field pattern of the mode shape is shown in Figure 4.12b. Figure 4.12c shows the frequency response of the resonator mode at 14.18 MHz with a quality factor of ~4500. A gain of 13.9 dB at resonance at the output of the differential TIA with a gain of 4.7 kΩ, corresponds to a motional resistance of $R_m = 950$ Ω.

The resonator is comprised of a thin layer (<1 μm) of AlN sandwiched between two Mo electrode layers, and stacked upon a 300μm×300μm×20μm square plate of single-crystalline silicon. The square resonator is anchored to the substrate through thin compliant beams, resulting in the least perturbation in the vibration mode shape. The bottom Mo layer is used as the ground terminal and the top Mo layer is patterned to define four triangular-shaped electrodes to efficiently excite and differentially sense the lateral bulk acoustic wave mode of the square resonator, and also provide an additional signal port for active electromechanical tuning.
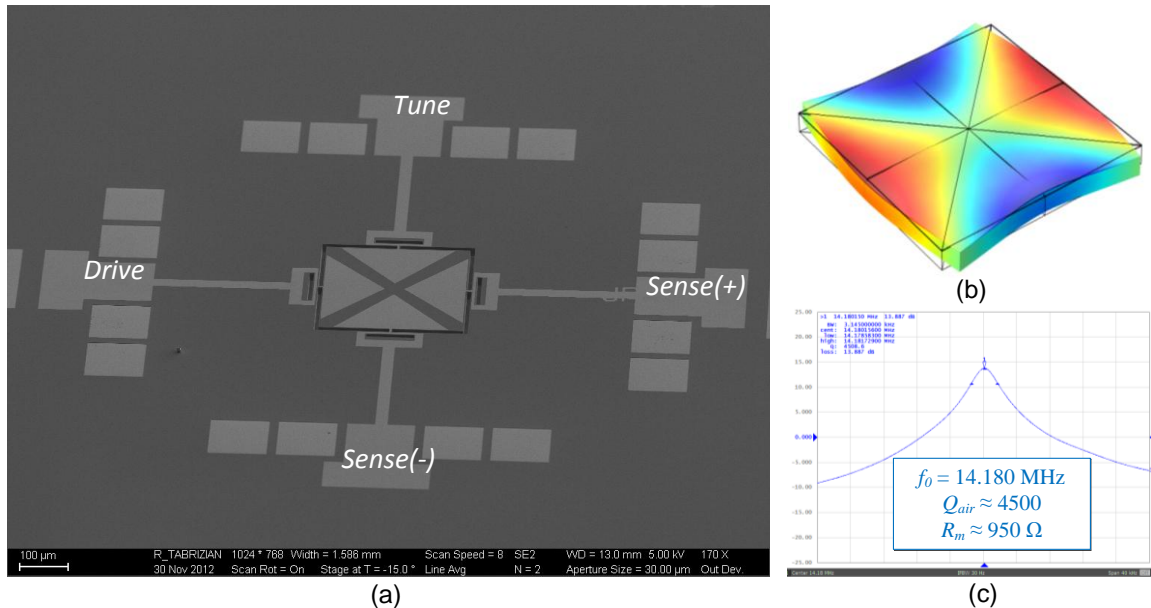
Figure 4.12: (a) SEM picture of the 4-port AlN-on-Si square resonator showing the electrode configuration, (b) Stress field pattern of the BAW square resonator, (c) Frequency response of the square BAW resonator shows a motional resistance ≈ 950 Ω, and quality factor of ~4500, at $f_0 ≈$ 14.18 MHz.

4.3.2   Circuit Implementation and Characterization Results

In a measurement setup similar to Figure 4.3, an Agilent E5071C Network Analyzer is used to measure the frequency response of the tuned 4-port square resonator of Figure 4.12. The differential sense output current of the resonator is picked off by a differential TIA with a gain of 4.7 kΩ. An analog all-pass phase-shifter circuit is used to generate the tuning displacement signal from a single-ended output of the TIA. The tuning signal is then scaled by an analog multiplier to be applied to the tuning port of the resonator. The scaling coefficient is provided by an external DC supply voltage that controls the gain of the analog multiplier. The differential TIA used for current pick-off is THS4501 from Texas Instruments (TI) and the single-ended amplifiers used for buffering and phase-shifting are AD8058 dual amplifier ICs; the analog multiplier is AD835, both from Analog Devices Inc (ADI).

Figure 4.13 shows the results of open-loop tuning of the 14.2-MHz resonator, by applying a tuning DC voltage in a range of [-600mV, 600mV], where the tuning voltage changes in steps of 200 mV. As shown in Figure 4.13a, the magnitude response of the resonator shows no significant variation of insertion loss or quality factor, implying that the phase error, $\Delta\varphi$, in the tuning loop is negligible. The phase response of the tuned resonator in Figure 4.13b shows ~14 kHz, i.e. 1000 ppm of linear active frequency tuning, with a slope of 833 ppm/V.

The amplifier gains are carefully designed such that ±4V headroom of AD8058 buffer becomes the bottleneck of the tuning performance. Therefore based on (4.14), the maximum linear tuning range of the oscillator with 600mV peak amplitude is limited to ~1480 ppm. To characterize the tuning performance of the system, the tuning voltage is swept in a range of [-1V, 1V], and the frequencies are measured using an Agilent 53181A frequency counter.

In a closed-loop oscillator setup similar to Figure 4.4, the differential TIA output is buffered by a VGA to drive the input port of the resonator. The VGA gain is controlled
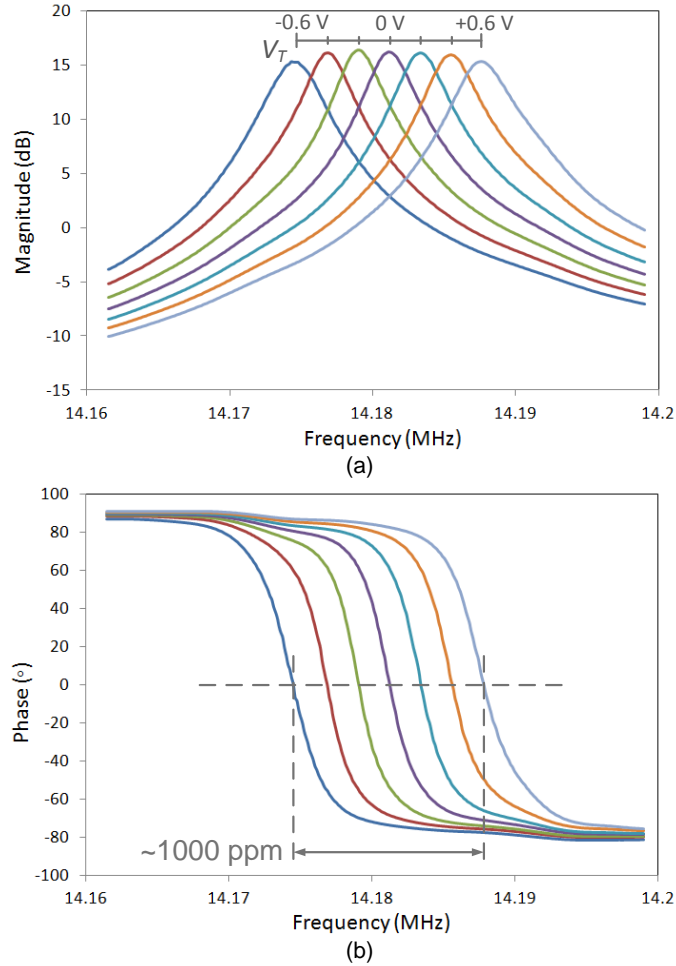
Figure 4.13: (a) Magnitude response of the tuned 14.2MHz resonator; no significant variation in insertion loss or quality factor of the resonator can be seen due to accurate phase adjustment of the tuning loop, (b) phase response of the tuned resonator; an overall tuning of ~1000 ppm is achieved.

by a PI controller to stabilize the TIA output. The VGA used in the PCB implementation is VCA810 from TI. The 14.2-MHz resonator is interfaced with this closed-loop oscillator on a PCB prototype, to demonstrate a MEMS VCO.

As shown in Figure 4.14, a linear tuning slope of 830 ppm/V with an overall bidirectional tuning range of 22 kHz, equivalent to 1550 ppm was measured from active tuning of the closed-loop oscillator. The measured tuning slope is in good agreement with the theoretical value of 824 ppm/V calculated based on a TIA gain of 4.7 kΩ, phase-shifter gain of 1.5 V/V, $R_m = 950$ Ω, and $C_m = 2.625$ fF.
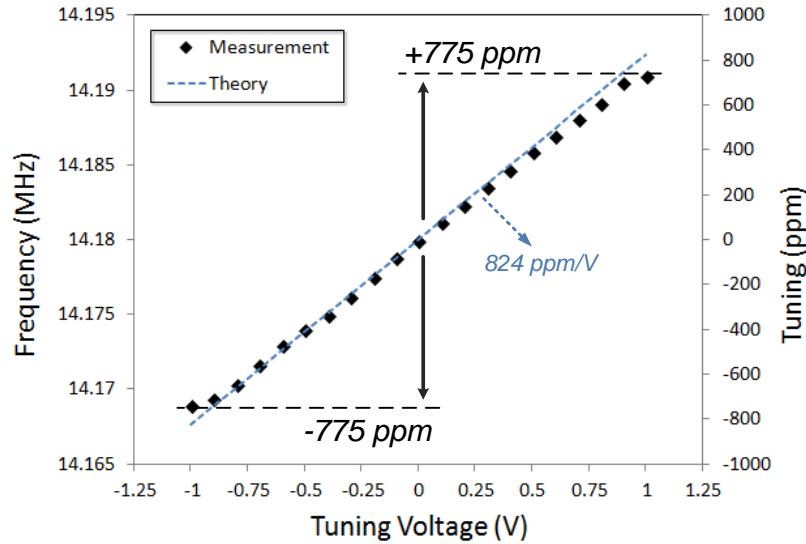
Figure 4.14: A maximum tuning range of 22 kHz, equivalent to 1550 ppm (±775 ppm) has been achieved using the MEMS VCO implemented based on the proposed tuning scheme. The resonator is tuned in both positive and negative directions with a slope of 830 ppm/V, which is in close agreement with the theoretical slope of 824 ppm/V.

The effect of active tuning on phase noise of the closed-loop series-mode oscillator can be categorized into two major effects. The first is the effect of active tuning on the effective quality factor and motional resistance of the resonant mode due to tuning path nonidealities particularly delay-induced phase errors. Such effects can be evaluated by the Leeson's formula [52], [58]. The second major effect is caused by the noise of the tuning path amplifiers, identical to the effect of the random noise of the DC tuning voltages used for electrostatic tuning, on the phase noise of capacitively actuated oscillators, which is typically of minor concern if designed sufficiently carefully. This leaves the first error source as the main cause of phase noise degradation in the active tuning scheme.

Figure 4.15 shows the results of phase noise measurements on the MEMS VCO, at three different corners of the tuning range, i.e. at V_T values of -800 mV, 0V, and 800mV, where phase noise values of -110.24 dBc/Hz, -110.58 dBc/Hz, and -111.34 dBc/Hz are measured respectively, at 1 kHz offset frequency. As can be seen, with careful matching of the phase in the tuning loop, the same phase noise performance can
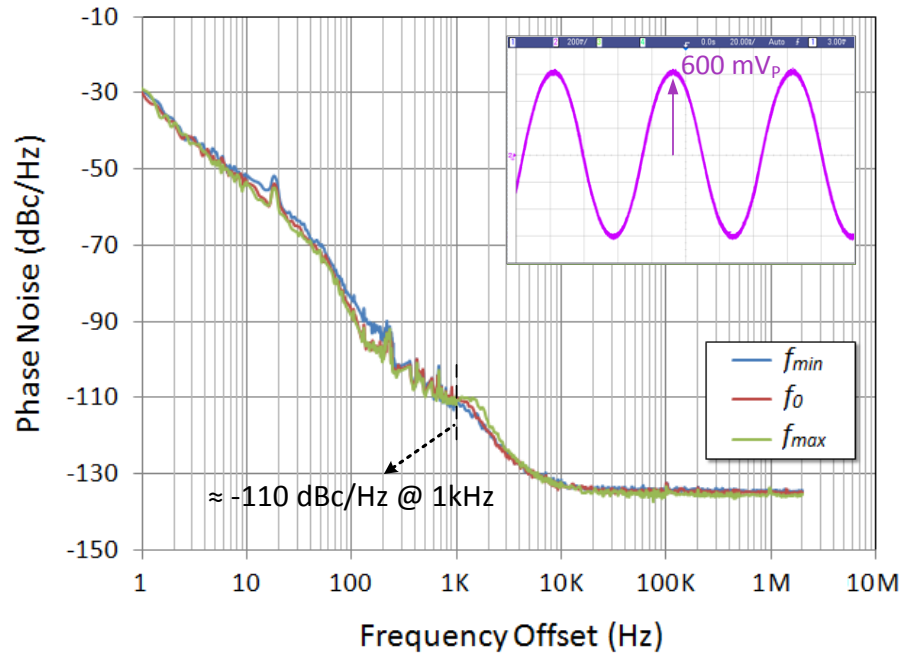
Figure 4.15: Phase noise performance of the oscillator is measured at three different corners of the tuning range, i.e. at -800 mV, 0 V, and 800mV, where phase noise values of -110.24 dBc/Hz, -110.58 dBc/Hz, and -111.34 dBc/Hz were measured respectively, at 1 kHz offset frequency. The top right inset shows the 600 mV$_P$ closed-loop sinusoidal oscillation at 14.18 MHz.

be maintained at all corners, and the tuning loop nonidealities do not cause significant

degradation on the phase noise performance of the MEMS VCO across the tuning range.

CHAPTER 5

SELF-CALIBRATED DUAL-MODE GYROSCOPE INTERFACE ARCHITECTURE

The performance metrics for gyroscopes were introduced in Chapter 1, and different device-level and system-level error sources were described in the first three Chapters of this thesis. Chapter 1 described the basic limitations on bias and scale factor stability and their dependency on the variations of the mode coupling terms, variations of the sense-mode quality factor, and the uncontrolled frequency split between the gyroscope modes. In Chapter 2, a deeper insight into the basic equations of Coriolis resonant gyroscopes was presented, the general transfer function of Coriolis gyroscopes was derived, and the effect of rotation and coupling terms on the mode-matched condition of such gyroscopes was explored. Chapter 3 covered the basic operation principles of axisymmetric BAW gyroscopes, and the basics of interface circuit and system design for Coriolis resonant gyroscopes, followed by more advanced architectures for quadrature cancellation and closed-loop operation that partially mitigate the bias and scale factor drift errors in MEMS gyroscopes. In order to further reduce the effect of nonidealities on the drift of gyroscope bias and scale factor, self-calibration schemes are required that can distinguish the error sources, estimate their contribution to the overall performance instability, and reduce the corresponding error contribution.

Extensive research has been directed towards in-situ calibration of bias and scale factor in MEMS gyroscopes over the past few years, in two main categories: miniaturized micromachined rotary stages for scale factor calibration, and electrical self-calibration schemes for compensation of bias and scale factor drift errors [59]-[60]. Mechanical rotary stages provide means to physically apply certain rotation rates to the gyroscope, and thus provide a relatively accurate estimate of the gyroscope scale factor [61]-[63]. However, the estimation has to be taken at stationary condition, i.e. $\Omega = 0$, which limits

the applicability of the scheme where online calibration is required. Moreover, such rotary platforms fundamentally cannot compensate for bias errors in gyroscopes. In such schemes, the gyroscope device needs to be implemented on the rotary platform, which makes the fabrication of the combined system challenging [62]. Furthermore, the compliant flexures used in such devices to provide mechanical rotations of different amplitudes, can degrade the shock survivability of the overall device.

The above-mentioned limitations, together with the ease of electrical signal processing make electrical self-calibration techniques the preferred method for error compensation in MEMS gyroscopes. The phase-based readout technique introduced in [30]-[31], relies on simultaneous I/Q excitation of the gyroscope degenerate modes to translate rotation rate into modulation of the gyroscope signal phases with respect to the reference actuation signals, thereby detecting rate in terms of degrees as a self-calibrated identity. Self-sustaining implementation of this phase-based scheme using the gyroscope itself as the resonant oscillatory element, results in the quadrature frequency modulated (QFM) gyroscope architecture in [32], which suffers from significant temperature-induced drift in performance, due to its frequency-based nature. The bias compensation schemes presented in [64]-[65] provide effective cancellation of the temperature effects for the frequency-based gyroscope architecture, however, this scheme still suffers from comparatively poor ARW performance, due to the inherently low rate sensitivity of the frequency-based architectures, as each °/s of rotation translates into 0.0028 Hz. For instance, rate integration for north-finding using such a gyroscope would require frequency detection with μHz-level resolution and high stability over long integration times, which is stringent for timing references and synthesizer systems. The inefficacy of PM and FM methods in providing self-calibrated yet high resolution rate output from MEMS gyroscopes, calls for innovative AM gyroscope solutions.

This chapter will introduce an amplitude-based dual-mode actuation and sensing scheme for axisymmetric Coriolis gyroscopes, which provides inherent bias cancellation,

81

in-run mode-matching capability using a direct mode-split measurement method [66], and online scale factor self-calibration capability by using differential scaled velocity feedback. The basic operation of the proposed scheme will be explained, followed by the analysis of nonidealities and possible ways to mitigate them.

5.1   DUAL-MODE GYROSCOPE SCHEME

The schematic of the proposed dual-mode gyroscope architecture is shown in Figure 5.1. Both $m = 3$ elliptical degenerate modes of a SD-BAW gyroscope are excited into oscillation with equal in-phase forces. Both mode outputs are sensed simultaneously. The difference of the two sense outputs is used to demodulate rate and cancel bias terms. Meanwhile, in order to provide self-sustaining actuation, the sum of the two sense outputs is used to close a drive loop around the gyroscope. An intuitive analysis shows that the difference operation cancels the common-mode equal bias terms in the individual outputs, and doubles the Coriolis contents to be demodulated in the coherent demodulator. In a similar manner, the summation cancels the differential Coriolis coupling between individual modes, making the drive loop independent of rate.
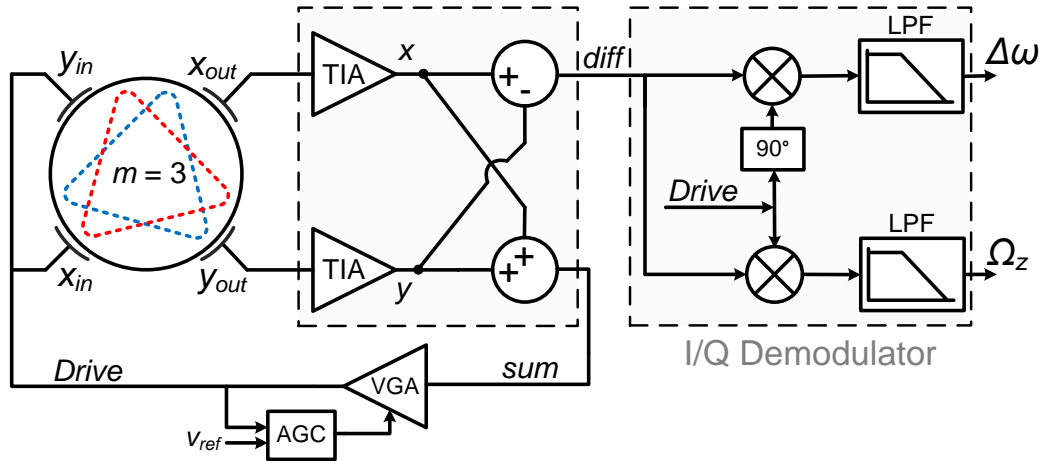
Figure 5.1: Proposed gyroscope architecture; both $n = 3$ modes of the 2.6-MHz BAW gyroscope are actuated and sensed simultaneously. The difference output is used for rate detection and summation is used to close the drive loop. The difference function cancels the common-mode bias output of the modes and senses the differential Coriolis output of the two modes with two-times higher sensitivity.

The gyroscope system of equations in (1.3) can be solved to evaluate the performance of the proposed scheme. In order to solve the equations in phasor domain, the frequency of operation, ω_0, must be determined primarily, so that the equations can be solved to find the individual outputs and the difference output at ω_0.

In order to simplify the calculations, (1.3) can be reduced to:

$$
\begin{bmatrix}
\omega_x^{\,2} - \omega_0^{\,2} + j\dfrac{\omega_0\omega_x}{Q} & j2\lambda\Omega_z\omega_0 \\[2ex]
-j2\lambda\Omega_z\omega_0 & \omega_y^{\,2} - \omega_0^{\,2} + j\dfrac{\omega_0\omega_y}{Q}
\end{bmatrix}
\cdot
\begin{bmatrix}
X(j\omega_0) \\[2ex]
Y(j\omega_0)
\end{bmatrix}
=
\begin{bmatrix}
F_0(j\omega_0)/m \\[2ex]
F_0(j\omega_0)/m
\end{bmatrix},
\tag{5.1}
$$

where the mode coupling terms are neglected, the two forces are equal in amplitude and phase, and most importantly the quality factor values of the two modes are equal. The latter is an ideal assumption which simplifies solving the equations. The case with unequal quality factor values will be explored in section 6.2.1.

Equation (5.1) can be solved to find x- and y-mode responses as follows:

$$
\begin{bmatrix}
X(j\omega_0) \\[2ex]
Y(j\omega_0)
\end{bmatrix}
=
\frac{F_0/m}{\det(A)}
\begin{bmatrix}
\omega_y^{\,2} - \omega_0^{\,2} + j\dfrac{\omega_0\omega_y}{Q} & -j2\lambda\Omega_z\omega_0 \\[2ex]
j2\lambda\Omega_z\omega_0 & \omega_x^{\,2} - \omega_0^{\,2} + j\dfrac{\omega_0\omega_x}{Q}
\end{bmatrix}
\cdot
\begin{bmatrix}
1 \\[2ex]
1
\end{bmatrix},
\tag{5.2}
$$

where $det(A)$ is the determinant of the gyroscope system of equations matrix, A. Consequently, the sum and difference displacements, X_{sum}, and X_{diff}, are derived from:

$$
X_{sum}(j\omega_0) = \frac{F_0/m}{\det(A)}\begin{bmatrix} 1 & 1 \end{bmatrix} \times
\begin{bmatrix}
\omega_y^{\,2} - \omega_0^{\,2} + j\dfrac{\omega_0\omega_y}{Q} & -j2\lambda\Omega_z\omega_0 \\[2ex]
j2\lambda\Omega_z\omega_0 & \omega_x^{\,2} - \omega_0^{\,2} + j\dfrac{\omega_0\omega_x}{Q}
\end{bmatrix}
\times
\begin{bmatrix}
1 \\[2ex]
1
\end{bmatrix}
$$

$$
X_{diff}(j\omega_0) = \frac{F_0/m}{\det(A)}\begin{bmatrix} 1 & -1 \end{bmatrix} \times
\begin{bmatrix}
\omega_y^{\,2} - \omega_0^{\,2} + j\dfrac{\omega_0\omega_y}{Q} & -j2\lambda\Omega_z\omega_0 \\[2ex]
j2\lambda\Omega_z\omega_0 & \omega_x^{\,2} - \omega_0^{\,2} + j\dfrac{\omega_0\omega_x}{Q}
\end{bmatrix}
\times
\begin{bmatrix}
1 \\[2ex]
1
\end{bmatrix},
\tag{5.3}
$$

which results in:

$$X_{sum}(j\omega_0) = \frac{F_0}{m} \frac{\omega_y^2 + \omega_x^2 - 2\omega_0^2 + j\frac{\omega_0}{Q}(\omega_x + \omega_y)}{\left(\omega_x^2 - \omega_0^2 + j\frac{\omega_0\omega_x}{Q}\right)\left(\omega_y^2 - \omega_0^2 + j\frac{\omega_0\omega_y}{Q}\right) - 4\lambda^2\Omega_z^2\omega_0^2}. \tag{5.4}$$

It can be seen from AC simulations, that the phase of X_{sum} crosses 90° only at the midpoint of ω_x and ω_y, i.e. $\omega_0 = (\omega_x + \omega_y)/2$, for $\Delta\omega < \omega_0/Q$. For $\Delta\omega > \omega_0/Q$, two additional 90°-crossing points will be generated by the individual modes. It can also be seen from closed-loop transient and PSS simulations, that the Barkhausen criteria for drive loop oscillation using the sum output, are satisfied at the midpoint frequency, as long as the mode split is smaller than *BW*, i.e. $\Delta\omega < \omega_0/Q$, while for larger values of mode split, the drive loop locks into the lower-frequency mode, since the sum magnitude is attenuated significantly at ω_0, as a result of the mode split.

From a mathematical point of view, 90° phase can be provided by making the real part of the numerator and the imaginary part of the denominator in (5.4) equal to zero at the same time. Equating the real part of the numerator to zero results in:

$$\omega_0 = \sqrt{\frac{\omega_x^2 + \omega_y^2}{2}} = \sqrt{\frac{\omega_x^2 + (\omega_x + \Delta\omega)^2}{2}} \approx \omega_x + \frac{\Delta\omega}{2} = \frac{\omega_x + \omega_y}{2}, \tag{5.5}$$

which is in agreement with the observations from simulations. It can be shown that in a high-Q gyroscope, i.e. $Q \gg 1$, at ω_0, the phase of the denominator will be very close to zero, resulting in the total phase of summation displacement to cross 90° at this frequency, even for split values relatively larger than *BW*. However, for split values larger than *BW*, the Barkhausen magnitude criteria is not satisfied at ω_0 anymore, resulting in the oscillator locking into the lower frequency degenerate mode.

At the ω_0 described by (5.5), the sum and difference displacements can be simplified as follows:

$$X_{Sum}(j\omega_0) = -\frac{2F_0}{m\omega_0^2} \frac{\left(\frac{\Delta\omega}{2}\right)^2 + j\frac{\omega_0^2}{Q}}{(\Delta\omega)^2 + \left(\frac{\omega_0}{Q}\right)^2 + 4\lambda^2\Omega_z^2 + j\frac{(\Delta\omega)^2}{2Q}}$$

$$X_{Diff}(j\omega_0) = -\frac{2F_0}{m\omega_0^2} \frac{\omega_0\Delta\omega + \frac{\omega_0\Delta\omega}{2Q} + j2\lambda\omega_0\Omega_z}{(\Delta\omega)^2 + \left(\frac{\omega_0}{Q}\right)^2 + 4\lambda^2\Omega_z^2 + j\frac{(\Delta\omega)^2}{2Q}}, \tag{5.6}$$

where $\Delta\omega = \omega_y - \omega_x$. Given that $\Delta\omega \ll \omega_0$, the $\Delta\omega^2/Q$ term in the denominator can be neglected compared to the $(\omega_0/Q)^2$ term. The $\Delta\omega^2$ term in the numerator of the summation displacement can also be neglected compared to the ω_0^2/Q, which proves that the 90°-crossing frequency remains close to $\omega_0 = \frac{1}{2}(\omega_x + \omega_y)$ for sufficiently small values of $\Delta\omega$, especially at near-mode-matched condition.

At relatively small frequency split between the modes, (5.6) can be simplified to:

$$X_{Sum}(j\omega_0) = -\frac{2F_0}{m\omega_0} \frac{j\frac{\omega_0}{Q}}{(\Delta\omega)^2 + \left(\frac{\omega_0}{Q}\right)^2 + (2\lambda\Omega_z)^2}$$

$$X_{Diff}(j\omega_0) = -\frac{2F_0}{m\omega_0} \frac{\Delta\omega + j2\lambda\Omega_z}{(\Delta\omega)^2 + \left(\frac{\omega_0}{Q}\right)^2 + (2\lambda\Omega_z)^2}. \tag{5.7}$$

Unlike in conventional single-mode AM gyroscope architecture, where only the sense output was affected by mode-split, in dual-mode scheme both drive (sum) and sense (difference) outputs are affected by mode split, through the denominator variations. Moreover, it can be seen that the displacement difference has a real component in its numerator that is directly proportional to mode split, while the imaginary component in

the numerator contains merely Coriolis signal. This quadrature-phase relationship can be utilized to provide a mode-split indicator that is fairly independent of the applied rate, to enable in-run monitoring of mode split, thereby facilitating in-run mode-matching.

It must be noted that the mode-split indicator is practically a function of both mode-split and rate. Therefore, it cannot be used to maintain a certain frequency split between the modes, in presence of time-varying rotation. However, for the purpose of in-run automatic mode-matching, the mode-split indicator can be nulled independent of the applied rotation, to maintain mode-matched condition, i.e. $\Delta\omega = 0$, during the operation of gyroscope. The effect of mode-split on the overall transfer function of the dual-mode gyroscope scheme emphasizes the importance of in-run mode-matching, which is facilitated by the scheme itself.

The quadrature-phase relationship of the two rates becomes a significant advantage of the dual-mode scheme over the conventional single-mode architecture, when recalling the effect of mode-split on the phase of the Coriolis output, as described by (1.6) in section 1.1.2. In order to adjust the demodulator phase to the phase of the Coriolis component, in presence of temperature variations, in single-mode mode-split architectures, LUT-based approaches have been used in [67], which require extensive characterization of the device quality factor over temperature, to create the LUT. With the dual-mode scheme however, as long as the drive loop locks into the midpoint of the two mode frequencies, the Coriolis and mode-split contents of the difference output maintain their I/Q phase relationship with respect to the input actuation signal, and therefore phase adjustment is not required in the demodulator. This improves the stability of the gyroscope scale factor and bias in presence of quality factor variations, and also reduces the complexity of interface system design and implementation.

5.1.1 Scale Factor and Signal-to-Noise Ratio

In the difference output, Coriolis coupling between the individual modes add up to double the overall rate sensitivity. At mode-matched condition, (5.7) is simplified to:

$$X_{Sum}(j\omega_0) = -\frac{2F_0}{m\omega_0} \frac{j\dfrac{\omega_0}{Q}}{\left(\dfrac{\omega_0}{Q}\right)^2 + \left(2\lambda\Omega_z\right)^2}$$

$$X_{Diff}(j\omega_0) = -\frac{2F_0}{m\omega_0} \frac{j2\lambda\Omega_z}{\left(\dfrac{\omega_0}{Q}\right)^2 + \left(2\lambda\Omega_z\right)^2}, \qquad (5.8)$$

which shows that the sum and difference are identical functions of rate and bandwidth. At mode-matched condition, the rate sensitivity of the dual-mode scheme is two times larger than the sensitivity of the same gyroscope used in conventional single-mode actuation scheme.

Since both modes contribute to the mechanical noise of the gyroscope, assuming that the *x*-mode and *y*-mode displacement noises are uncorrelated, the overall mechanical noise power will also double in the difference output, as compared to the single-mode AM gyroscope scheme. Therefore, the overall signal-to-noise ratio (SNR) of the gyroscope will also double, since the signal power is now 4-times larger than that in the conventional scheme. The two-fold increase in SNR theoretically translates into √2-times (~1.4-times) reduction in the value of ARW, as discussed in section 1.2.3.

As the split between the gyroscope modes increases, the sensitivity begins to decrease. At mode-split condition, assuming that the drive loop still locks into the mid-point of the two mode frequencies, although the differential Coriolis components still add up, the split between the drive frequency and the individual mode frequencies start to increase, and therefore the magnitude of both drive displacement and the Coriolis-
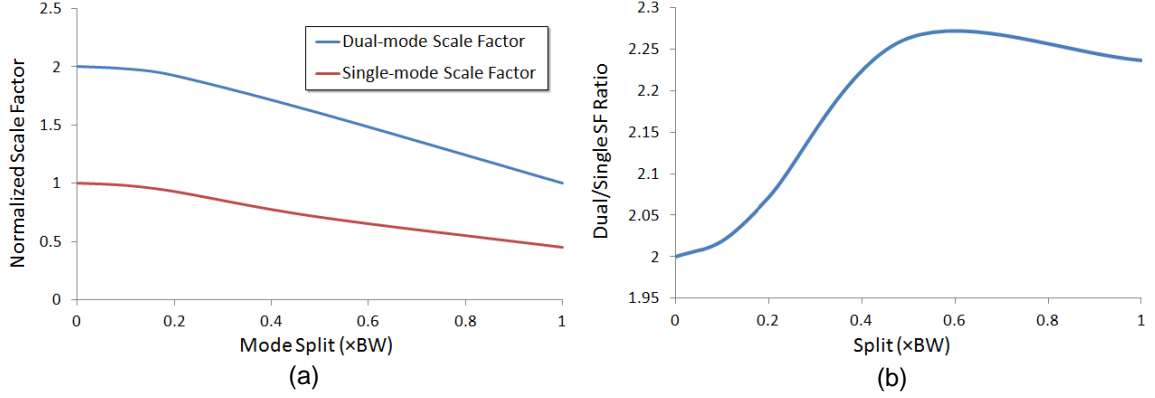
Figure 5.2: (a) Scale factor as a function of mode-split in both conventional single-mode actuation scheme and dual-mode scheme, for $\Delta f < $ BW, (b) the ratio of the two scale factor values at each Δf, showing that in this range, the scale factor of the dual-mode scheme is at least twice larger than the scale factor of the single-mode scheme.

induced displacements in individual mode outputs begin to decrease accordingly, as described by (5.7).

Figure 5.2a shows the comparison of scale factor in single-mode actuation and dual-mode actuation for $0 \leq \Delta\omega \leq BW$ based on (1.6) and (5.7), assuming that the demodulation phase is adjusted for maximum rate sensitivity in (1.6). As can be seen from Figure 5.2b, in this range, the scale factor of the dual-mode scheme is at least twice larger than that of the single-mode scheme. Assuming that the drive loop would still lock into the midpoint of the two mode frequencies for $\Delta\omega > BW$, the dual-mode scale factor would have become again twice larger than the single-mode scale factor at $1.4 \times BW$, and the two values would have become equal at $\approx 3.66 \times BW$, after which the single-mode scale factor would have surpassed the dual-mode scale factor. However, since this does not happen in reality, it is not shown in the plots of Figure 5.2.

As mentioned earlier before this section, for value of mode split, $\Delta\omega > BW$, the drive loop locks into the lower frequency mode, where the sum and difference outputs will be dominated by the output of that mode, resulting in no meaningful rate or bias. As will be explained later in section 5.1.3, this characteristic can be utilized to provide automatic initial alignment and matching of the gyroscope modes.

5.1.2 Inherent Bias Compensation

So far, the gyroscope equations were solved without considering the damping coupling and stiffness coupling. In presence of these coupling terms, and assuming that the frequency of the drive loop, f_{lock}, is still equal to the average of the two mode frequencies, the sum and difference displacements can be derived from (1.3) as:

$$X_{Sum}(j\omega_0) = \dfrac{-\left(\dfrac{2F_0}{m\omega_0}\right)\left[-\dfrac{\omega_{xy}^{\ 2}}{\omega_0} + j\dfrac{\omega_0}{Q} - j\dfrac{\omega_{xy}}{Q_{xy}}\right]}{\left[\left((\Delta\omega)^2 + \left(\dfrac{\omega_0}{Q}\right)^2 + 4\lambda^2\Omega_z^{\ 2}\right) + \left(\dfrac{\omega_{xy}^{\ 2}}{Q_{xy}^{\ 2}} - \dfrac{\omega_{xy}^{\ 4}}{\omega_0^{\ 2}}\right) - j\dfrac{2\omega_{xy}^{\ 2}}{\omega_0}\dfrac{\omega_{xy}}{Q_{xy}}\right]}$$

$$X_{Diff}(j\omega_0) = \dfrac{-\left(\dfrac{2F_0}{m\omega_0}\right)\left[\Delta\omega + j2\lambda\Omega_z\right]}{\left[\left((\Delta\omega)^2 + \left(\dfrac{\omega_0}{Q}\right)^2 + 4\lambda^2\Omega_z^{\ 2}\right) + \left(\dfrac{\omega_{xy}^{\ 2}}{Q_{xy}^{\ 2}} - \dfrac{\omega_{xy}^{\ 4}}{\omega_0^{\ 2}}\right) - j\dfrac{2\omega_{xy}^{\ 2}}{\omega_0}\dfrac{\omega_{xy}}{Q_{xy}}\right]}, \quad (5.9)$$

where the difference output has no undesired coupling terms in its numerator, due to the inherent bias cancellation properties of the dual-mode scheme.

The sum output has contribution from both coupling terms in its numerator, unlike the drive output in conventional single-mode scheme. While the damping coupling can slightly increase the insertion loss of the sum output, the quadrature-phase stiffness coupling term can shift the summation peak to lower frequencies, as shown in Figure 5.3a, where relatively large values of $a_q = \omega_{xy}^{\ 2}/\omega_0 = [0.4, 0.8, 2, 4]\times BW$ result in a frequency shift of a_q in the summation resonance peak. These large values, though impractical, are chosen to clearly show how the frequency modulation effect of quadrature coupling on the peak frequency of the sum output. In practice, the typical values of a_q are expected to be much smaller than the gyroscope BW.

Figure 5.3b shows the response of the difference output in presence of the same levels of quadrature error, and a constant rotation of $\approx 0.01\times BW$. It should be noted that without applying rotation in the simulations, the behavior of the difference output would
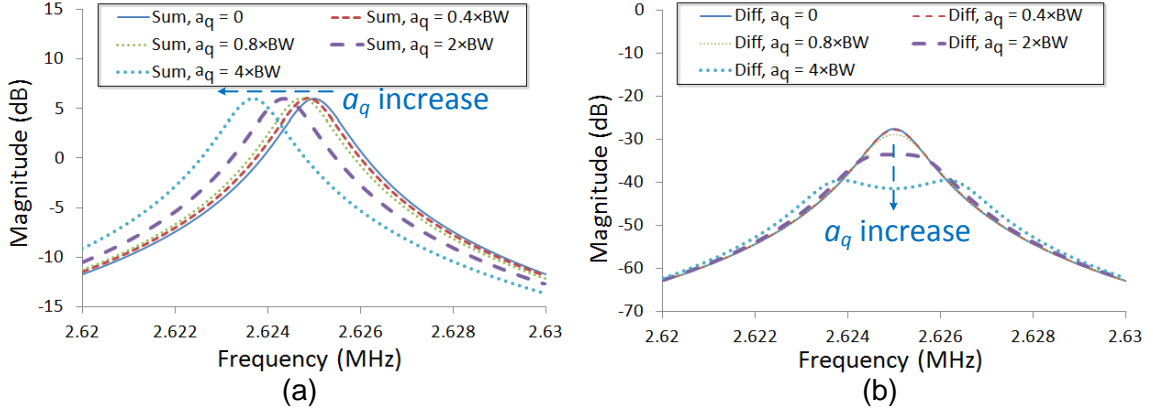
Figure 5.3: (a) the response of the sum output to different quadrature levels; it can be seen that as quadrature increases, the summation peak is shifted to lower frequencies than the natural mode-matched frequency of the gyroscope modes. This can result in rate leakage into the quadrature-phase demodulator channel, similar to the effect of mode-split in single-mode gyroscope. (b) the response of the difference output to different quadrature levels; a constant rotation rate of $0.01 \times BW$ is applied. The Coriolis frequency remains at the natural matched frequencies of the gyroscope resonance modes; the natural resonance modes split as a result of increase in quadrature.

have been less visible, due to complete bias cancellation in the difference output. As can be seen, the mode responses split symmetrically as a result of increasing quadrature in the system transfer function, in a similar manner to the single-mode scheme, and as described previously in Chapter 2. It can also be shown that the shift in the peak frequency of the sum output is equal to the frequency shift of the lower frequency mode, both equal to a_q.

In the presence of quadrature coupling, when rotation is applied, while the peak of the sum output shifts to a lower frequency, the Coriolis contents of the difference signal are still located at the original resonance frequency of the mode-matched gyroscope. The difference between f_{lock} and f_0 creates a phase-shift effect similar to the one caused by mode-split in the conventional single-mode scheme. As a result of the shift between the drive loop frequency and the Coriolis peak frequency, the Coriolis and mode-split components in the difference output leak from either of the I/Q channels to the other, complicating the recovery of both signals. Moreover, the variations of quadrature magnitude with temperature can cause further instability in rate sensitivity, and induce errors in the mode-split monitoring, in terms of both transfer function magnitude and

demodulation phase. Therefore, for robust operation of the system, either the shift in f_{lock} should be accurately estimated and compensated for in the demodulator, or the amount of quadrature causing the frequency shift must be kept sufficiently small, such that the frequency shift becomes negligible compared to the *BW* of the gyroscope.

It can be shown through simulations that the individual modes show a similar behavior to that of the sum output, i.e. the individual peak frequencies shift identically to the sum peak, while each peak magnitude is 6dB lower than the sum peak magnitude.

Based on the above, since the effect of quadrature reflects majorly on the frequency of the individual modes and consequently on the frequency of the sum output peak, the existence of quadrature coupling in the gyroscope cannot be easily detected. This complicates the implementation of quadrature nulling schemes that are needed for robust operation of the dual-mode gyroscope architecture. One possible way to detect the quadrature level in the dual-mode scheme is by characterization of the ratio of rate component in the I/Q channels of the coherent demodulator. The scale factor calibration technique that will be introduced in section 5.2 relies on inducing an electrically-generated virtual rotation in the mechanical gyroscope. The gyroscope response to this well-defined virtual rate can be utilized to estimate the quadrature level using the above-mentioned method.

5.1.3 Automatic Mode-Matching and Alignment Capability

A major limitation in conventional single-mode AM gyroscope architecture is the lack of a direct measure of mode-split especially during the gyroscope operation. This complicates the implementation of most automatic mode-matching schemes [7], [23]-[24]. The dual-mode architecture relieves this issue by providing the quadrature-phase component of the difference output current, as a direct proportional measure of mode-split. The mode-split indicator measured by the quadrature-phase channel in Figure 5.1 can be used to bring the mode frequencies back together, provided that a mode tuning
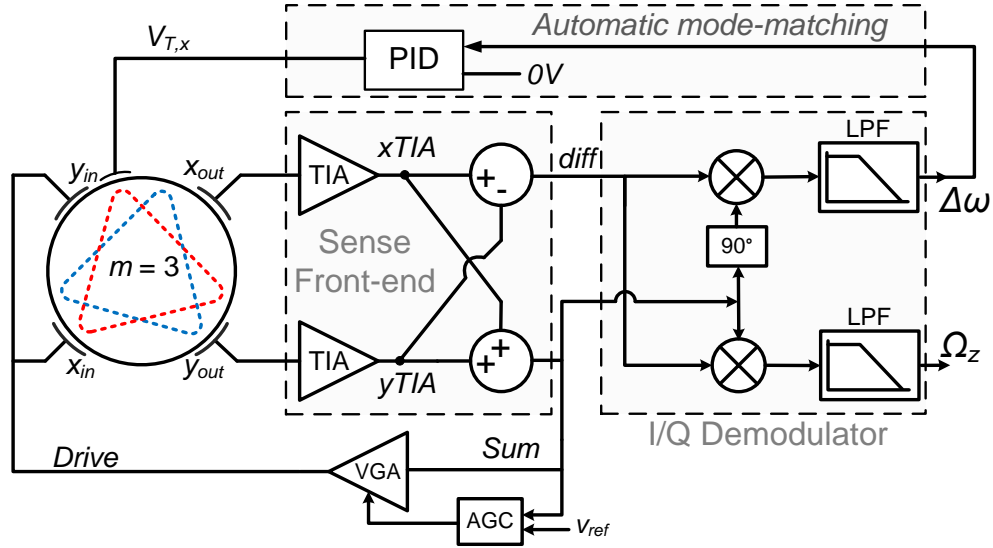
Figure 5.4: The implementation of in-run automatic mode-matching using a PID controller that nulls the quadrature-phase output, i.e. the mode-split indicator. The controller output provides the tuning voltage to the gyroscope modes, to make the mode frequencies equal.

mechanism is existent in the gyroscope. Figure 5.4 shows the implementation of in-run automatic mode-matching using a PID controller that nulls the mode-split indicator signal, thereby maintaining zero-split between the natural resonance frequencies of the two modes, even in presence of rotation.

An important enabling advantage of an in-run mode-matching loop in the dual-mode scheme, is the fact that since $\Delta\omega = 0$, the gyroscope transfer function is described by (5.8), where an AGC controller in the drive loop can be used to regulate the sum output as shown in the schematic of Figure 5.4. The AGC compensates for the rotation-induced energy loss of the sum signal, and also stabilizes the Coriolis force in the gyroscope by regulating the sum velocity, and consequently the individual velocities, in a similar manner to the discussion of section 3.2.1. In the absence of an in-run mode-matching controller, an AGC that regulates the sum output would compensate for the effects of both rate and mode-split, which could result in variation of the Coriolis force due to unpredictable changes of mode split.

The automatic mode-matching scheme in Figure 5.4 assumes that the modes are manually aligned. However, initial manual adjustment of quadrature coupling may not be

adequate, as the quadrature error might change with temperature variation or time, resulting in change of the overall gyroscope transfer function, thus the degradation of scale factor and bias. Therefore, in a self-contained dual-mode scheme, an automated mode-alignment and mode-matching method is required to provide initial alignment of the modes, and also maintain minimum quadrature during the gyroscope operation.

Figure 5.5 shows the effect of mode-split, in presence of quadrature coupling, on the sum and difference transfer functions in the dual-mode scheme. Different values of $a_q = \omega_{xy}{}^2/\omega_0 = [0.4, 0.8, 2, 4] \times BW$ are used, at a mode split of $\Delta\omega = 2 \times BW$, at stationary condition, i.e. $\Omega_z = 0$. Again, the values of a_q and $\Delta\omega$ are selected to be relatively large to exaggerate the effect of mode-split, in presence of quadrature. Figure 5.5a shows the response of the sum output. In the absence of quadrature coupling ($a_q = 0$), the sum magnitude and phase responses are symmetrical with respect to ω_0, while the gain at each mode frequency is lower than the 6dB peak gain at mode-matched condition, as was shown in Figure 5.3a. As the quadrature coupling increases, the gyroscope modes start to split further due to the additional quadrature term in the system determinant. At the same time, with increase of a_q, the gain of the transfer function increases at the lower-frequency mode and decreases at the higher-frequency mode, up to a point that at very high a_q values (e.g. $a_q = 4 \times BW$), the phase zero-crossing happens at the peak of the lower-frequency mode, which now has the same 6dB gain as the sum peak had at mode-matched condition.

This observation is counterintuitive, given the symmetry of the actuation and sensing scheme in the dual-mode architecture. The mathematical representation of the sum displacement for a stationary gyroscope, with mode split and quadrature, neglecting damping coupling, can provide a more in-depth understanding of the system behavior:
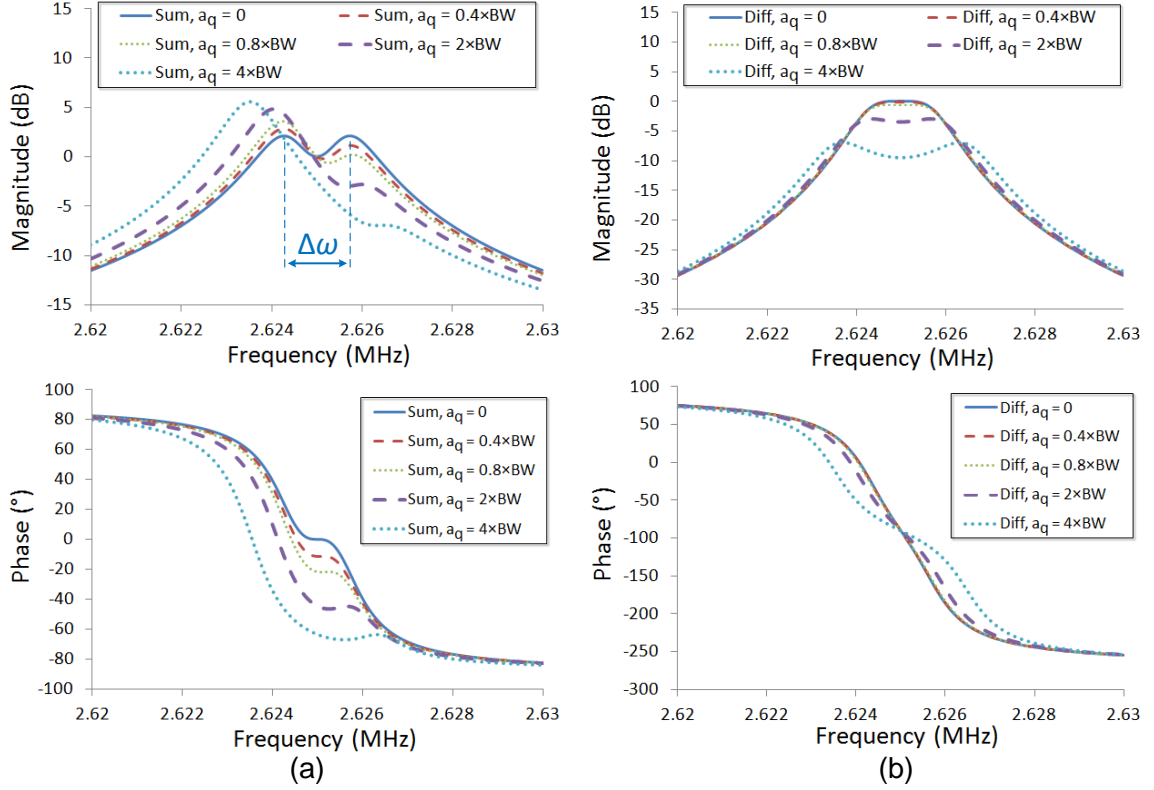
Figure 5.5: The effect of quadrature coupling on mode-split ($\Delta\omega = 2 \times BW$) gyroscope transfer function, (a) as quadrature coupling increases, the gain of the sum transfer function changes asymmetrically at the two mode frequencies; at very large quadrature levels, e.g. $a_q = 24 \times BW$, the phase zero-crossing happens at the peak of the lower-frequency mode, with the same 6dB gain as in the mode-matched summation peak, (b) the difference output responds symmetrically to both quadrature and split, due to its differential behavior; in the absence of quadrature, the difference output of the stationary gyroscope has only the quadrature-phase mode-split indicator component provide its maximum at frequency ω_0. However, with the increase of quadrature coupling, the quadrature-induced split causes the magnitude to drop at ω_0.

$$X_{Sum}(j\omega) = \frac{-\left(\dfrac{F_0}{m\omega_0}\right)\left[\omega_1^2 + \omega_2^2 - 2\omega_{xy}^2 - 2\omega^2 + j\dfrac{\omega_1 + \omega_2}{Q}\right]}{\left[\left(\omega_1^2 - \omega^2\right)\cdot\left(\omega_2^2 - \omega^2\right) + j\left(\omega_1 + \omega_2\right)\dfrac{\omega}{Q} - \dfrac{\omega_1\omega_2}{Q^2}\omega^2 - \omega_{xy}^4\right]}. \quad (5.10)$$

The summation displacement phase satisfies the Barkhausen criteria approximately where the numerator phase crosses 90°, i.e. the real part of the numerator becomes zero:

$$\omega_0 = \sqrt{\frac{{\omega_1}^2 + {\omega_2}^2 - 2{\omega_{xy}}^2}{2}} \Rightarrow \omega_0 \approx \omega_1 + \frac{\Delta\omega}{2} - \frac{{\omega_{xy}}^2}{2\omega_1}. \qquad (5.11)$$

As can be seen, ω_0 experiences a negative shift of ${\omega_{xy}}^2/2\omega_1$, almost equal to the quadrature-induced split described by (2.6). As a result, the gain of the summation peak at the lower-frequency mode becomes larger, almost equal to the sum of the two mode outputs, i.e. 6dB in the simulation of Figure 5.5a.

From an intuitive perspective, the bipolar mode-split and the unipolar quadrature coupling, both being displacement coefficients in the gyroscope system of equations, can be represented as the differential and common-mode displacement components of the dual-mode scheme, respectively. Therefore, at the frequency of one mode, which happens to be the lower-frequency mode, the common-mode quadrature component and the same-sign mode-split component add up to create a higher peak magnitude. On the other hand, at the frequency of the other mode, which is the higher-frequency mode, the two components have opposite signs, thus cancel each other. This justifies the asymmetry in the sum output at the two mode frequencies. Moreover, in the sum differential equation, the displacement coefficient that is used to determine the oscillation frequency is modified by the common-mode component only, since the differential mode-split components cancel out. Therefore the overall resonance frequency of the sum peak shifts in a unidirectional fashion. It can be shown that individual mode frequencies are also affected by the same common-mode value.

In the difference output, the common-mode quadrature components cancel each other while the differential mode-split components add up as the quadrature-phase component of the difference output current, as shown in Figure 5.5b. In the absence of quadrature coupling, the difference output of the stationary gyroscope contains only the quadrature-phase mode-split indicator component with its maxima at frequency ω_0. As quadrature increases, the quadrature-induced split causes the gain to drop at ω_0, as the

differential mode-split components symmetrically increase the gain at their respective split frequencies. In the absence of rotation and damping coupling, the phase zero-crossing of the output difference current remains 90°, at ω_0. The asymmetry of the system transfer function in presence of mode-split and misalignment can be used to provide methods and algorithms for initial alignment and matching of the gyroscope modes.

<u>Characterization results:</u>

An axisymmetric SD-BAW gyroscope [39] from Qualtré [40], with a mode-matched resonance frequency of 2.625 MHz, Q = 37,000, and R_m = 32.67 kΩ, is interfaced with the dual-mode gyroscope architecture of Figure 5.1. The differential output currents of each gyroscope mode are sensed and amplified by two TIAs in a pseudo-differential fashion, with 100-kΩ transimpedance gain. Summation and difference operations are provided by fully-differential inverting summing amplifiers. A gain of unity is used for summation amplifier, while the gain of the difference amplifier is chosen to be 4 V/V, for larger scale factor, to reduce the effect of quantization noise in lock-in amplifier ADC. The opamps used for TIA and summing operations are OPA657 and THS4501, respectively, both from TI. Thin-film surface-mount (SMD) resistors are used for their low excess noise performance [68]. Resistors with 100ppm accuracy are chosen for accurate gain matching of the sense channels. The design of the PCB is discussed in more detail in Section 5.3.2.

An HF2LI lock-in amplifier unit [69] is used to interface the gyroscope in both single-mode actuation and dual-mode actuation schemes, for comparison. The HF2LI unit has two output channels and two input channels that are reconfigurable to single-ended or differential. It also provides built-in phase-locked-loop (PLL) blocks for implementation of drive loop, by locking into a certain phase of the drive signal fed into any of the inputs. ADCs with 14-bit resolution are used at the input channels to digitize the inputs and 16-bit DACs are used to take the processed digital data from the processor unit and translate them to analog outputs. The processor unit provides digital coherent I/Q

demodulators for demodulation of in-phase and quadrature-phase components of the input signals, with respect to the carrier signal of interest. In case of single-mode actuation, the *x*-mode and *y*-mode output voltages are fed into channel-1 and channel-2 of the lock-in amplifier, respectively, while in case of the dual-mode scheme, the sum and difference outputs are fed into channel-1 and channel-2, respectively. In both cases, only channel-1 output is used as the drive signal. For dual-mode actuation, channel-1 output is fed into two inverting buffers, each driving one of the two gyroscope modes. Using two separate amplifiers, the two input actuation amplitudes can be adjusted to provide equal vibration amplitude to the two modes, in case the motional resistance values are mismatched, due to slight mismatches in quality factors or transduction coefficients of the two modes. At the same time, it guarantees that the two excitation signals are accurately in-phase, to avoid any partial phase or frequency modulation effects, similar to [30]-[32]. The effect of Quality factor mismatch between the modes will be discussed further in section 6.2.1.

Figure 5.6a shows the open-loop response of the gyroscope *x* and *y* modes in conventional single-mode scheme, in comparison with the response of the sum and difference outputs in the dual-mode scheme, using the same SD-BAW gyroscope device.
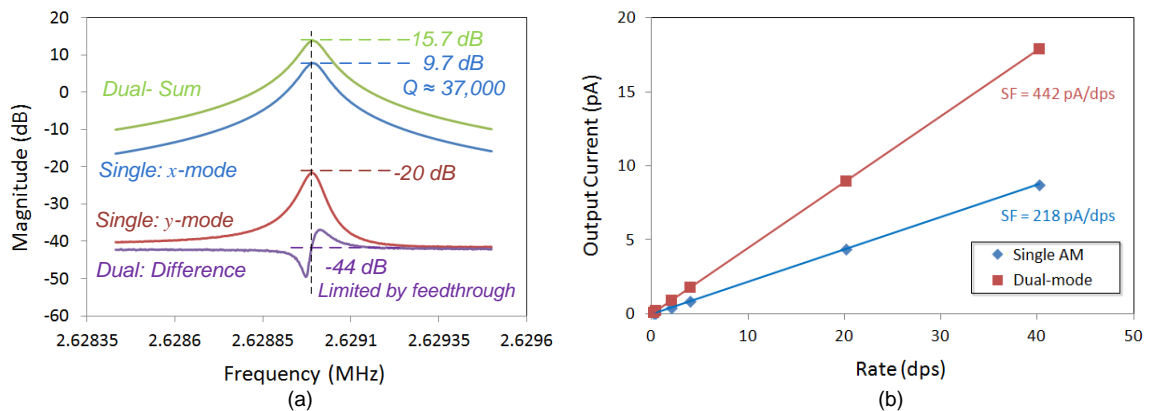
Figure 5.6: (a) open-loop response of the gyroscope in both single-mode and dual-mode configurations; the dual-mode configuration shows 24dB reduction of ZRO level, limited by PCB feedthrough, and 6dB lower insertion loss to the drive loop, (b) the dual-mode architecture doubles the rate sensitivity at mode-matched condition.

In single-mode configuration, the *x* mode shows an insertion loss of -9.72 dB at the mode-matched resonance frequency, while the sum output shows 6 dB lower insertion loss, as expected from (5.8). The *y*-mode output in single-mode configuration shows -20dB of quadrature level, while the difference output level at resonance frequency has a magnitude of -44dB, which is a reduction of 24 dB, equivalent to almost 15 times better drift performance in dual-mode architecture, compared to single-mode configuration.

Figure 5.6b shows the sensitivity plots for both conventional single-mode scheme and the dual-mode actuation scheme. The dual-mode architecture exhibits a sensitivity of 442 pA/°/s, which is twice larger than the scale factor of the conventional scheme.

Figure 5.7 shows the reduction of the ZRO at resonance frequency due to the inherent bias cancellation of the dual-mode architecture. As can be seen in Figure 5.7a, the spectrum of the sense (*y*-mode) output in single-mode configuration shows a ZRO peak with -68 dBV$_{rms}$ amplitude at the actuation frequency, while in the dual-mode sense (difference) output spectrum in Figure 5.7b, the ZRO peak amplitude is lower than the -70 dBV$_{rms}$ noise floor, after an additional difference amplifier gain of 4 V/V, making it

(a)

(b)
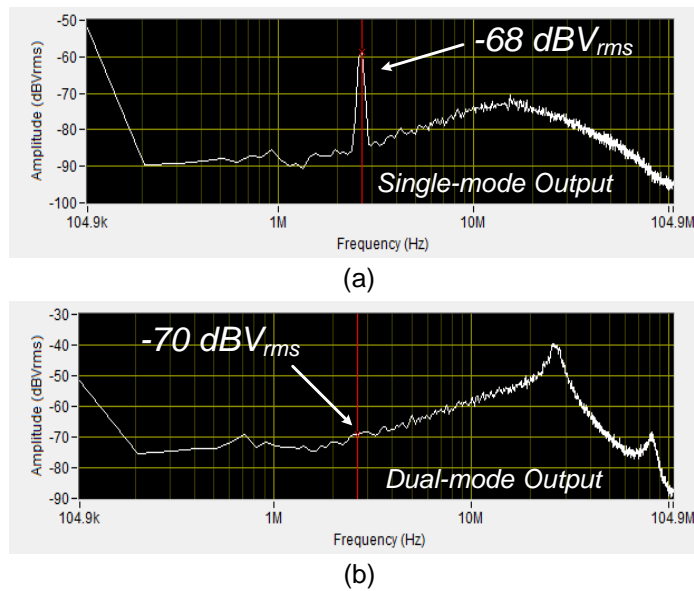
Figure 5.7: (a) sense-mode output spectrum in single-mode configuration shows quadrature amplitude of -68 dBV$_{rms}$, at carrier frequency, (b) in dual-mode configuration, the difference output shows -70 dBV$_{rms}$, after an additional 4× amplification, equivalent to 14dB (5×) improvement of ZRO.
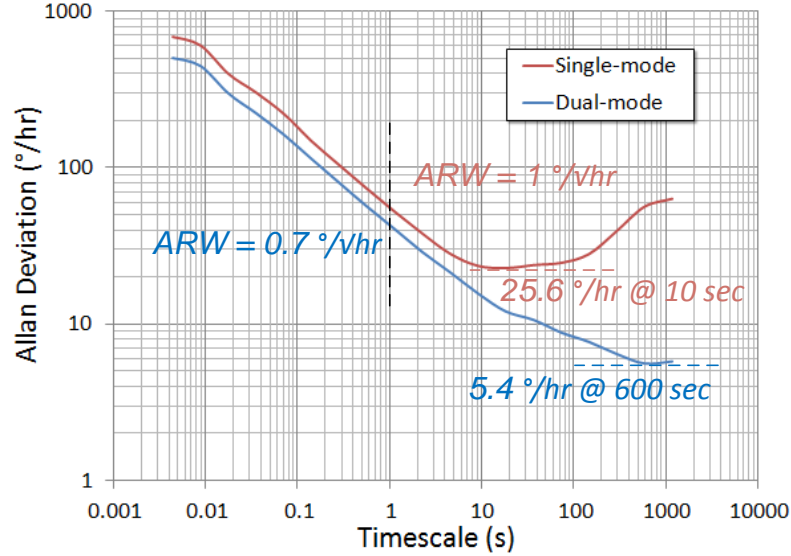
Figure 5.8: Allan deviation plots for both architectures; dual-mode architecture improves the bias drift of the gyroscope by almost 5-times from 25.6 °/hr at 10 sec, to as low as 5.4 °/hr at 600 sec. The ARW is consistently improved by 1.4 times, attributed to 3-dB SNR improvement.

equivalent to -82 dBV$_{rms}$ for fair comparison with the single-mode output. Therefore, the dual-mode scheme can reduce the ZRO magnitude by at least 14dB, which implies roughly 5-times reduction in the bias drift value.

Figure 5.8 shows the Allan variance results for stationary gyroscope in both configurations. Each measurement has been recorded for 2 hours at a sampling rate of 1.8 kSa/s. The Allan variance analysis is performed by AlaVar 5.2 [70].

The dual-mode actuation scheme improves the bias drift of the BAW gyroscope from 25.6 °/hr at 10 sec averaging time in conventional single-mode scheme to as low as 5.4 °/hr at 600 sec averaging time. The 60x improvement in averaging time makes this scheme more suitable for navigation applications. Unlike in most bias compensation schemes [21]-[22], the dual-mode architecture consistently improves ARW from 1 °/√hr down to 0.7 °/√hr, due to the 3-dB SNR enhancement.

In another set of measurements, the in-run mode-matching loop of Figure 5.4 was implemented to maintain the mode-matched condition across temperature. A PID controller in the HF2LI lock-in amplifier controls the tuning voltage of the *x*-mode, V_{Tx},
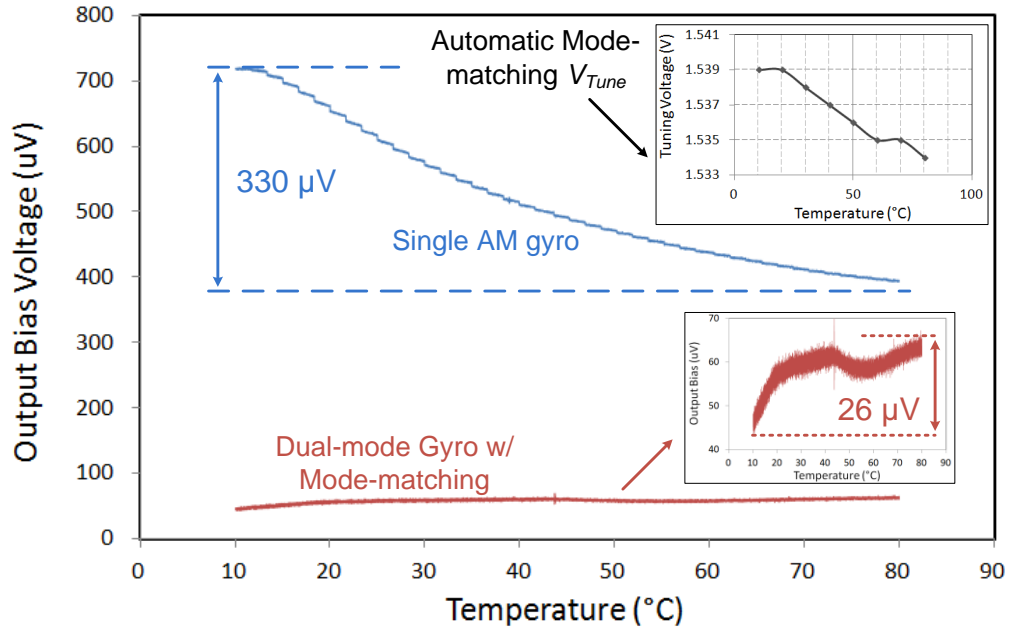
Figure 5.9: Output bias voltage of the sensor in both single-mode configuration, and dual-mode configuration with automatic in-run mode-matching, across a temperature range of 10-80 °C; the overall drift of output bias is reduced from 330 μV in single-mode configuration to only 26 μV in mode-matched dual-mode configuration. Top right inset shows the tuning voltage generated by the mode-matching PID controller, changing by ~5mV across the entire temperature range. The bottom inset shows the magnified dual-mode output bias voltage variation across temperature.

to keep the mode split indicator at 0 V, thereby maintaining mode-matched condition at all temperatures. Figure 5.9 compares the temperature drift of the gyroscope bias voltage in both conventional single-mode architecture and dual-mode architecture with in-run mode-matching. The bias cancellation technique together with in-run mode-matching reduce the overall drift of bias voltage from 330 μV in single-mode scheme down to only 26 μV in dual-mode scheme, across a temperature range of 10-80 °C. The top right inset shows a total change of 5mV in the tuning voltage generated by the PID controller to maintain mode-matched condition.

Figure 5.10 compares the input-referred bias in °/s for both configurations. The scale factor is measured for each scheme, at every 10 °C, to calculate the °/s equivalent values. The dual-mode scheme with in-run mode-matching demonstrates for the first time 45× reduction in the overall drift of bias, down to 3 °/s, over the 70°C temperature range.
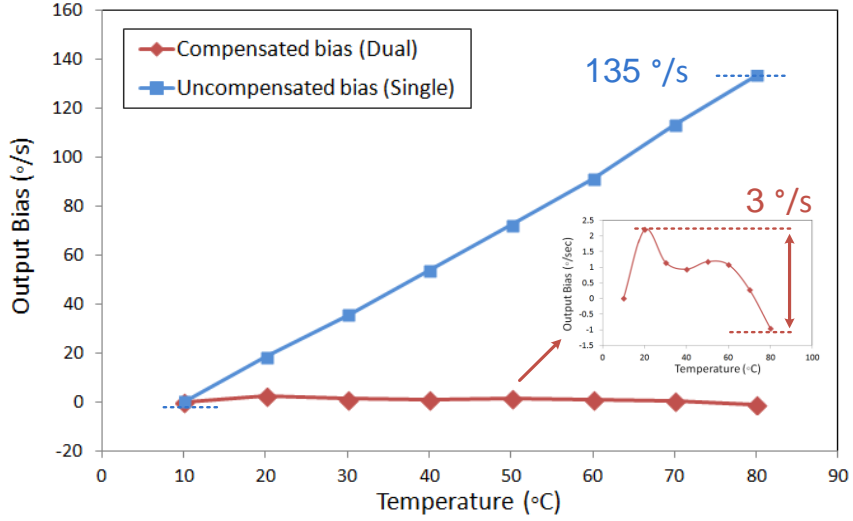
Figure 5.10: Output bias voltage is translated to equivalent input rotation; the overall bias variation across the temperature range of 10-80 °C is improved by 45×, from 135 °/s in single-mode configuration to only 3 °/s in dual-mode configuration with in-run mode-matching.

5.2   SCALE FACTOR CALIBRATION ARCHITECTURE

In the readout scheme of Figure 5.1, the Coriolis force couples the velocity of each mode to the other mode with opposite polarities, with a scaling of $\pm\lambda\Omega_z$. In an identical manner, in electrical domain, Coriolis coupling can be mimicked by providing scaled velocity feedback from each mode to the other, with opposite polarities. Since the resonance mode output currents are proportional and in-phase with their corresponding mode velocities, the output voltages of the individual TIAs can be used to provide the scaled velocity feedback.

Figure 5.11 shows an implementation of the proposed scale factor calibration scheme, adapted to the dual-mode readout architecture. As can be seen, the x-mode output current, proportional to x-mode velocity, is scaled by $-R_F$, multiplied by V_{cal}, and is applied to the y-mode input, while the y-mode output current is scaled by $+R_F$, multiplied by V_{cal} and is applied to the x-mode input to mimic the Coriolis effect.

The simplified gyroscope equations in (1.2), in the absence of mode coupling terms and with application of electrical calibration stimulus can therefore be rewritten as:

101
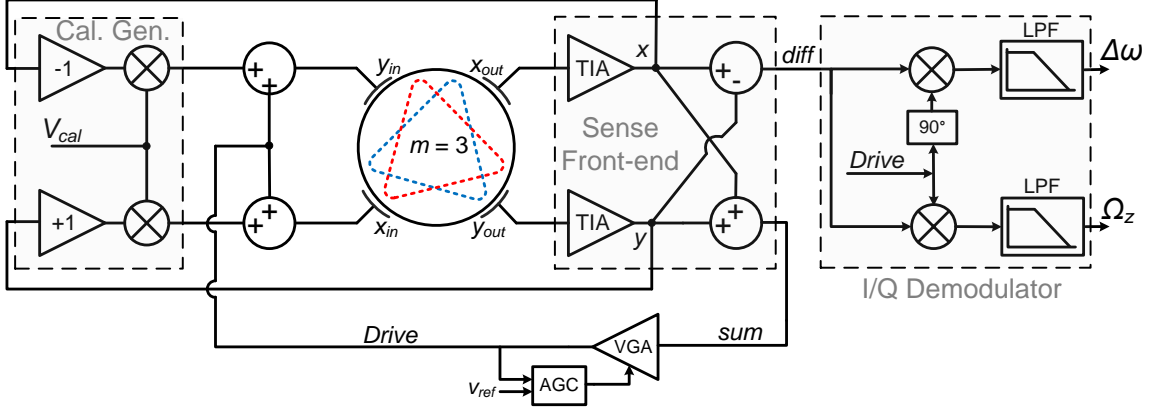
Figure 5.11: System implementation of the proposed scale factor calibration; velocity output of individual modes are differentially scaled and then added to the actuation inputs, in a cross-coupled fashion, to mimic Coriolis force.

$$m\ddot{x} + d_{xx}\dot{x} + k_{xx}x = f_0 \cos(\omega_0 t) - 2m\lambda\Omega_z\dot{y} - R_F V_{Cal}\eta^2\dot{y}$$
$$m\ddot{y} + d_{yy}\dot{y} + k_{yy}y = f_0 \cos(\omega_0 t) + 2m\lambda\Omega_z\dot{x} + R_F V_{Cal}\eta^2\dot{x}, \tag{5.12}$$

which can be represented in the phasor domain as:

$$\begin{bmatrix} \omega_x^2 - \omega_0^2 + j\dfrac{\omega_0\omega_x}{Q} & j\left(2\lambda\Omega_z + \dfrac{R_F\eta^2 V_{cal}}{m}\right)\omega_0 \\ -j\left(2\lambda\Omega_z + \dfrac{R_F\eta^2 V_{cal}}{m}\right)\omega_0 & \omega_y^2 - \omega_0^2 + j\dfrac{\omega_0\omega_y}{Q} \end{bmatrix} \cdot \begin{bmatrix} X(j\omega_0) \\ Y(j\omega_0) \end{bmatrix} = \begin{bmatrix} F_0(j\omega_0)/m \\ F_0(j\omega_0)/m \end{bmatrix}. \tag{5.13}$$

As can be seen, in the modified matrix, the rate component is now including a linear combination of both mechanical and electrical components, i.e. the overall response is the superposition of the two rates. Equation (5.13) can be solved to find the gyroscope response to both mechanical rate and electrical calibration rates as follows:

$$X_{Sum}(j\omega_0) \approx -\frac{2F_0}{m\omega_0} \frac{j\dfrac{\omega_0}{Q}}{(\Delta\omega)^2 + (\omega_0/Q)^2 + \left(2\lambda\Omega_z + \dfrac{\eta^2 R_F V_{cal}}{m}\right)^2}$$

$$X_{Diff}(j\omega_0) \approx -\frac{2F_0}{m\omega_0} \frac{\Delta\omega + j\left(\lambda\Omega_z + \dfrac{\eta^2 R_F V_{cal}}{m}\right)}{(\Delta\omega)^2 + (\omega_0/Q)^2 + \left(2\lambda\Omega_z + \dfrac{\eta^2 R_F V_{cal}}{m}\right)^2} \tag{5.14}$$

The gyroscope response to the electrical calibration rate V_{cal} can be used to calculate the sensitivity of the gyroscope system to mechanical rotation, given the value of the transduction coefficient, η^2. Moreover, the response of the gyroscope to electrical calibration rate can be monitored in real time, to capture the drifts of physical scale factor due to various common drift sources such as temperature-induced frequency and bandwidth variation, and compensate for them. However, it should be noted that the only source of drift that cannot be captured by this scheme is the variations of the transduction coefficient, η^2, which calls for efficient schemes to measure that parameter.

Since the system output is the superposition of the virtual and physical rates, the two rotations can be applied simultaneously, to provide online calibration of physical scale factor. The significant advantage of online scale factor calibration over offline scale factor calibration schemes such as [21], [31], is in the elimination of the time-varying errors in scale factor that can change from the calibration phase to the operation phase in [31], or from one phase of operation to the other in [21]. Using the scale factor drift information provided by the online calibration scheme, the drifts and nonlinearities in the demodulated mechanical rate can be compensated and readjusted.

In order to minimize the effect of simultaneous virtual rotation on the response of the gyroscope to physical rotation:

1) The magnitude of the virtual rotation should be sufficiently smaller than the rotation rate full-scale, determined by the gyroscope single-sided *BW*, as described in (1.19). With this condition, the virtual rate sensitivity can be used to track the physical scale factor changes that are caused by the environmental variations. Moreover, the scheme can capture the physical scale factor nonlinearities that are generated at large rotation rates. The upper magnitude limit of the virtual rate depends on the desired scale factor calibration accuracy. The lower limit of the virtual rate can be determined by the overall noise performance of the system. It is noteworthy that since the transfer function argument in the

dual-mode gyroscope system is a linear combination of the virtual and physical rotation rates, the limit of nonlinearity must be defined based on the absolute value of the sum of the two rotation rates. Furthermore, it can be shown that simultaneous application of relatively large (with respect to *BW*) physical and virtual rotation rates can result in nonlinearity of the gyroscope, but not in intermodulation of the two rotation rates, as it would have if the gyroscope output was a function of a nonlinear combination of the two rates.

2) The two rates should be distinguishable by a specific predefined characteristic of at least one of the two. For instance, the calibration rate can be applied at a specific frequency outside of the mechanical rate bandwidth defined by the specific application, yet in-band with respect to the gyroscope mechanical *BW*. This would need the gyroscope *BW* to be designed larger than the required bandwidth of the specific application.

An important difference between the nature of the electrical calibration rate and the applied mechanical rate is in the effect of frequency in the rate magnitude in each case. While, increasing both the frequency and the angular amplitude of the mechanical rate increase the rate magnitude in a proportionally linear manner, the magnitude of the electrical rate is not affected by changing its frequency. As a result, a DC electrical voltage generates the same virtual rotation as a sinusoidal voltage with the same peak amplitude would generate. Therefore, since the DC rate cannot be easily distinguished from bias variations, an electrical sinusoidal or square-wave stimulus with sufficiently small amplitude can be used at a relatively high frequency (preferably within the gyroscope bandwidth) to characterize the response of the gyroscope.

Proof-of-concept Implementation and Characterization Results:

The calibration scheme of Figure 5.11 was implemented on the PCB prototype used in characterizations of section 5.1, by adding analog multiplier ICs to the dual-mode architecture, to generate the calibration signals by modulating the velocity outputs of the

individual modes with a low-frequency electrical rate generated by a Rigol-DG4162 function generator.

As a proof of concept, the PCB prototype was interfaced with the HF2LI unit, in a configuration similar to the one described in characterization results of section 5.1. Figure 5.12 shows the time-domain response of the system to simultaneous application of a sinusoidal mechanical rate of 30 °/s peak-to-peak, and a square-wave electrical stimulus of 40mV$_{p-p}$, equivalent to ~39 °/s, at 0.05 Hz frequency. The results verify the fact that the output is the superposition of the two rates, provided that both rates are small enough not to drive the gyroscope transfer function nonlinear.

The equivalent mechanical rate for an electrical stimulus can be calculated by the relationship between Ω_z and V_{cal}, from (5.12), i.e. $\lambda\Omega_{eq}=R_F\eta^2 V_{cal}$, where $R_F=100\text{k}\Omega$, and $\lambda=0.54$. In this specific case, η^2 should be replaced with $\eta_1\eta_2$ that are calculated for actuation electrode width of 24°, and sense electrode width of 14°, for an outer radius of 325 μm. All electrodes see a polarization of 18 VDC across 270-nm gaps, and the device thickness is 40 μm. In this specific implementation, the multiplier output is attenuated by 50 times to generate equivalent rates <100 °/s. Considering an effective mass of 9×10^{-9} kg for the gyroscope, it can be shown that a stimulus of 40mV$_{p-p}$ represents ~39 °/s
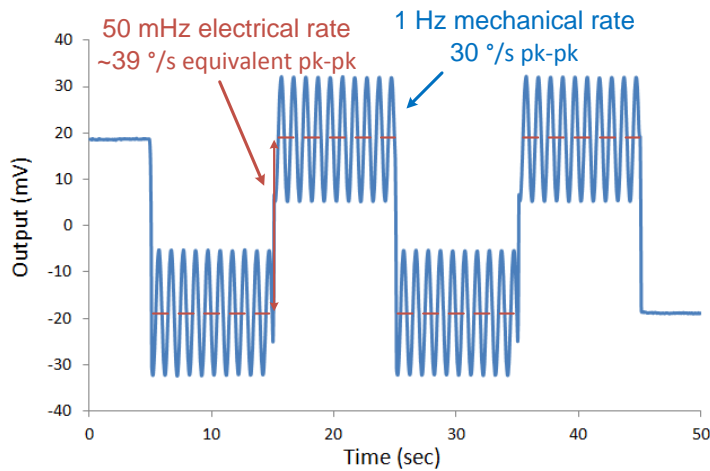

Figure 5.12: Simultaneous application of mechanical sinusoidal rate with 30 °/s peak-peak amplitude at 1Hz, and electrical square-wave stimulus of 40 mV$_{p-p}$ at 50 mHz frequency, with ~39 °/s equivalent rate peak-to-peak amplitude; the output is the superposition of the two rate inputs.

equivalent rotation rate.

To characterize the efficacy of the self-calibration technique, the scale factor is measured for both physical angular rotation rate and virtual calibration rate at different temperatures. Since temperature variation can induce noticeable changes in the scale factor, simple RMS or peak-to-peak measurements of each rate is sufficient for assessment of the functionality and effectiveness of the proposed scale factor calibration. In this set of measurements, after 1 hour soaking time in the rate table at each temperature, peak sinusoidal rotation rates of [10, 25, 50, 100] °/s at 1 Hz are applied to the gyroscope, followed by a sinusoidal calibration stimuli of [10, 20, 30] mV_{peak} at 50mHz. The peak-to-peak results of these sinusoidal excitations are measured accurately by the lock-in amplifier, and scale factor is calculated from the linear slope of the scale factor lines at each temperature. The temperature inside the rate table is swept in a range of 10-50 °C. The temperature is not reduced below 10°C, to avoid condensation, in case it could damage any of the circuits or the gyroscope.

Figure 5.13 shows the scale factor measurement results of physical rotation and electrical virtual rotation at each temperature. Figure 5.13a shows the physical scale factor ($\mu V/°/s$) measurement results at each temperature and Figure 5.13b shows the results of calibration scale factor (V/V) measurement. As shown in Figure 5.13c, both scale factor values change by almost 40% over the 10-50 °C temperature range. In this plot, the calibration scale factor is normalized to the baseline 10°C physical scale factor data point. The linear drop of both scale factors with temperature can be attributed to the linear reduction of quality factor as a result of temperature increase. It must be noted that in this gyroscope implementation, in order to avoid nonlinear actuation of the gyroscope at different temperature points, the drive input force is regulated rather than regulating the velocity of the modes. This results in such a high degradation of scale factor over temperature. Regulation of the output velocities could have reduced this temperature variation of scale factor, at the cost of transducer nonlinearity at higher temperatures.
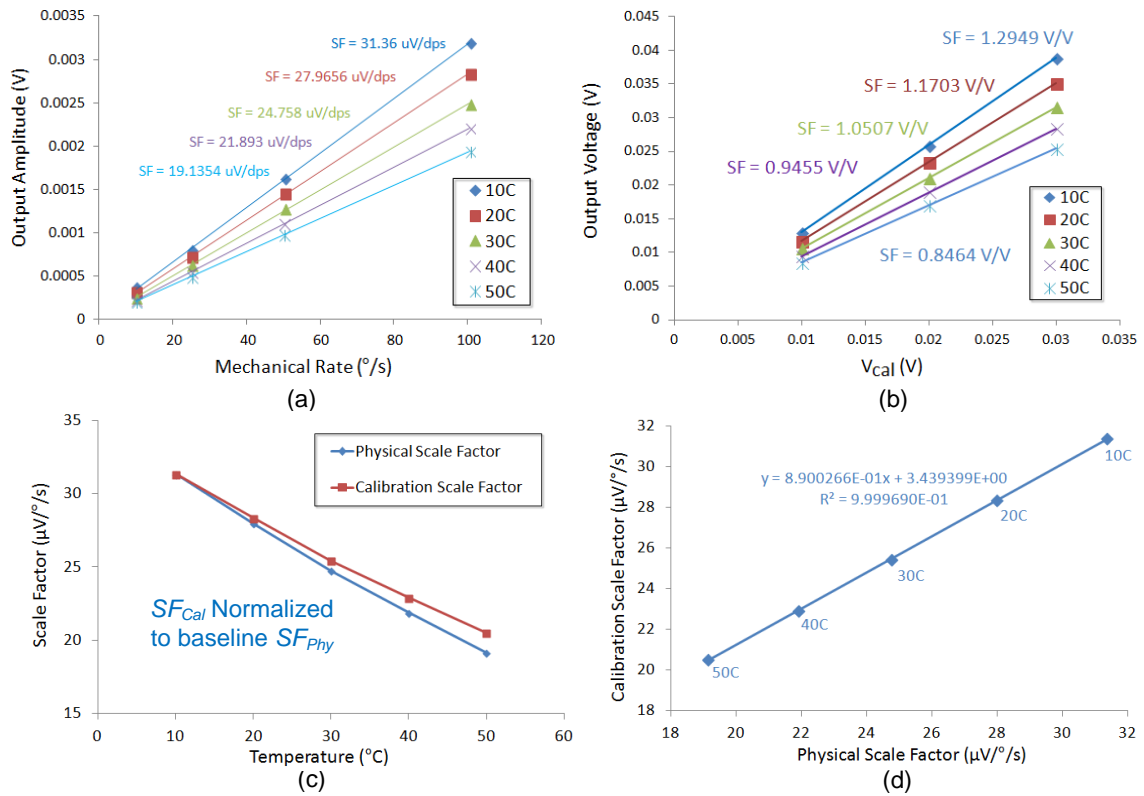
Figure 5.13: Calibration of physical scale factor with electrical scale factor estimate (a) physical scale factor measured every 10 °C over a temperature range of [10 - 50] °C using sinusoidal rotations of 10-100 °/s, (b) electrical scale factor is measured for the same temperature range, using 10mV, 20mV, and 30mV sinusoidal stimuli at 1Hz, (c) electrical scale factor is normalized to the baseline physical scale factor (at 10 °C) value; both physical scale factor and electrical scale factor values linearly drop with increase of temperature, (d) the electrical (calibration) scale factor is plotted as a linear function of physical scale factor; this linear relationship is used to calibrate the drifts in physical scale factor.

Figure 5.13d shows the calibration scale factor as a linear function of the physical scale factor. The calibration line shows a regression of $R^2 = 0.999969$ which is equivalent to ~31 ppm of accuracy. However, the line has a non-zero intercept point, which is due to the scale factor drift of the calibrating multipliers with temperature.

Figure 5.14 shows the temperature drift performance of the uncompensated scale factor and that of the compensated scale factor on the same plot, both measured from the dual-mode configuration. It has been confirmed through measurements that the single-mode scale factor follows the same variation as the uncompensated dual-mode scale factor. As can be seen, the uncalibrated scale factor changes linearly with temperature, while the calibrated scale factor shows a peak-to-peak drift of 0.35%, with $\sigma = 0.15\%$.
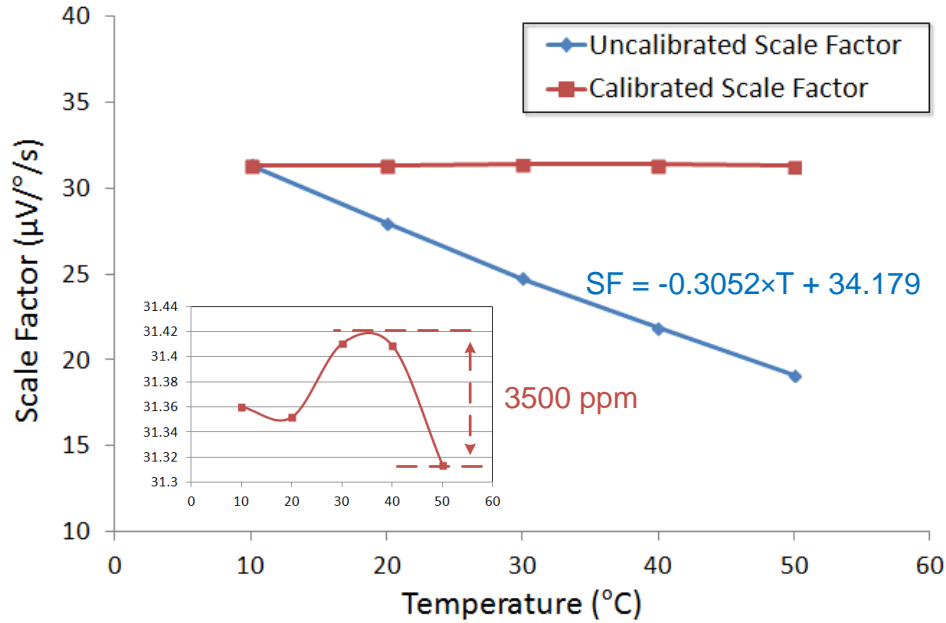
Figure 5.14: Physical scale factor temperature drift is calibrated by the electrical scale factor at each temperature. The linear drop of over 40% in scale factor over the [10 - 50] °C temperature range is reduced to below 3500ppm peak-to-peak scale factor error, which is an improvement of >100× in scale factor temperature stability.

The AD835 analog multipliers show considerable amounts of drift in both their offset and scale factor performances over temperature. The input offset, output offset, and scale factor of these mixers are reported to have maximum temperature variations of ±25 mV, ±10 mV, and ±9 %, respectively, across a temperature range of [-40 - 85] °C [71].

When used as calibration multipliers, the input offset mismatch between the two calibrating multipliers is modulated by the velocity signals to carrier frequency, and thus creates a fake DC electrical rate in the gyroscope. The value of this fake DC rate can drift with temperature, depending on the temperature behavior of individual input offsets, and thus degrade the bias performance of the gyroscope. The common-mode offset component of the two multipliers appears as an in-phase damping coupling term in the equations of the gyroscope. The output offset of the calibrating multipliers can be eliminated by means of high-pass filtering prior to summation with actuation signals. Otherwise, these offsets electrostatically detune the gyroscope modes.

The scale factor drift of the calibrating multipliers can create the non-zero intercept point in the linear relation of physical and calibration scale factor values, as seen in the scale factor measurement results of Figure 5.13d. Therefore, preliminary multiplier gain characterization is needed prior to calibration of the scale factor, complicating the overall calibration procedure. It can be shown that the mismatch of scale factors of the two calibrating multipliers can only have minor effect on the accuracy of the estimated rate, by changing the non-zero intercept point of the calibration scale factor as a function of physical scale factor.

The above analysis shows the importance of long-term stability and performance matching of the analog multipliers, calling for temperature-compensated analog multiplier design, or alternatively digital implementation of the dual-mode self-calibrated gyroscope, where zero-drift multiplication operation is provided by digital multiplier modules, leaving the major accuracy limitation to the resolution and drift of the front-end ADCs and actuating DACs.

In-run Bandwidth Characterization Functionality:

Since the electrical rate can mimic physical rotation, the electrical stimulus can also be used to estimate the bandwidth of the gyroscope in real-time. This online bandwidth characterization capability can be used for additional error compensations to the gyroscope overall transfer function.

Figure 5.15 shows the bandwidth characterization results using the proposed self-calibration scheme. The frequency of the electrical stimulus is swept from 0.5 Hz up to 60 Hz, and the output rate peak amplitude is measured at each frequency, as shown in Figure 5.15a. The amplitudes are plotted against the input frequencies, to obtain the equivalent low-pass transfer function of the gyroscope, shifted to DC. As can be seen, a 3-dB half-bandwidth of 36 Hz is estimated from this measurement, which is close to the actual 35.5-Hz half-bandwidth of the gyroscope modes.
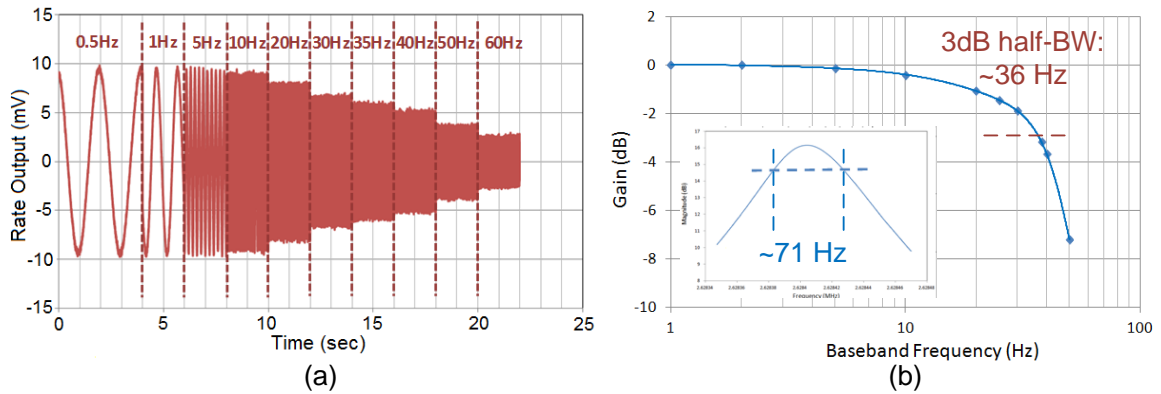
Figure 5.15: The scale factor calibration scheme can be used for bandwidth characterization; (a) time-domain output rate of the gyroscope, showing the attenuation at different input frequencies, in a range of 0.5-60 Hz, (b) the attenuation is plotted versus the input electrical rate frequency, showing a 3-dB half-bandwidth of 36 Hz, for a gyroscope with a half-bandwidth of 35.5 Hz.

The in-run bandwidth characterization capability is of key importance to characterization of high dynamic range gyroscopes, where mechanical rotary tables might suffer from limitations in generating relatively large mechanical rotation rates, at frequencies as high as 100 Hz. For instance, the maximum rate of the Ideal Aerosmith 1291Br rate table used for characterizations of this work is limited to 2000 °/s and thus cannot be used for full characterization of a gyroscope with 10,000 °/s full-scale range.

In-run Monitoring of Quadrature Coupling:

In a similar fashion to the in-run BW characterization scheme, quadrature coupling can also be monitored in-run, by means of applying a calibration stimulus at a specific frequency, and characterizing the quadrature-phase component of the difference output at the frequency of the stimulus. This additional quadrature-phase component can be nulled by means of a phase-shifter in both demodulator paths, to properly cancel the effect of quadrature on the frequency of the sum peak.

Discussion:

In the dual-mode self-calibrated scheme, the demodulated output rate can alternatively be nulled by PID controller in a closed control loop, to provide the virtual rotation rate required to counterbalance the applied mechanical rate, as shown in Figure 5.16. This scheme works in a similar manner to the force-to-rebalance architecture

described in Chapter 3. The main difference is that the rebalance operation is performed at lower frequency, and the forces are modulated and demodulated using analog multipliers. Moreover, the scheme shown in Figure 5.16 allows for nulling the in-phase and quadrature-phase components of the difference signal independently, to compensate for both mode-split and applied rotation, separately.

A significant advantage of the force-to-rebalance scheme of Figure 5.16 is the reduction of post-processing required for background calibration. More importantly, the force-to-rebalance operation nulls the time-varying component in the gyroscope transfer function, that is $2\lambda\Omega_z + \eta^2 R_F V_{cal} = 0$, which linearizes the transfer function significantly, and also eliminates the variations of the transfer function due to time-varying rotation.

Provided that mode-matched condition is automatically provided by a mode-matching scheme to the gyroscope system, and also provided that an AGC is used to stabilize the drive-mode vibration amplitude, the conventional single-mode force-to-rebalance architecture can also provide self-calibration of all scale factor drift errors, except for the drift of the transduction coefficient. In such a scheme, instead of providing a scaled velocity feedback, the constant drive-mode velocity reference voltage used by the AGC can also be used as a reference for the force-to-rebalance loop. However, in this
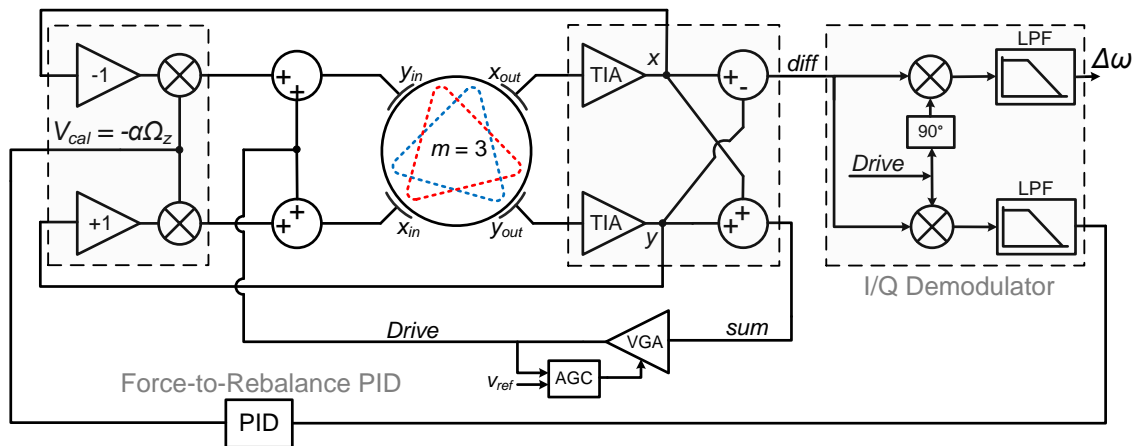

Figure 5.16: Force feedback can be used to null the difference output; instead of nulling the difference output the in-phase component after demodulation is nulled, while the quadrature-phase component is used for automatic mode-matching.

system, bias cancellation and automatic mode-matching are still required independently, to compensate for bias and mode-split errors. The advantage of using velocity feedback in the dual-mode architecture is that even in the absence of a mode matching scheme, and consequently in the absence of an AGC that stabilizes the mode velocities, mechanical scale factor can still be calibrated by means of scaled velocity feedback.

A similar scheme has been proposed in [72], in which the force-to-rebalance architecture is used in a mode reversal scheme, to null the difference output in one mode of operation, while the sum output is used to close the drive loop, and null the sum output in the other mode of operation, while the difference output is used to close the drive loop. In such a scheme, in the first mode of operation, the inputs are excited with equal in-phase forces, while in the second mode of operation, the equal forces have opposite phases. However, in the scheme presented in [72], there is no indication of a mode-matching or alignment scheme that can enable using an AGC in the drive loop to control the mode velocities to provide scale factor calibration capability.

5.3   SELF-CONTAINED SELF-CALIBRATED GYROSCOPE SYSTEM

A self-contained self-calibrated dual-mode gyroscope system is implemented for independent DARPA evaluation. The implementation is based on using commercially available discrete components, benefiting from the relatively short turn-around time of PCB fabrication and prototyping. The prototype was designed based on an all-analog interface system, due to the lack of simple yet sophisticated and sufficiently accurate platforms for sensors with such a high operation frequency as MHz-range BAW gyroscopes. The gyroscope system is powered by a single 12 VDC power supply with 2A max output current. Data acquisition is performed using an ADS1278 24-bit ADC backend at a sampling rate of 1 kHz. The rest of the system functionalities are provided internally by the self-contained system. This section describes the experimental design

112

criteria and details for the self-contained gyroscope system, and the characterization results of the overall system and its components.

5.3.1 Electrical Design Criteria and Mechanical Structure

The self-contained self-calibrated gyroscope system has to provide the following functionalities all on the same platform:

1) House the MEMS die and provide interface to electronics by means of bondwires

2) Provide actuation and TIA sense front-end

3) Dual-mode operation and calibration signal generation

4) Closed-loop actuation with automatic gain control

5) I/Q demodulation of the sense signals

6) Power supply and high-accuracy reference generation.

In order to provide the above functionalities with enough accuracy, using discrete components, a relatively large number of discrete components and consequently large board size are required. However, the independent characterization activity has a size limitation of 4×8 in^2, which is too small for the required volume of electronics. Moreover, a large PCB will introduce practical issues when it comes to wirebonding the MEMS die. Furthermore, ground bouncing can become a significant challenge when the size of the PCB increases beyond certain limits defined by the frequency of operation.

In this self-contained system shown in Figure 5.17, a modular approach has been taken, to not only address the above issues, but also provide ease of access and repair to each portion of the system. The system prototype is comprised of four PCBs mechanically connected to each other in a cube shape, by means of rectangular header connectors that provide both mechanical stability and electrical connections and communication between all four PCBs. The electrical header connections transfer signals, power and ground lines, and reference voltages from one board to the other. The modular design of the system, together with a 4-layer PCB implementation, allow for effective
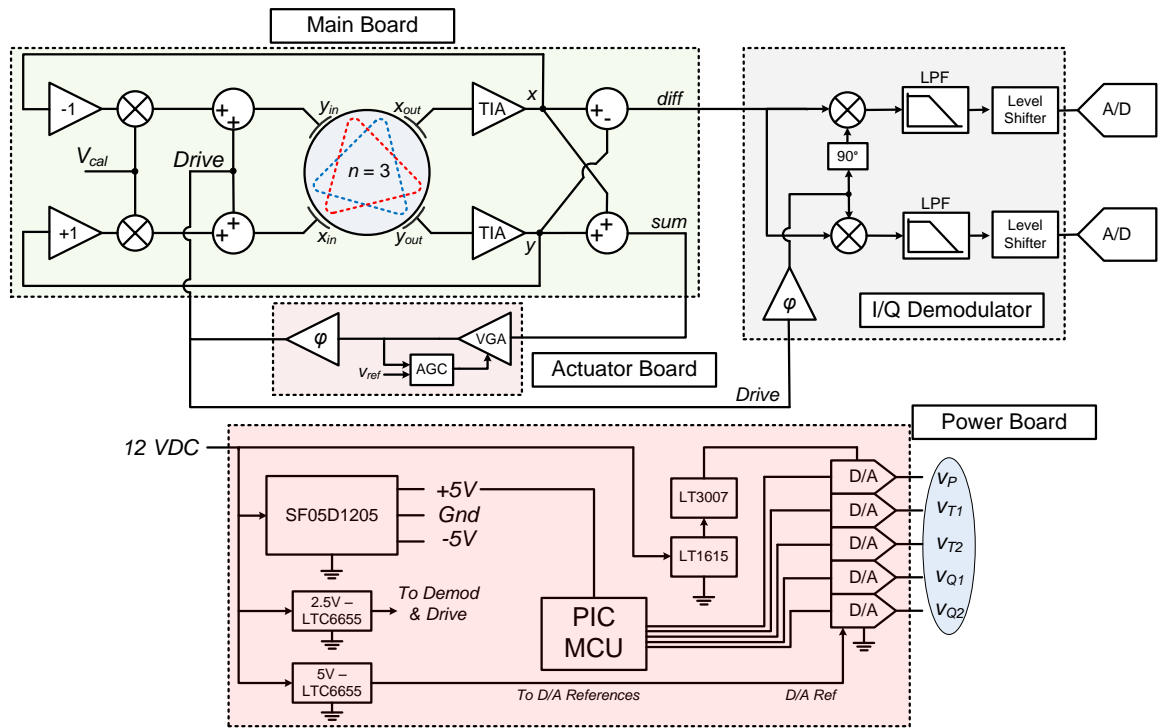
Figure 5.17: Self-contained self-calibrated gyroscope system is comprised of four different PCBs: Main PCB which houses the MEMS device and provides electrical interface to it, actuation PCB, demodulator PCB, and power generation PCB. The PCBs are connected mechanically and electrically by rectangular headers.

shielding of the gyroscope signals from one another. Below is a list of the boards and their design details.

5.3.2 Main Board

The main board, shown in Figure 5.18, fits on the top of the structure. This board houses the MEMS die (right inset), interfacing it with actuation and sensing electronics by means of bondwires. The MEMS output currents are sensed using 4 single-ended TIAs with gains of 100 kΩ. The opamp used for TIAs is OPA657 from TI. The main board also contains the additional inverting summing amplifiers required for summation and difference functions for the dual-mode operation. The summing amplifiers use THS4501 fully-differential opamps from TI.

For minimum phase degradation of the signal, the resistances are chosen to be no larger than 2 kΩ. Two AD835 analog multipliers from ADI are used for generation of
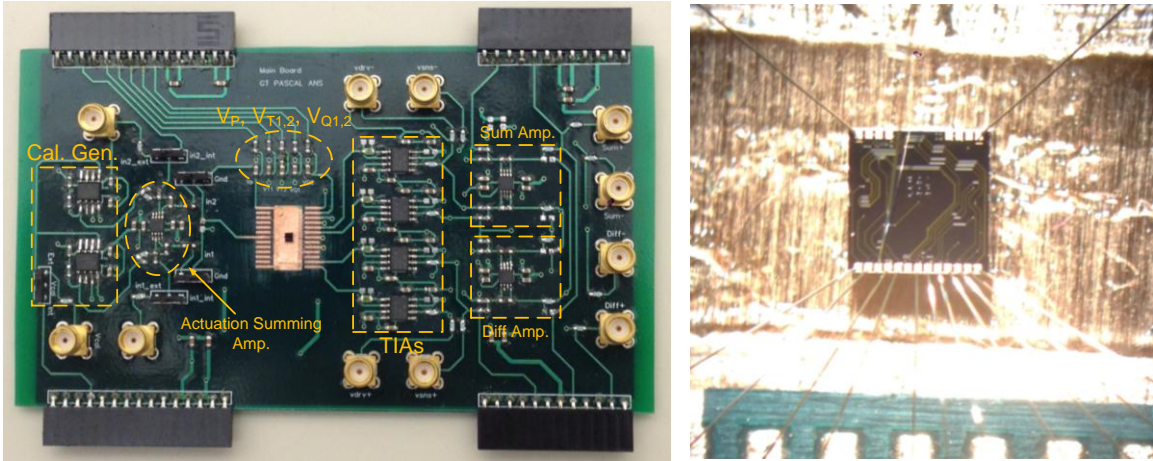
Figure 5.18: The main board is placed on the top of the structure; the MEMS die (right inset) is wirebonded and interfaced by TIA and actuation amplifiers. The dual-mode operation and self-calibration are provided by this board.

calibration stimulus from multiplication of the mode velocity signals and a low-frequency (0.1-10 Hz) sinusoidal/square-wave signal generated from a function generator. Two summing amplifiers using AD8058 dual-opamp ICs from ADI, add the input actuation signal and the calibration signals and apply them to the gyroscope modes. The polarization voltage and frequency and quadrature tuning voltages are received from the power board, to be applied to the gyroscope. Multiple sliding switches are added to be able to reconfigure the system from single-mode operation to dual-mode operation, and also from lock-in amplifier operation to operation within the self-contained self-calibrated system, for flexibility in characterization.

5.3.3 Closed-Loop Actuation Board

The closed-loop actuation board, shown in Figure 5.19, takes sense outputs from the main board, and uses them to generate sinusoidal actuation voltage to the gyroscope at certain peak amplitude, for either constant force or constant velocity, using an AGC controller. The input signal to this actuation board can be either one of the two mode outputs, used for single-mode operation, or the sum output used for dual-mode operation. Sliding switches are used to select the mode of operation, and to select the phase polarity
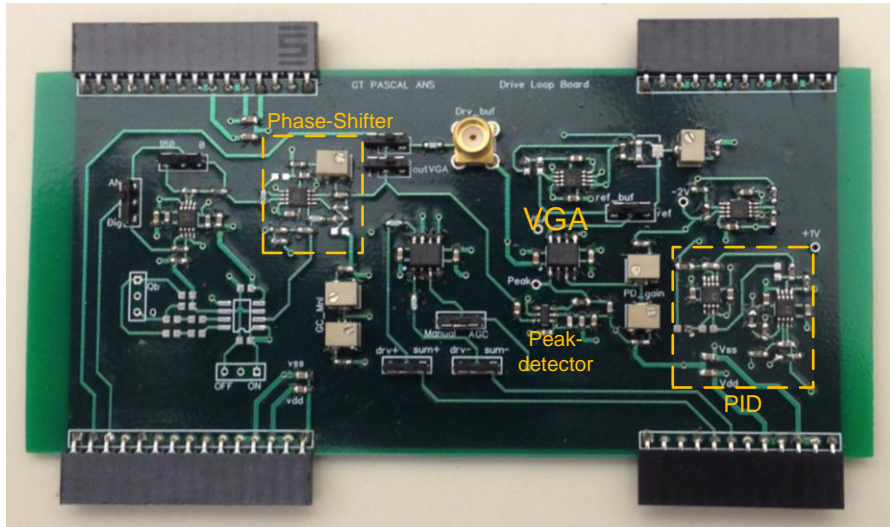
Figure 5.19: Closed-loop actuation board receives the drive/sum signals and generates a self-sustaining actuation signal for stabilized input force or output velocity. A peak detector and a PI Controller provide the AGC system.

to close the series-mode oscillation loop. The input signal is received and amplified by a VCA810 from TI, operating as VGA which gain is controlled by an AGC loop. The AGC output is phase-shifted by an analog all-pass phase-shifter to compensate for the phase delays of the TIAs and amplifiers in the drive loop chain.

The AGC loop is comprised of a peak detector IC that measures the peak amplitude of the desired sinusoidal signal, followed by a Proportional-Integral (PI) controller that controls the gain of the VGA to stabilize the desired amplitude to a certain peak voltage level. The desired signal to control is either the drive input to the gyroscope, to stabilize the input drive force, or the drive/sum output, to stabilize the velocity of the gyroscope modes, thereby stabilizing the Coriolis force. The peak detector used in the AGC loops is LTC5507 from Linear Technology, and the PI controller is implemented using a dual-opamp AD8058 IC from ADI. The references required for AGC operation are generated from references provided by the power board. The actuation signal provided to the main board, is also amplified and fed to the demodulator board to be used for demodulation.

5.3.4   Demodulator Board

The demodulator board, shown in Figure 5.20, receives the single-mode sense output and dual-mode difference output on one side, and the drive oscillation on the other side, to demodulate rate using analog multipliers and low-pass filters. To provide I/Q coherent demodulation, analog all-pass phase-shifters are used to generate quadrature-phase carrier signal. Another similar phase-shifter is also used in the in-phase carrier path, to compensate for the effect of sense TIA phase delay and the effect of frequency shift caused by residual uncompensated quadrature in the gyroscope.

The low-pass filters are 2nd-order low-pass Sallen-Key filters with bandwidth of 100 Hz. The outputs of filters are then level-shifted by a 2.5V reference to match the input voltage requirements of the ADC backend. The reference voltage is provided by the power board. The amplifiers used for level-shifting and low-pass filtering are AD8639 dual-opamps from ADI.

5.3.5   Power Board

The actuator and demodulator boards are placed on the two sides of the cube
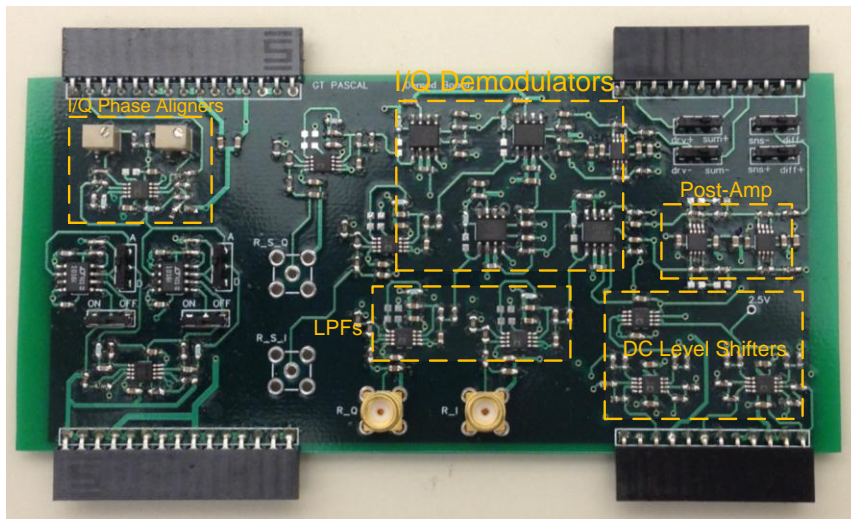
Figure 5.20: I/Q demodulator board receives the sense/difference signals and demodulates rate signal using the appropriate carrier with aligned phases. DC level shifters are used to adjust the DC offset to the 2.5V level required by the ADS1278 A/D backend.

structure, to be close to the main board, for efficient signaling. The power board, shown in Figure 5.21, is placed on the bottom of the structure to provide low-frequency reference voltages, MEMS polarization and tuning voltages, and electrical reference voltages. The low-frequency demodulated analog rate is also communicated to the ADC backend via the power board. The cubic PCB structure cannot be mechanically stabilized by only the header connectors. Therefore, fixtures are used at the back of the main and power boards to effectively align them and keep them firm.

The four boards are designed to operate from ±5V supply, which is provided by SF05D1205 from Delta Electronics, with 12VDC input and 500mA maximum output current capability. Each supply rail and ground potential are routed to each board via multiple header connectors, to guarantee sufficient current capability and low enough supply resistance and proper grounding all over the system. For safe operation of the power board, high-power resistors are used for ±5V supplies.

A 2.5V reference is provided by 2.5-V LTC6655 from Linear Technologies
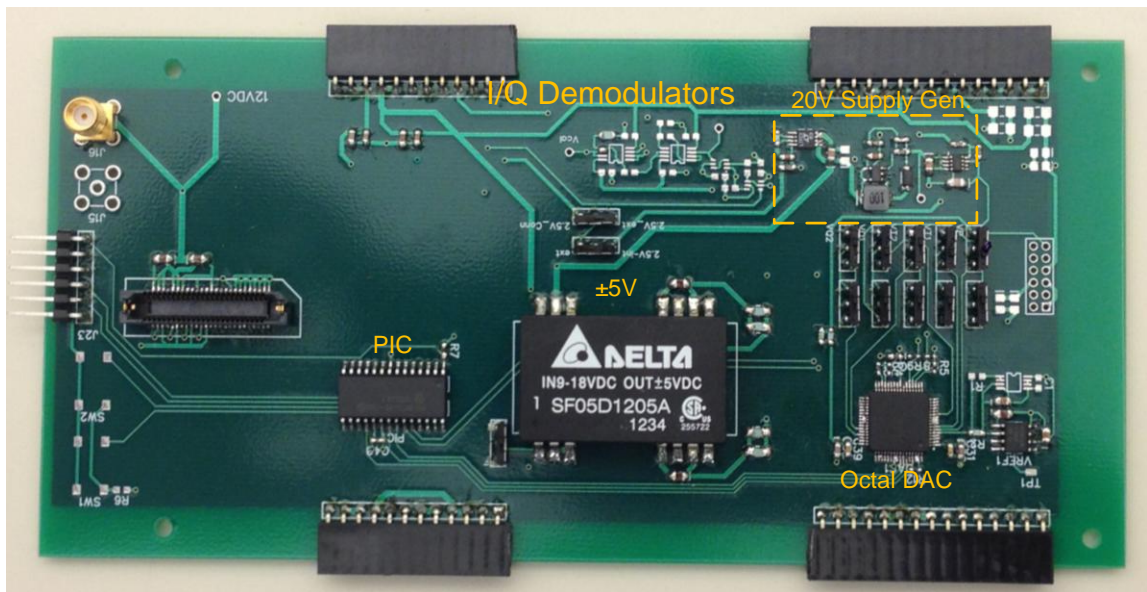
Figure 5.21: Power board generates the ±5V power supplies with 500mA maximum output current, and 2.5V and 5V reference voltages required for accurate operation of the analog circuitry. The MEMS bias voltages are provided by means of a 16-bit DAC that is supplied by a low-ripple low-noise 20V voltage generated on board from the 12VDC input.

(LTC), with 0.25ppm peak-to-peak averaged noise level, and 2 ppm/°C maximum temperature drift. This 2.5V reference guarantees low drift and high accuracy operation of analog circuits including the drive loop and its AGC, and the level shifters that condition the rate signal for the ADC backend.

To generate an 18V polarization voltage for the MEMS gyroscope, a DAC8718 IC from TI is used, which is an octal 16-bit DAC. The 20V supply of the DAC IC is provided by a chain of LT1615 step-up DC/DC converter followed by LT3007 which is a high-voltage low drop-out (LDO) regulator, both from Linear Technologies. The combination of the two power ICs provides a relatively low-noise 20V supply for the DAC operation. In addition to generating the 18V polarization voltage, this DAC also provides two frequency tuning voltages and two quadrature tuning voltages to the gyroscope. For accurate and stable operation of the gyroscope, the DAC requires a 5V reference voltage, which in this implementation is provided by a 5-V LTC6655. The operation of the DAC is controlled by a PIC microcontroller that can be programmed externally and can retain the DAC settings for consistency of turn-on to turn-on measurements of bias and scale factor.

5.3.6   Characterization Results

The self-contained self-calibrated gyroscope was characterized for bias performance and scale factor stability, with and without calibration. The same 1291Br Ideal Aerosmith rate table setup was used for these characterizations. Figure 5.22 shows the self-contained gyroscope system in the cube structure. Two 15-pin and 12-pin male-to-female header connectors are used on the sides of each board to the other by means of rectangular headers. To minimize feedthrough and capacitive/inductive coupling between signal traces, at least one ground pin is used in between each two pins that carry different signals, e.g. a ground pin exists between the pins that carry a difference signal and a summation signal, but no ground pin exists between two opposite-sign difference signals.
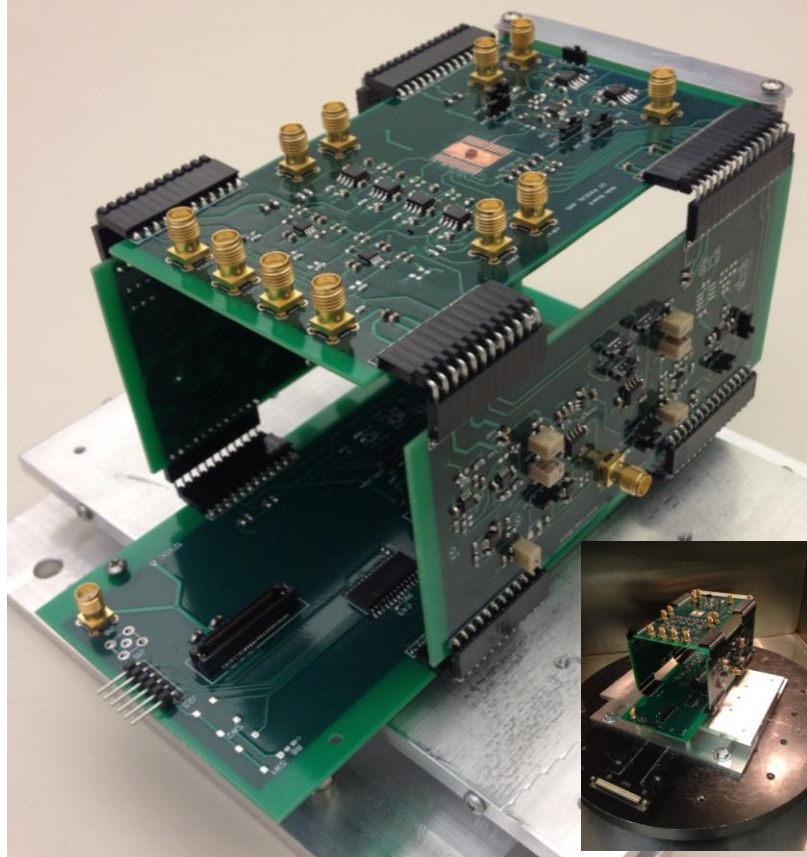
Figure 5.22: Self-contained self-calibrated gyroscope system; the cubic structure is comprised of a power board on the bottom, main board housing the device and actuation/sensing amplifiers on top, a closed-loop actuation board on the right side (front view), and a demodulator board on the left side (rear). The system is supplied by a 12-VDC 2A max input; rate output is digitized by ADC backend.

The bias cancellation capability of the dual-mode architecture was characterized on the self-contained setup, as shown in Figure 5.23, where Allan variance measurements are taken for 2 hours each, from the dual-mode configuration, the single-mode configuration, and from the in-phase demodulator multiplier output alone with its inputs grounded, to show both the advantages of dual-mode over single-mode in cancelling long-term bias drift components, and the effect of poor multiplier performance on the long-term bias instability of the system.

Comparison of the bias performances of the dual-mode and single-mode configurations shows 4-times reduction of bias drift from 140 °/hr at 200 sec in single-mode configuration, down to 35 °/hr at 600 sec in dual-mode configuration. Moreover,

the ARW is improved by 1.3 times due to the 3dB higher SNR of the dual-mode compared to the single-mode scheme. However, in comparison to the Allan variance plots of Figure 5.8, the bias instability values have increased by 5-6 times each, and the ARW values have increased by ~3-times each.

A stand-alone Allan variance characterization of the AD835 demodulating multiplier IC shows that the bias instability degradation of the dual-mode configuration compared to the dual-mode bias of Figure 5.8 can be majorly attributed to the poor temperature performance of bias of this multiplier, as also reported by the datasheet [71], i.e. up to ±25 mV offset drift with temperature. However, in the case of the single-mode configuration, poor offset behavior of the demodulator analog multiplier is expected to degrade the bias instability performance by only two times, due to the two-times lower gain of this configuration compared to the dual-mode configuration. The excess instability of the single-mode configuration can therefore be attributed to the demodulation of drive-loop phase noise by the ZRO of the sense output in this configuration, while the dual-mode output benefits from ~5-times lower ZRO amplitude,
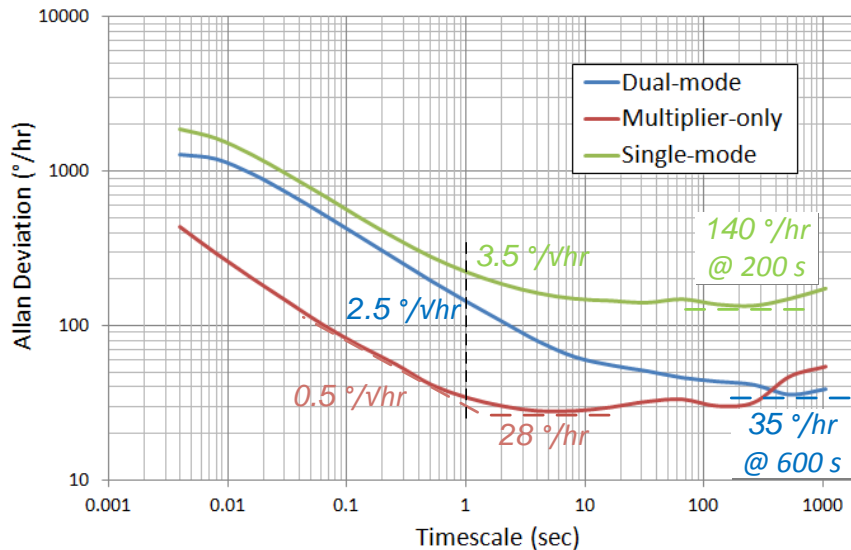

Figure 5.23: Allan variance measurements on the self-contained gyroscope system show 4X reduction of bias instability from 140 °/hr in single-mode configuration to 35°/hr in the dual-mode configuration. The multiplier output is also characterized for bias performance, causing significant degradation to the bias performances of both configurations.

121

similar to the ZRO plots of Figure 5.7. This is another important aspect of the advantages of bias cancellation in the dual-mode architecture compared to the single-mode scheme, which can reduce the amount of flicker noise demodulated from the drive-loop phase noise to the analog rate output.

The ARW is improved by 1.3-times by using the dual-mode scheme, due to its 3dB higher SNR compared to single-mode scheme. However, the ARW values have increased by ~3-times each, which is majorly caused by poor noise performance of the analog multiplication. In this regard, it should be noted that the multiplier-only output in the Allan variance plots of Figure 5.23, shows the bias performance of the multiplier output amplifier only, and not the noise performance of analog multiplier core, which is significantly noisier than the digital multiplier blocks within the lock-in amplifier unit.

It is also noteworthy that although the flicker noise performance of the multiplier is not reported in the datasheet, the early flattening of the multiplier-only Allan deviation plot indicates relatively large amounts of flicker noise in the post amplifier of the IC.

When used for coherent demodulation, the input and output offset drifts of AD835 multiplier ICs affect the bias performance of the gyroscope in the in-phase demodulator channel. In the quadrature-phase channel, these offset drifts translate into fake mode-split components, and thus result in mode-matching errors in an in-run mode-matching scheme. As a result, the self-contained gyroscope system has not been characterized for in-run mode-matching capability. Consequently, it is also preferred to stabilize the amplitude of the input forces, rather than the mode velocities, due to the absence of mode-matching scheme.

The scale factor drifts of the demodulating multipliers have almost no impact on the performance of online scale factor calibration, since both rates see the same demodulation path. Moreover, in an in-run mode-matching loop, the drifts of scale factor can only change the gain of the control loop, without any impact on its accuracy performance. The complications that multipliers offset and offset drifts create for self-

calibrated gyroscope implementation, call for offset reduction techniques, or alternatively for all-digital implementations of the scheme, where the digital multipliers show zero drift in their offset and scale factor performances.

In order to characterize the scale factor stability improvement, both mechanical and electrical scale factor values are measured every day for 7 consecutive days, where the system is turned off at the end of each measurement, and turned back on the next day for the new measurement. Using the electrical scale factor measured each day, the calibrated mechanical scale factor is calculated from the raw mechanical scale factor value as described below:

$$SF_{Phy,calibrated,n} = SF_{elec,1} \frac{SF_{Phy,n}}{SF_{elec,n}} \ , \tag{5.15}$$

where $SF_{Phy,calibrated,n}$ is the calibrated mechanical scale factor of the nth day, $SF_{Phy,n}$ is the raw mechanical scale factor measured on the nth day, $SF_{elec,n}$ is the raw electrical scale factor measured on the nth day, and $SF_{elec,1}$ is the baseline electrical scale factor measured on the 1st day.

The combination of sinusoidal mechanical rate and square-wave electrical rate can be practically used for online background calibration of scale factor. However, for maximum measurement accuracy and consistency, it is preferred that both rates be sinusoidal, at different frequencies. With sinusoidal rotation and calibration rates, an FFT algorithm can be used to characterize the output signal peaks in frequency domain, and consequently reject the effect of time-varying offset on peak-to-peak or root-mean-square (RMS) measurements.

Figure 5.24 shows the response of the dual-mode self-calibrated gyroscope to simultaneous application of sinusoidal mechanical and electrical rates at two different frequencies. In order to avoid the leakage of each rate tone from its corresponding FFT

bin into its side bins, the frequency of each rate should be selected, as accurately as possible, at one of the 2^N available FFT bins, defined as:

$$f_{in} = \frac{M}{2^N} f_{sampling} \tag{5.16}$$

where $f_{sampling}$ is the sampling frequency of 1kHz, provided by the data acquisition backend, N is the number of FFT bits, M is an integer number smaller than 2^N, and f_{in} is the frequency of the input rate. In order to utilize the entire dynamic range offered by a 2^N-point FFT, M is typically selected to be an integer that is co-prime to 2^N. This will guarantee that each two samples used by the FFT algorithm will have different voltage levels, and therefore the full dynamic range offered by the FFT algorithm will be utilized.

In order to avoid interference of the two modes or their harmonics with each other, the two input frequencies have to be far enough from each other and also from each other's harmonics. Based on the above assumptions, the frequencies of the physical rate and electrical rate are selected to be at bin-63 and bin-223 of the 2^{16}-point FFT as:
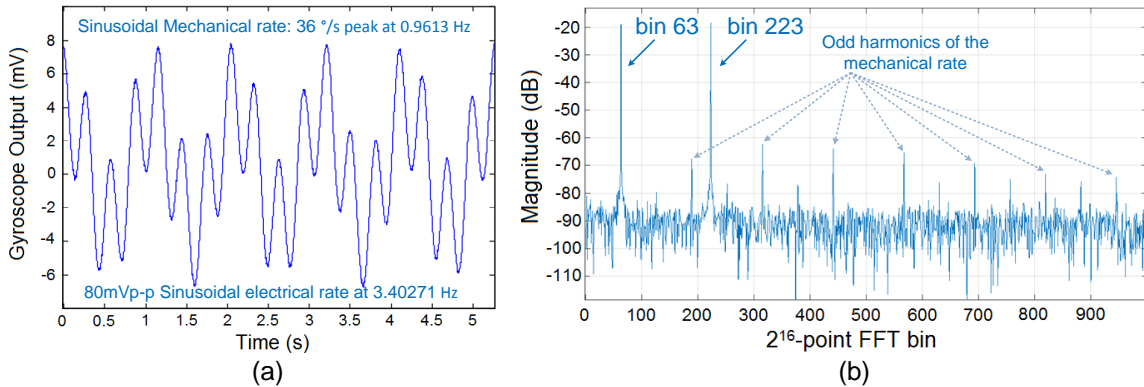
Figure 5.24: Simultaneous application of sinusoidal mechanical rate with 36 °/s peak amplitude, at 0.9613 Hz frequency, and sinusoidal electrical rate with 80 mV$_{pk-pk}$ (equivalent to ~39 °/s peak) amplitude, at 3.40271 Hz frequency (a) time-domain waveform, and (b) frequency-domain spectrum; the two rate are applied at two different frequencies. The frequencies are chosen to be at the 63rd and 223rd bins of a 2^{16}-point FFT at a sampling rate of 1 kHz. Mechanical rate exhibits nonlinear behavior, as seen from its many higher order odd harmonics, unlike the electrical rate which shows no significant harmonics. Since the output is the superposition of the two applied rates, the output does not show any intermodulation of the two input rate tones.

$$f_{in,Phy} = \frac{2^6 - 1}{2^{16}} 1000 = 0.9613 \, Hz$$

$$f_{in,Cal} = \frac{2^8 - 2^5 - 1}{2^{16}} 1000 = 3.40271 \, Hz \tag{5.17}$$

which are not even close to an integer ratio of one another. The accuracy of the rate table frequency is as good as 100µHz, which is sufficient for a 22-bit FFT using the 1-kHz sampling rate of the data acquisition back-end. In order to provide 36 °/s peak rotation rate, the angular amplitude of the rate table is set to 5.9602°. The amplitude of the electrical stimulus is also chosen to be 80 mV$_{pk\text{-}pk}$, equivalent to ~39 °/s peak.

Figure 5.24a shows a ~5sec frame of the time-domain response of the system to simultaneous mechanical and electrical virtual rotations. Figure 5.24b shows the discrete frequency-domain response of the system to both rates. As can be seen, the mechanical rate shows up to 15 harmonics, while the electrical calibration rate does not show any significant harmonics. Moreover, no intermodulation of the two rates is observed in the output, which is a clear indication that the harmonics of the mechanical rate are created by nonlinearity of the rate table, as the gyroscope is operating linearly in presence of
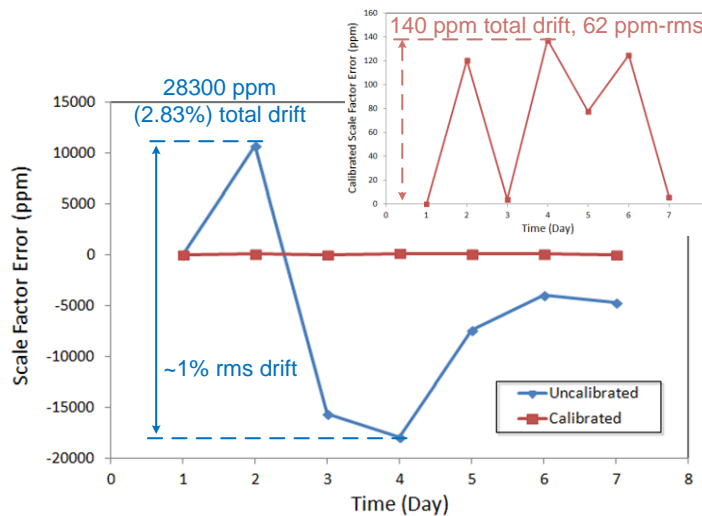
Figure 5.25: Scale factor of the system has been measured for 7 consecutive days; the uncalibrated scale factor shows an overall drift of 2.83%, equivalent to ~1% RMS drift over 7 days. When calibrated by the electrical rate scale factor, the overall drift of scale factor reduces to 140ppm, equivalent to 62 ppm RMS drift, which is 150× reduction of scale factor drift.

125

simultaneous 36 °/s mechanical and 39 °/s electrical rates.

Figure 5.25 shows the drift performance of the uncompensated scale factor and that of the compensated scale factor on the same plot, measured for 7 consecutive days. As can be seen, the uncalibrated dual-mode scheme shows an overall scale factor drift of 2.83%, and an RMS drift of ~1%. By using the self-calibration algorithm described in (5.15), the RMS drift is improved by ~150 times down to 62 ppm, while the peak-to-peak drift is improved by ~200 times down to 140 ppm.

CHAPTER 6

CONCLUSIONS AND FUTURE WORK

In this dissertation, system architectures were introduced for readout, control and self-calibration of MEMS resonators and resonant gyroscopes. The presented characterization results clearly indicate the enabling features of the proposed architectures, and their advantages in terms of noise, linearity, and long-term drift performance of the interface system. This chapter presents a summary of the contributions of this research, followed by future directions towards near-zero-drift performances in MEMS resonant gyroscopes.

6.1   CONTRIBUTIONS

A summary of the technical contributions made throughout the course of this study is provided below:

1) An electromechanical feedback technique was proposed to provide linear bidirectional active frequency tuning to piezoelectric-on-Si MEMS resonators and resonant sensors. The linearity and tuning range were studied thoroughly and the effects of nonidealities were also explored. The characterization results were shown to prove the efficacy of the proposed scheme.

2) The active frequency tuning scheme was used to enable for the first time, implementation of mode-matched piezoelectric-on-Si resonant gyroscopes, with high dynamic range and high sensitivity performance.

3) A dual-mode actuation and differential readout scheme was proposed for axisymmetric MEMS resonant gyroscopes. The dual-mode differential readout scheme provides inherent cancellation of mode coupling terms in the gyroscope system equations, thus improves the bias performance over that of the conventional single-mode actuation schemes.

4) The differential sensing scheme provides a mode-split indicator signal that is independent of the applied rotation. An in-run mode-matching scheme was implemented that nulls this mode-split indicator to maintain mode-matched condition at all times. The dual-mode readout scheme shows two orders of magnitude reduction of the drift of gyroscope bias over temperature, as compared to conventional uncompensated single-mode scheme.

5) A scale factor calibration scheme was proposed that applies a virtual rotation to the gyroscope. The response of the gyroscope to the virtual rotation can be used to estimate the drifts of scale factor over time and temperature, and compensate for them. In the proposed scheme, the gyroscope rotation input is a linear combination of the virtual and physical rotations. Therefore, simultaneous application of the two is possible for online calibration of scale factor errors. Moreover, the linearity of the transfer function avoids intermodulation of the two rates. The proposed scale factor calibration scheme shows up to two orders of magnitude reduction in the long-term drifts of scale factor.

6.2   ERROR SOURCES AND NONIDEALITIES

The stability performance of bias and scale factor of the dual-mode gyroscope scheme can be affected by mismatches between gyroscope modes or mismatches in the gains of electrical actuation and sensing paths. For instance, quality factor mismatches in the gyroscope can significantly increase the output bias, depending on the amount of mismatch. In a similar manner, resistor mismatches in the dual-mode TIA front-end can result in the degradation of bias cancellation. To achieve high accuracy using the dual-mode architecture, a thorough analysis of these sources of mismatch and nonidealities is required. An intuitive analysis of the electronics errors was provided in section 5.3.6. In this section, the effects of quality factor mismatch and substrate anisotropy on bias calibration performance are discussed.

6.2.1 Quality Factor Mismatch of Gyroscope Modes

In the presence of quality factor mismatches, (5.1) can be rewritten as:

$$
\begin{bmatrix}
\omega_x^2 - \omega_0^2 + j\dfrac{\omega_0\omega_x}{Q_x} & j2\lambda\Omega_z\omega_0 \\[2ex]
-j2\lambda\Omega_z\omega_0 & \omega_y^2 - \omega_0^2 + j\dfrac{\omega_0\omega_y}{Q_y}
\end{bmatrix}
\cdot
\begin{bmatrix}
X(j\omega_0) \\[2ex]
Y(j\omega_0)
\end{bmatrix}
=
\begin{bmatrix}
F_x(j\omega_0)/m \\[2ex]
F_y(j\omega_0)/m
\end{bmatrix}
\tag{6.1}
$$

where Q_x and Q_y are the x-mode and y-mode quality factors, respectively. It is assumed for an axisymmetric gyroscope that the two quality factor values are almost equal. Therefore, the assumption that $f_{lock}=f_0$ is still valid. The equation (6.1) can be solved as:

$$
X_{Sum}(j\omega_0) \approx -\frac{1}{m\omega_0}\frac{j\left(\dfrac{\omega_0}{Q_x}F_y + \dfrac{\omega_0}{Q_y}F_x\right) + j2\lambda\Omega_z\left(F_x - F_y\right)}{(\Delta\omega)^2 + \dfrac{\omega_0}{Q_x}\cdot\dfrac{\omega_0}{Q_y} + \left(2\lambda\Omega_z\right)^2 + j\omega_0\Delta\omega\left(\dfrac{1}{Q_x} - \dfrac{1}{Q_y}\right)}
$$

$$
X_{Diff}(j\omega_0) \approx -\frac{1}{m\omega_0}\frac{\Delta\omega\times\left(F_x + F_y\right) + j\left[\dfrac{\omega_y}{Q_y}F_x - \dfrac{\omega_x}{Q_x}F_y + 2\lambda\Omega_z\left(F_x + F_y\right)\right]}{(\Delta\omega)^2 + \dfrac{\omega_0}{Q_x}\cdot\dfrac{\omega_0}{Q_y} + \left(2\lambda\Omega_z\right)^2 + j\omega_0\Delta\omega\left(\dfrac{1}{Q_x} - \dfrac{1}{Q_y}\right)}.
\tag{6.2}
$$

In both (6.1) and (6.2), the input actuating forces, F_x and F_y, are also considered to be different, to be able to compensate for the quality factor mismatch.

As can be seen, the quality factor mismatch generates an additional ZRO term that is in-phase with the Coriolis component, in the difference output. This in-phase relationship makes it difficult to distinguish this ZRO term from the mechanical rotation rate. However, it can also be understood from (6.2) that if F_x and F_y can be adjusted such that $Q_xF_x=Q_yF_y$, then the additional ZRO term can be nulled.

This can also be understood by looking into the individual mode outputs, at mode-matched condition (for simplicity):

$$X\left(j\omega_0\right) \approx -\frac{1}{m\omega_0} \frac{j\dfrac{\omega_0}{Q_y}F_x + j2\lambda\Omega_z F_y}{\dfrac{\omega_0}{Q_x}\cdot\dfrac{\omega_0}{Q_y}+\left(2\lambda\Omega_z\right)^2}$$

$$Y\left(j\omega_0\right) \approx -\frac{1}{m\omega_0} \frac{j\dfrac{\omega_0}{Q_x}F_y - j2\lambda\Omega_z F_x}{\dfrac{\omega_0}{Q_x}\cdot\dfrac{\omega_0}{Q_y}+\left(2\lambda\Omega_z\right)^2}. \tag{6.3}$$

In a stationary gyroscope, at mode-matched condition, in order to adjust F_x and F_y to provide the $Q_x F_x = Q_y F_y$ condition, two independent VGAs can be used to stabilize the individual mode velocities to a single desired reference level, V_{ref}, while the drive loop still locks to the phase zero-crossing of the sum transfer function, to minimize the effect of rotation on the phase of the drive loop. However, when rotation is applied, the two individual output displacements change in opposite directions as a result of differential Coriolis force. Consequently, the two individual VGAs will also compensate for the differential Coriolis-induced displacement in the individual mode outputs, resulting in reduction of the Coriolis sensitivity to zero, and also leakage of quadrature and in-phase ZRO terms to the difference output due to the imbalanced input forces. Therefore, the most straightforward way to alleviate this issue is to characterize the Q-mismatch of the gyroscope modes individually, and apply their ratio to the VGA gains to control the gyroscope actuation, with the fair assumption that the ratio of the quality factors will remain the same over temperature and time, at least in an isotropic axisymmetric gyroscope structure.

It can be understood from (6.2) that in the presence of quality factor mismatch, the frequency split between the modes can still be monitored through the quadrature-phase component of the difference output. Since the ultimate goal is to null this mode-split entirely, the stability or accuracy of the coefficient of mode-split indicator is not

important. Therefore, an in-run mode-matching scheme similar to the one presented in Figure 5.4 can still be used to maintain mode-matched condition.

An alternative way to reduce the effect of applied rotation on the transfer function of the system is to use force-to-rebalance to compensate for the Coriolis terms in the individual mode outputs, as shown in the schematic of Figure 6.1. However, it can be shown that in such a scheme, the force-to-rebalance loop also compensates for the Q-mismatch, due to the differential nature of this mismatch.

In the force-to-rebalance architecture the individual mode outputs are as follows:

$$
X(j\omega_0) \approx -\frac{1}{m\omega_0} \frac{j\dfrac{\omega_0}{Q_y}F_x + j\left(2\lambda\Omega_z + \dfrac{\eta^2 R_F V_{cal}}{m}\right)F_y}{\dfrac{\omega_0}{Q_x}\cdot\dfrac{\omega_0}{Q_y} + \left(2\lambda\Omega_z + \dfrac{\eta^2 R_F V_{cal}}{m}\right)^2}
$$

$$
Y(j\omega_0) \approx -\frac{1}{m\omega_0} \frac{j\dfrac{\omega_0}{Q_x}F_y - j\left(2\lambda\Omega_z + \dfrac{\eta^2 R_F V_{cal}}{m}\right)F_x}{\dfrac{\omega_0}{Q_x}\cdot\dfrac{\omega_0}{Q_y} + \left(2\lambda\Omega_z + \dfrac{\eta^2 R_F V_{cal}}{m}\right)^2}. \tag{6.4}
$$
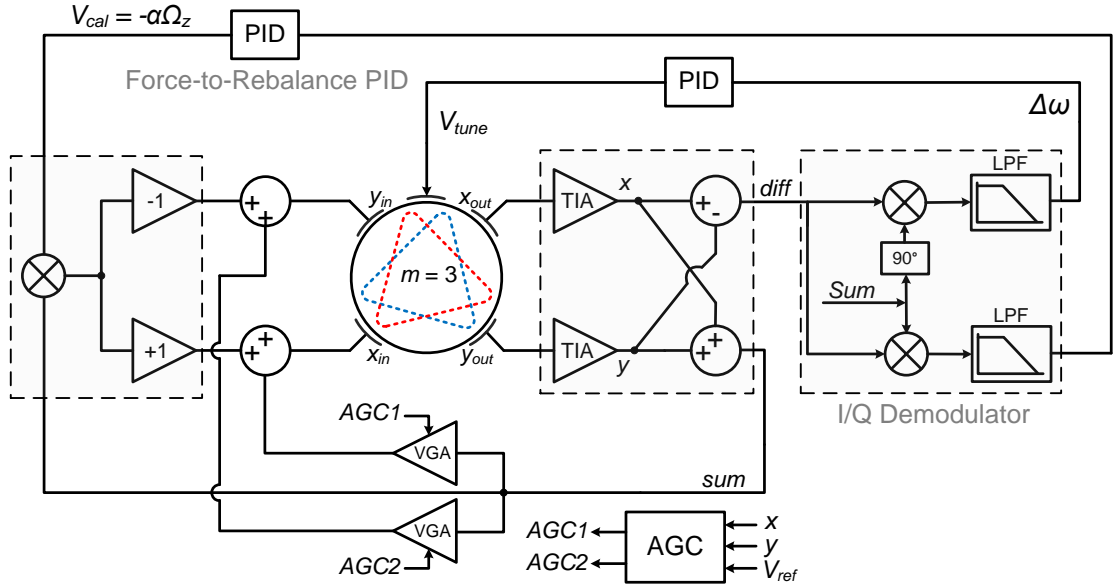
Figure 6.1: Force-to-rebalance architecture used to interface a Q-mismatched gyroscope.

Therefore, V_{cal} can be derived as:

$$V_{cal} = \frac{m}{\eta^2 R_F}\left(-2\lambda\Omega_z + \frac{\omega_0}{F_x + F_y}\left(\frac{F_y}{Q_x} - \frac{F_x}{Q_y}\right)\right),$$ (6.5)

where the Q-mismatch dependency of V_{cal} is controlled by the $Q_x F_x = Q_y F_y$ condition, while the mechanical rate component is independent of the applied actuation forces. With the V_{cal} force applied, the individual mode output will be:

$$X(j\omega_0) = Y(j\omega_0) = -\frac{1}{m\omega_0}\frac{j\dfrac{\omega_0}{F_x + F_y}\left(\dfrac{F_x^{\,2}}{Q_y} + \dfrac{F_y^{\,2}}{Q_x}\right)}{\dfrac{\omega_0}{Q_x}\cdot\dfrac{\omega_0}{Q_y} + \left(\dfrac{\omega_0}{F_x + F_y}\right)^2\left(\dfrac{F_y}{Q_x} - \dfrac{F_x}{Q_y}\right)^2},$$ (6.6)

which are equal in amplitude, due to the nulling of the in-phase difference output.

It can be understood from both (6.2) and (6.5) that the Q-mismatch-induced ZRO is proportional to the difference of gyroscope bandwidths in both open-loop and force-to-rebalance architecture, implying that larger quality factor values, thus smaller bandwidth values, can significantly improve this in-phase ZRO, even in the presence of mismatches. In such a condition, the force-to-rebalance architecture has the added advantage of retrieving bandwidth by closed-loop feedback, while the bias is still reduced by the large values of the open-loop gyroscope quality factor values.

In the scheme of Figure 6.1, since both individual velocities and thus the sum velocity are fixed to a voltage reference, only one multiplier is required to generate the single-ended calibration signal. A subsequent single-to-differential amplifier will change the polarity of the calibration signal to be applied to individual modes. This will eliminate the effect of multiplier scale factor and offset mismatches in the scheme of Figure 5.11.

It can be shown that for unequal actuation forces, the quadrature and damping coupling terms leak into the difference output. The amount of leakage is proportional to

the difference of the two forces, $\Delta F = F_x - F_y$. Therefore, the force difference required to compensate for the Q-mismatch in dual-mode scheme, results in $\sim Q$-times lower magnitude of the coupling terms than their actual contribution to the individual modes.

6.2.2   Effect of Anisotropy

As mentioned earlier, the dual-mode scheme is mostly suitable for axisymmetric gyroscope structures. Ideally, an axisymmetric gyroscope fabricated on an isotropic substrate can benefit from near-complete cancellation of bias errors.

In a dual-mode interface that uses such an anisotropic gyroscope, the placement of electrodes becomes a more critical issue. Unequal displacements at different antinodes of the two modes can result in insertion loss mismatch between the two modes, depending on the device structure and the electrode configuration. In an isotropic device, the quality factor mismatch can be compensated by using the scheme described in Figure 6.1. However, in an anisotropic device, the insertion loss mismatch is not only caused by quality factor mismatch. Instead, it may include the asymmetric couplings of each mode on the other due to anisotropy, resulting in miscalculation of the actual insertion losses of the modes. Consequently, compensation of the insertion loss mismatch in such conditions can result in further increase of the mismatch, thus degrade the drift of bias.

6.3   BENCHMARKING AND COMPARISON

Table II shows a comparison of the performance achieved in this work, with commercially available high performance gyroscopes [73]-[76], and the FM gyroscope published in [65]. The comparison takes into account parameters such as the noise performance or ARW, sensitivity, full-scale range, long-term stability and temperature stability of both bias and sensitivity, and their bandwidths.

While some of the parameters are not specified (N/S) for some of the gyroscopes, most relevant parameters are listed in this comparison. It can be understood from Table II

that the self-calibrated dual-mode scheme provides the lowest temperature stability of scale factor, i.e. 0.35% over [10-50] °C temperature range, and also the lowest bias instability, i.e. 5.4 °/hr. Moreover, the bias and scale factor repeatability provided by the self-calibrated dual-mode scheme, i.e. 21 ppmFS and 60 ppm respectively, are among the lowest numbers reported in Table II. Although the FM gyroscope in [65] shows an order of magnitude better scale factor stability than this work, the ARW performance is compromised due to the inherently low gain of frequency-output sensors.

The comparison of Table II clearly shows the advantages of the dual-mode scheme in minimizing the temperature drift of both scale factor and bias and improving their repeatability over time. This makes the dual-mode scheme a preferred architecture for high-end applications where stable gyroscope operation is required.

Table II: Performance comparison between commercially available and academically published gyroscopes and the dual-mode self-calibrated gyroscope system.

Performance Metric	Unit	BMG160 [73]	CRS43-04 [74]	QGYR110Hx [75]	ADXRS646 [76]	[65]	This work
Scale Factor (*SF*)	mV/°/s	0.34 - 5.5	10	0.25 - 4	9	N/A	0.044
Angle Random Walk	°/√hr	0.84	1.2	0.42	0.6	3.3	0.7
Bias instability	°/hr	N/S	N/S	14	12	6	5.4
Full scale range	°/s	125 - 2000	200	±300 - 3000	±300	±1000	±3000
Bandwidth	Hz	12 - 230	25	N/S	1000	50	35
Temp. drift of *SF*	ppm/°C	300	--	N/S	--	--	--
SF variation over temp. range	%	--	±3	N/S	±6.5	N/S	0.35*
Temp. drift of bias	°/s/°C	±0.015	--	±0.05	--	N/S	--
Bias variation over temp. range	°/s	--	±6	--	±3	N/S	±1.5
Bias repeatability	ppmFS	--	--	--	--	--	21
Bias tolerance	°/s	±1	±6	±5	N/S	--	--
SF tolerance	%	±1	N/S	±3	N/S	0.0007	0.006
Temperature Range	°C	[-40, 85]	[-40, 85]	[-40, 85]	[+20, 105]	N/S	[10, 80]

* measured in a temperature range of [10, 50] °C; this drift is equivalent to 88 ppm/°C.

6.4 FUTURE WORK

The dual-mode architecture provides the basic means to minimize the drift of bias and scale factor in axisymmetric resonant MEMS gyroscopes. Different types of nonidealities were introduced throughout Chapter 5 that can affect the performance of both bias compensation and scale factor calibration schemes. A list of these error sources, their impact on the system performance, and potential solutions to mitigate their effects are brought below:

1) The mismatches in gain and offset of different analog electronic components can induce offset or gain inaccuracies in the overall performance of the dual-mode self-calibrated gyroscope scheme:

   a. The input offset of the calibration multipliers induce DC virtual rotation in the gyroscope transfer function, which appears as bias at the sensor output; the variations of this offset will therefore translate into drift of bias over time and environmental variations.

   b. Gain mismatches between the two calibration multipliers can induce errors in the scale factor calibration performance. The variations of these gains with time and temperature can result in further drift of scale factor.

   c. The mismatch of the resistor networks used in the TIA front-end and analog summing amplifiers can result in incomplete cancellation of the mode coupling terms, thus cause bias leakage into the system output.

   d. The drift of the input offset and output offset of the demodulating multipliers result in degradation of the overall bias performance. However, since both physical and calibration rate outputs see the same multiplier gain, the drift of that gain does not affect the scale factor calibration accuracy.

   In order to alleviate the abovementioned drift issues due to inaccuracies and mismatches in gains and offsets of the analog electronics, an all-digital

135

implementation must be used, where the TIA outputs are digitized by high-precision ADCs, the digitized samples are processed by high-speed FPGA and DSP electronics. Based on the processor results, using high-speed DACs, proper analog signals are generated to actuate the gyroscope modes. In such a scheme, the offset and gain inaccuracy of the mathematical operations inside the digital processor are virtually zero, and at the same time, the offsets and gain inaccuracies of the TIAs and ADC/DAC channels can be background-calibrated by the digital processing unit. The choice of data converter architecture and precision depends on the frequency range of the resonant gyroscope device, and the overall required dynamic range of the system.

2) The existence of uncompensated quadrature coupling between the gyroscope modes can result in frequency shift of the actuation drive loop, thus result in leakage of rate and mode-split outputs into each other, as discussed in section 5.1.2. This can complicate the operation of in-run mode-matching as well as the general rate readout in the dual-mode gyroscope interface system. A simple fix to this issue in the open-loop architecture, is by monitoring the leakage of virtual rotation of a specific frequency into the quadrature-phase channel (mode-split indicator channel) of the coherent I/Q demodulator, and compensating for the error by incorporating a phase shifter into the demodulator. This can be done by mixing the mode-split output into the applied virtual rotation stimulus, and nulling its DC component by controlling the demodulator phase shift.

3) Automatic initial alignment and matching of the gyroscope is required in a self-sufficient gyroscope scheme. An algorithm needs to be devised based on the discussions and simulation results of section 5.1.3, to utilize the asymmetry of the gyroscope sum output response in presence of both mode-split and quadrature coupling, for initial alignment and frequency matching of the gyroscope modes,

automatically. Following this initialization, the in-run mode-matching scheme presented in section 5.1.3 can maintain mode-matched condition.

4) Symmetry of the gyroscope structure is crucial to the performance of the dual-mode architecture. While the dual-mode scheme, due to its differential sensing nature, allows monitoring of several mismatch errors in the gyroscope, it cannot detect or cancel the asymmetric coupling effects that are caused by the substrate anisotropy. Therefore, the use of an axisymmetric gyroscope fabricated on an isotropic material substrate is highly recommended to achieve the best performance from the dual-mode architecture.

5) As discussed in section 6.2.1, quality factor mismatches between the gyroscope modes can induce significant errors into the bias, in the dual-mode gyroscope architecture. The proposed architecture of Figure 6.1 should be used in a sophisticated implementation to cancel out the effect of rotation by a force-to-rebalance control loop, and at the same time maintain control of the individual output amplitudes by individual VGAs that can compensate for the mismatch of quality factor values. This will be the most challenging item in the future implementation of the dual-mode gyroscope towards achieving zero-drift gyroscope systems.

In conclusion, an all-digital FPGA-based implementation of the dual-mode architecture, using an isotropic gyroscope, has potentials to provide near-zero-drift performance in terms of both gyroscope bias and scale factor, by maintaining control of different gyroscope parameters that can change over time and temperature, by means of multiple concurrently-running control loops. With such an implementation, the bottleneck of accuracy and drift can ultimately be limited to that of the available analog voltage reference technology.

REFERENCES

[1] N. Yazdi, F. Ayazi, and K. Najafi, "Micromachined inertial sensors," *Proc. IEEE*, vol. 86, no. 8, pp. 1640–1659, Aug. 1998.

[2] M.S. Weinberg and A. Kourepenis, "Error sources in in-plane silicon tuning fork MEMS gyroscopes," *Microelectromechanical Systems, Journal of,* vol. 15, no. 3, pp. 479–491, Jun. 2006.

[3] IEEE Standard Specification Format Guide and Test Procedure for Single-Axis Interferometric Fiber Optic Gyros," *IEEE Standard 952-1997*, 1998 doi: 10.1109/IEEESTD.1998.86153S.

[4] Farrokh Ayazi, "A High Aspect-ratio High Performance Polysilicon Vibrating Ring Gyroscope," Ph.D. dissertation, University of Michigan, 2000.

[5] M.F. Zaman, A. Sharma, Z. Hao, and F. Ayazi, "A Mode-matched Silicon Yaw Tuning-Fork Gyroscope with Subdegree-per-hour Allan Deviation Bias Instability," *Microelectromechanical Systems, Journal of,* vol. 17, pp. 1526-1536, 2008.

[6] F. Ayazi, "Multi-DOF inertial MEMS: From gaming to dead reckoning," Solid-State Sensors, Actuators and Microsystems Conference (TRANSDUCERS), 2011 16th International, pp. 2805-2808, 5-9 June 2011.

[7] S. Sung, W. T. Sung, C. Kim, S. Yun, Y. J. Lee, "On the Mode-Matched Control of MEMS Vibratory Gyroscope via Phase-Domain Analysis and Design," *Mechatronics, IEEE/ASME Transactions on* , vol.14, no.4, pp.446,455, Aug. 2009.

[8] M. Saukoski, L. Aaltonen, and K.A.I. Halonen, "Zero-Rate Output and Quadrature Compensation in Vibratory MEMS Gyroscopes," *IEEE Sensors Journal*, vol. 7, no. 12, pp. 1639-1652, Dec. 2007.

[9] E. Tatar, S. E. Alper, T. Akin, "Effect of Quadrature Error on the Performance of a Fully-Decoupled MEMS Gyroscopes," *Proc. IEEE, MEMS 2011,* pp. 569-572, Jan. 2011.

[10] A.S. Phani, A.A. Seshia, M. Palaniapan, R.T. Howe, and J.A. Yasaitis, "Modal coupling in micromechanical vibratory rate gyroscopes," *IEEE Sensors Journal*, vol. 6, no. 5, pp. 1144–1152, Oct. 2006.

[11] H. Xie and G.K. Fedder, "Integrated Micro-electromechanical Gyroscopes," *Journal of Aerospace Engineering (ASCE)*, vol. 16, no. 2, pp. 65–75, Apr. 2003.

[12] A. Sharma, M. Zaman, and F. Ayazi, "A 104-dB dynamic range transimpedance-based CMOS ASIC for Tuning Fork Microgyroscopes," *Solid-State Circuits, IEEE Journal of* , vol. 42, no. 8, pp. 1790-1802, Aug. 2007.

[13] M.F. Zaman, "Degree-per-hour mode-matched micromachined silicon vibratory gyroscopes," Ph.D. dissertation, Georgia Institute of Technology, April 2008.

[14] A. Sharma, M.F. Zaman, and F. Ayazi, "A Sub-0.2 °/hr Bias Drift Micromechanical Gyroscope with Automatic CMOS Mode-Matching," *IEEE Journal of Solid-State Circuits (JSSC)*, Vol. 44, No.5, pp. 1593-1608, May 2009.

[15] A. N.Shirazi, M.F. Zaman, and F. Ayazi, "A Digital Phase Demodulation Technique for Resonant MEMS Gyroscopes," *IEEE Sensors Journal*, vol. 14, Issue 9, 2014, pp.3260-3266.

[16] D. Allan, "Statistics of atomic frequency standards," *Proceedings of the IEEE*, vol. 54, no. 2, pp. 221-230, Feb. 1966.

[17] "IEEE standard for inertial sensor terminology," IEEE, Aug. 2001.

[18] "IEEE Standard Specification Format Guide and Test Procedure for Coriolis Vibratory Gyroscopes," IEEE, Jan. 2004.

[19] L.C. Ng, "On the Application of Allan Variance Method for Ring Laser Gyroscope Performance Characterization," No. UCRL-ID-115695, Lawrence Livermore National Lab., CA (United States), 1993.

[20] B.J. Gallacher, J. Hedley, J.S. Burdess, A.J. Harris, A. Rickard, and D.O. King, "Electrostatic Correction of Structural Imperfections Present in a Microring Gyroscope," *Journal of Microelectromechanical Systems (JMEMS)*, vol. 14, no. 2, pp. 221–234, Apr. 2005.

[21] David M. Rozelle, "Self Calibrating Gyroscope System," U.S. Patent No. 7,912,664, Mar 22, 2011.

[22] I.P. Prikhodko et al, "In-run Bias Self-calibration for Low-cost MEMS Vibratory Gyroscopes," *PLANS 2014*, pp.515-518, 5-8 May 2014.

[23] R. Antonello, R. Oboe, L. Prandi, F. Biganzoli, "Automatic Mode Matching in MEMS Vibrating Gyroscopes Using Extremum-Seeking Control," *Industrial Electronics, IEEE Transactions on* , vol.56, no.10, pp.3880,3891, Oct. 2009.

[24] C. D. Ezekwe, B. E. Boser, "A Mode-Matching $\Sigma\Delta$ Closed-Loop Vibratory Gyroscope Readout Interface With a 0.004 /s/ √Hz Noise Floor Over a 50 Hz Band," *Solid-State Circuits, IEEE Journal of* , vol.43, no.12, pp.3039,3048, Dec. 2008.

[25] S. Sonmezoglu, S. E. Alper, T. Akin, "An automatically mode-matched MEMS gyroscope with 50 Hz bandwidth," *Micro Electro Mechanical Systems (MEMS), 2012 IEEE 25th International Conference on*, pp.523,526, Jan. 29 2012-Feb. 2 2012.

[26] G.K. Balachandran, V.P. Petkov, T. Mayer, T. Baislink, "27.1 A 3-Axis gyroscope for electronic stability control with continuous self-test," in *Solid- State Circuits Conference - (ISSCC), 2015 IEEE International*, pp.1-3, 22-26 Feb. 2015.

[27] J. Seeger, M. Lim, and S. Nasiri, "Development of High-Performance, High-Volume Consumer MEMS Gyroscopes," In *Technical Digest Solid-State Sensor, Actuator and Microsystems Workshop, Hilton Head Island* (2010), (pp. 61-64).

[28] L. Prandi, C. Caminada, L. Coronato, G. Cazzaniga, F. Biganzoli, R. Antonello, R. Oboe, "A low-power 3-axis digital-output MEMS gyroscope with single drive and multiplexed angular rate readout," *Solid-State Circuits Conference Digest of Technical Papers (ISSCC), 2011 IEEE International*, pp.104,106, 20-24 Feb. 2011.

[29] J.A. Geen, S.J. Sherman, J.F. Chang, and S.R. Lewis, "Single-Chip Surface Micromachined   Integrated Gyroscope with 50°/h Allan Deviation," *Solid-State Circuits*, *IEEE Journal of,* vol. 37, no. 12, pp. 1860-1866, Dec. 2002.

[30] G. Casinovi, W. K. Sung, M. Dalal, A. N.-Shirazi, F. Ayazi, "Electrostatic Self-calibration of Vibratory Gyroscopes," *Micro Electro Mechanical Systems (MEMS), 2012 IEEE 25th International Conference on*, pp.559,562, Jan 29-Feb 2, 2012.

[31] A. Norouzpour-Shirazi, G. Casinovi, M. Dalal, and F. Ayazi, "Combined Phase-readout and Self-calibration of MEMS Gyroscopes," *Solid-State Sensors, Actuators and Microsystems,2013 Transducers & Eurosensors XXVII: The 17th International Conference on*, pp.960-963, 16-20 June 2013.

[32] M.H. Kline, Y. Yeh, B. Eminoglu, H. Najar, M. Daneman, D. A. Horsley, B. E. Boser, "Quadrature FM gyroscope," *Micro Electro Mechanical Systems (MEMS), 2013 IEEE 26th International Conference on*, pp.604,608, 20-24 Jan. 2013.

[33] B. Eminoglu, M.H. Kline, I. Izyumin, Y. Yeh, and B.E. Boser, "Ratiometric Readout Technique for MEMS Gyroscopes with Force Feedback," in *Proc. IEEE/ION Position Location and Navigation Symposium (PLANS 2014)*, Monterey, CA, USA, May 2014, pp.1203-1208.

[34] A. Sharma, "CMOS Circuits and Systems for Sub-degree/hour MEMS Gyroscopes," Ph.D. Dissertation, in Electrical Engineering, Georgia Institute of Technology, December 2007.

[35] H. Johari, F. Ayazi, "Capacitive Bulk Acoustic Wave Silicon Disk Gyroscopes," in *Electron Devices Meeting, 2006. IEDM '06. International* , pp.1-4, 11-13 Dec. 2006.

[36] Michael W. Putty, "Micromachined Vibrating Ring Gyroscope," Ph.D. Dissertation, University of Michigan, 1995.

[37] F. Ayazi, and K. Najafi, "High Aspect-ratio Combined Poly and Single-crystal Silicon (HARPSS) MEMS Technology," Microelectromechanical Systems, Journal of, 2000. 9(3): p.288-294.

[38] G.H. Bryan, "On the Beats in the Vibrations of a Revolving Cylinder or Bell," *Proc. of the Cambridge Philosophical Society*, vol. 7, pp. 101-111, 1890.

[39] Diego E. Serrano, "Integrated Inertial Measurement Units Using Silicon Bulk-Acoustic Wave Gyroscopes," Ph.D. Dissertation, Georgia Institute of Technology, 2014.

[40] Qualtré, Inc. [Online]. Available: http://www/qualtre.com

[41] B.P. Otis, J.M. Rabaey, "A 300-μW 1.9-GHz CMOS Oscillator Utilizing Micromachined Resonators," in *Solid-State Circuits, IEEE Journal of* , vol.38, no.7, pp.1271-1274, July 2003.

[42] D.H. Kim, S. Mukhopadhyay, S.K. Lim, "Fast and Accurate Analytical Modeling of Through-Silicon-Via Capacitive Coupling," in *Components, Packaging and Manufacturing Technology, IEEE Transactions on*, vol.1, no.2, pp.168-180, Feb. 2011

[43] J.I. Seeger, J. Xuesong, M. Kraft, and B.E. Boser, "Sense Finger dynamics in a ΣΔ Force-Feedback Gyroscope," in Tech. Dig. Solid-State Sensors and Actuators Workshop, Jun. 2000, pp. 296–299.

[44] A.A Trusov, M.R. Phillips, G.H. McCammon, D.M. Rozelle, A.D. Meyer, "Continuously Self-calibrating CVG System Using Hemispherical Resonator Gyroscopes," in *Inertial Sensors and Systems (ISISS), 2015 IEEE International Symposium on*, pp.1-4, 23-26 March 2015.

[45] H.M. Lavasani, W. Pan, B.P. Harrington, R. Abdolvand, and F. Ayazi, "Electronic Temperature Compensation of Lateral Bulk Acoustic Resonator Reference Oscillators Using Enhanced Series Tuning Technique," *Solid-State Circuits, IEEE Journal of* , vol.47, no.6, pp. 1381,1393, Jun. 2012.

[46] A. Norouzpour-Shirazi, M. Hodjat-Shamami, R. Tabrizian, F. Ayazi, "Dynamic Tuning of MEMS Resonators via Electromechanical Feedback," in *Ultrasonics, Ferroelectrics, and Frequency Control, IEEE Transactions on* , vol.62, no.1, pp.129-137, January 2015.

[47] G. Piazza, R. Abdolvand, G. Ho, and F. Ayazi, "Piezoelectrically-transduced, Capacitively-tuned, High-Q Single-crystal Silicon Micro-mechanical Resonators on SOI Wafers," Sensors and Actuators A, vol. 111, pp. 71–78, Mar. 2004.

[48] D.E. Serrano, R. Tabrizian, and F. Ayazi, "Electrostatically Tunable Piezoelectric-on- silicon Micromechanical Resonator for Real-time Clock," *Ultrasonics, Ferroelectrics and Frequency Control, IEEE Transactions on* , vol.59, no.3, pp. 358,365, Mar. 2012.

[49] R. Tabrizian, M. Pardo, and F. Ayazi, "A 27 MHz temperature compensated MEMS oscillator with sub-ppm instability," *in Proc. IEEE Int. Conf. MEMS*, Jan./Feb. 2012, pp. 23–26.

[50] M. Shahmohammadi, D. Dikbas, B. P. Harrington, and R. Abdolvand, "Passive Tuning in Lateral-mode Thin-film Piezoelectric Oscillators," in Proc. Joint IEEE IFCS/EFTF, pp. 1–5, May 2011.

[51] Hodjat-Shamami, M.; Norouzpour-Shirazi, A.; Tabrizian, R.; Ayazi, F., "A dynamically mode-matched piezoelectrically transduced high-frequency flexural disk gyroscope," in *Micro Electro Mechanical Systems (MEMS), 2015 28th IEEE International Conference on*, pp.789-792, 18-22 Jan. 2015.

[52] D.B. Leeson, "A Simple Model of Feedback Oscillator Noise Spectrum," *Proc. of the IEEE*, vol. 54, no. 2, pp. 329–330, Feb. 1966.

[53] R. Abdolvand, H. M. Lavasani, G. K. Ho, and F. Ayazi, "Thin-film piezoelectric-on-silicon resonators for high-frequency reference oscillator applications," *Ultrasonics, Ferroelectrics and Frequency Control, IEEE Transactions on*, vol.55, no.12, pp. 2596-2606, Dec. 2008.

[54] G.K. Ho, R. Abdolvand, A. Sivapurapu, S. Humad, F. Ayazi, "Piezoelectric-on-Silicon Lateral Bulk Acoustic Wave Micromechanical Resonators," in *Microelectromechanical Systems, Journal of*, vol.17, no.2, pp.512-520, April 2008.

[55] F. Ayazi, "MEMS for Integrated Timing and Spectral Processing," in *Proc. IEEE Custom Integrated Circuits Conf.*, pp. 65-72, Sep. 2009.

[56] R. Tabrizian, M. Hodjat-Shamami, and F. Ayazi, "High-Frequency AlN-on-Silicon Resonant Square Gyroscopes," *Microelectromechanical Systems, Journal of*, vol.22, no.5, pp. 1007-1009, Oct. 2013.

[57] W. Pan and F. Ayazi, "Thin-film Piezoelectric-on-substrate Resonators with Q-enhancement and TCF Reduction," in *Proc. IEEE Int. Conf. MEMS*, pp. 104–107, Jan. 2010.

[58] Vittoz, Eric. *Low-power crystal and MEMS oscillators: the experience of watch developments*. Springer Science & Business Media, 2010.

[59] A. M. Shkel, "Precision navigation and timing enabled by microtechnology: are we there yet?," Proc. SPIE 8031, Micro- and Nanotechnol. Sensors, Systems, and Applications vol. 3, 803118, 13 May, 2011.

[60] Robert Lutwak, "Micro-technology for Positioning, Navigation, and Timing Towards PNT Everywhere and Always." *Inertial Sensors and Systems (ISISS), 2014 International Symposium on*. IEEE, 2014.

[61] E.E. Aktakka, J.K Woo, D. Egert, R. Gordenker, K. Najafi, "A Micro Vibratory Stage for On-Chip Physical Stimulation and Calibration of MEMS Gyroscopes," in *Inertial Sensors and Systems (ISISS), 2014 International Symposium on*, pp.1-2, 25-26 Feb. 2014.

[62] E.E. Aktakka, J.K. Woo, D. Egert, R.J.M Gordenker, K. Najafi, "A Microactuation and Sensing Platform With Active Lockdown for In Situ Calibration of Scale Factor Drifts in Dual-Axis Gyroscopes," in *Mechatronics, IEEE/ASME Transactions on* , vol.20, no.2, pp.934-943, April 2015.

[63] Nadig, S.; Pinrod, V.; Ardanuç, S.; Lal, A., "Multi-modal mechanical stimuli stage for in-situ calibration of MEMS gyroscopes," in *Inertial Sensors and Systems (ISISS), 2015 IEEE International Symposium on* , vol., no., pp.1-2, 23-26 March 2015.

[64] M.H. Kline, Y.C. Yeh, B. Eminoglu, I.I. Izyumin, M. Daneman, D.A. Horsley, B.E. Boser, "MEMS Gyroscope Bias Drift Cancellation Using Continuous-time Mode Reversal," in *Solid-State Sensors, Actuators and Microsystems (TRANSDUCERS & EUROSENSORS XXVII), 2013 Transducers & Eurosensors XXVII: The 17th International Conference on*, pp.1855-1858, 16-20 June 2013.

[65] I.I. Izyumin, M.H. Kline, Y.C. Yeh, B. Eminoglu, C.H. Ahn, V.A. Hong, Y. Yang, E.J. Ng, T.W. Kenny, B.E. Boser, "A 7ppm, 6°/hr Frequency-output MEMS Gyroscope," in *Micro Electro Mechanical Systems (MEMS), 2015 28th IEEE International Conference on*, pp.33-36, 18-22 Jan. 2015.

[66] A. Norouzpour-Shirazi, D.E. Serrano, M.F. Zaman, G. Casinovi, F. Ayazi, "A Dual-mode Gyroscope Architecture with In-run Mode-matching Capability and Inherent Bias Cancellation," in *Solid-State Sensors, Actuators and Microsystems (TRANSDUCERS), 2015 Transducers - 2015 18th International Conference on*, pp.23-26, 21-25 June 2015.

[67] C.D. Ezekwe, W. Geiger, T. Ohms, "A 3-axis Open-loop Gyroscope with Demodulation Phase Error Correction," in *Solid- State Circuits Conference - (ISSCC), 2015 IEEE International*, pp.1-3, 22-26 Feb. 2015.

[68] F. Seifert, "Resistor current noise measurement," Technical Report LIGO-T0900200-v11, LIGO/Caltech, 2009.

[69] Zurich Instruments, HF2LI [Online]. Available http://www.zhinst.com/products/hf2li

[70] Alamath – Allan Variance Software [Online]. Available: http://www.alamath.com

[71] Analog Devices. AD835 – 250MHz Voltage Output 4-Quadrant Multiplier [Online]. Available: http://www.analog.com/en/products/linear-products/analog-multipliers-dividers/ad835.html

[72] Stanley F. Wyse, Robert E. Stewart, "Vibratory Gyro Bias Error Cancellation Using Mode-reversal," U.S. Patent No. 8,561,466, Oct 22, 2013.

[73] Bosch Sensortec. BMG160 – Digital Triaxial Gyroscope Sensor [Online]. Available: https://www.bosch-sensortec.com/en/homepage/products_3/3_axis_sensors/gyroscope_sensors/bmg160/bmg160

[74] Silicon Sensing. CRS43 – Single-axis Angular Rate Sensor [Online]. Available: http://www.siliconsensing.com/products/gyroscopes/

[75] Qualtré Inc. QGYR110Hx – Single-axis MEMS Gyroscope [Online]. Available: http://www.qualtre.com/single-axis-mems-gyroscope/

[76] Analog Devices Inc. ADXRS646 – High Stability Vibration Rejecting Yaw Rate Gyroscope [Online]. Available: http://www.analog.com/en/products/mems/mems-gyroscopes/adxrs646.html#product-overview